Nano-Micro Letters

e-ISSN 2150-5551
CN 31-2103/TB

REVIEW

https://doi.org/10.1007/s40820-026-02351-0

Check for updates

Cite as
Nano-Micro Lett.
(2027) 19:60

Received: 14 April 2026
Accepted: 6 August 2026
© The Author(s) 2026

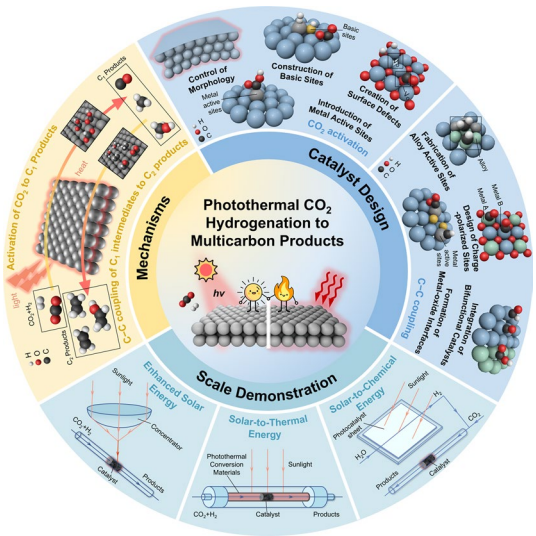
Photothermal CO_2 Hydrogenation to Multicarbon Products: Mechanisms, Catalyst Design, and Scale Demonstration

Yanlin Liao[1,2], Ying Luo[1], Zheng Wang[1,3] ✉, Qiang Wang[2] ✉, Hong He[1,3,4] ✉

HIGHLIGHTS

- Photothermal synergistic mechanism and reaction pathways from CO_2 to C_{2+} products are systematically elucidated, providing a mechanistic basis for multicarbon product synthesis.
- Photothermal catalyst modification strategies are comprehensively summarized from a pathway-oriented perspective to enhance reactant activation and promote C−C coupling toward C_{2+} products.
- Recent photothermal scale demonstrations are highlighted, underscoring the practical potential of scalable and sustainable CO_2 hydrogenation technologies.

ABSTRACT Photothermal CO_2 hydrogenation to multicarbon products presents a promising route to mitigate global climate change while simultaneously generating valuable C_{2+} products for industrial use. However, realizing high activity and selectivity toward multicarbon products remains a significant challenge, primarily due to the intricate nature of reactant activation and the inherently sluggish kinetics of C−C coupling. This review elucidates the fundamental principles of photothermal catalysis, with a particular focus on the synergistic interplay between light and thermal energy. In addition, the activation pathways of CO_2 to C_1 intermediates and the subsequent mechanisms of C−C bond formation leading to multicarbon products are systematically examined. On this basis, catalyst design and modification strategies are categorized to enhance reactant activation and facilitate efficient C−C coupling. Furthermore, recent progress in pilot-scale demonstrations is highlighted to showcase the potential for scalable and sustainable CO_2 hydrogenation technologies. By addressing the current challenges and outlining future research directions, this review aims to accelerate the development of efficient photothermal processes for CO_2 valorization.



KEYWORDS Photothermal catalysis; CO_2 hydrogenation; C−C coupling; C_{2+} products; Scale demonstration

Yanlin Liao and Ying Luo have contributed equally to this work.

✉ Zheng Wang, zhengwang@rcees.ac.cn; Qiang Wang, qiangwang@bjfu.edu.cn; Hong He, honghe@rcees.ac.cn

[1] Laboratory of Atmospheric Environment and Pollution Control, Research Center for Eco-Environmental Sciences, Chinese Academy of Sciences, Beijing 100085, People's Republic of China

[2] College of Environmental Science and Engineering, Beijing Forestry University, Beijing 100083, People's Republic of China

[3] College of Resource and Environment, University of Chinese Academy of Sciences, Beijing 101408, People's Republic of China

[4] State Key Laboratory of Advanced Environmental Technology, Institute of Urban Environment, Chinese Academy of Sciences, Xiamen 361021, People's Republic of China

Published online: 12 November 2026

Shanghai Jiao Tong University Press

Springer

1 Introduction

Over the past several decades, excessive fossil fuel consumption has resulted in CO_2 emissions exceeding 30 billion tons annually, with profound impacts on human living conditions and global climate [1, 2]. Mitigating these emissions is therefore essential for curbing global warming and advancing toward a sustainable future [3, 4]. Among various mitigation strategies, carbon capture, utilization, and storage (CCUS) has attracted considerable attention owing to its comprehensive emission reduction potential and techno-economic feasibility. As illustrated in Fig. 1, CCUS involves CO_2 capture from point sources, followed by either long-term geological storage or conversion into valuable products [5]. While storage-focused solutions provide an immediate way of emission control, they contribute minimally to resource valorization and economic sustainability. In contrast, CO_2 utilization seeks to transform CO_2 from environmental waste into a chemical feedstock, thereby enabling the production of value-added chemicals and supporting circular carbon economy [6, 7].

However, practical deployment of CO_2 utilization technologies remains challenged by intrinsic thermodynamic stability of CO_2 and energy-intensive nature of conventional catalytic processes [8–13]. To address these challenges, recent research has increasingly focused on catalytic systems driven by multiple physical fields [14–19]. Within this context, photothermal CO_2 hydrogenation has garnered significant attention due to its low cost, high solar energy absorption, and independence from fossil fuel consumption (Fig. 2) [20, 21]. The underlying mechanism of photothermal CO_2 hydrogenation combines photo-induced and thermally driven catalytic pathways [22]. The resulting synergy significantly enhances CO_2 hydrogenation efficiency, positioning photothermal catalysis as a promising strategy for sustainable carbon conversion [23, 24].

Within the spectrum of products derived from photothermal CO_2 hydrogenation, multicarbon compounds are of industrial importance due to their dual roles as energy-dense fuels and essential feedstocks for chemical synthesis [25, 26]. As a result, the efficient conversion of CO_2 to C_{2+} products has become a key research priority. Although significant progress has been made in photothermal CO_2 hydrogenation [27, 28], the selective formation of C_{2+} products remains challenging due to the inherently sluggish kinetics of C−C coupling [29, 30].

Although photothermal CO_2 hydrogenation has been reviewed from the perspectives of material design, photothermal conversion, and reactor development, systematic discussions centered on multicarbon product formation remain relatively limited. In this review, we organize recent progress according to the key reaction sequence from CO_2 activation and C_1 intermediate formation to C–C coupling and C_{2+} product generation, with particular emphasis on photothermal synergy. This reaction-oriented framework enables the comparison of different coupling mechanisms, the evaluation of photothermal roles in pathway regulation, and the clarification of catalyst design principles for selective C_{2+} synthesis. Following this logic, the fundamental principles of photothermal catalysis, CO_2 activation pathways leading to C_1 intermediates, and subsequent C−C coupling mechanisms for C_{2+} product formation are systematically elucidated. On this basis, catalyst design and modification strategies are summarized to enhance reactant activation and promote C−C bond formation. In addition, recent progress in scale demonstrations and their feasibility is discussed to support the development of scalable and sustainable CO_2 hydrogenation technologies. Finally, by identifying existing challenges and outlining future research directions, this review seeks to accelerate the development of efficient pathways for CO_2 valorization.

2 Fundamental Principles of Photothermal CO_2 Hydrogenation

Photothermal catalysis leverages photonic energy, thermal energy, and their synergistic effects, offering an innovative strategy to overcome the kinetic constraints and thermodynamic limitations of conventional CO_2 conversion reactions.

2.1 Role of Light in Photothermal Catalysis

The role of light in photothermal catalysis originates from intrinsic photocatalytic properties of semiconductors, whose tunable bandgap structures can efficiently generate charge carriers [31–33]. Specifically, as illustrated in Fig. 3a, when semiconductors absorb photons with energies equal to or greater than their bandgap, electrons in valence band are excited to conduction band, generating electron–hole pairs. These photogenerated carriers subsequently migrate to the

© The authors
https://doi.org/10.1007/s40820-026-02351-0

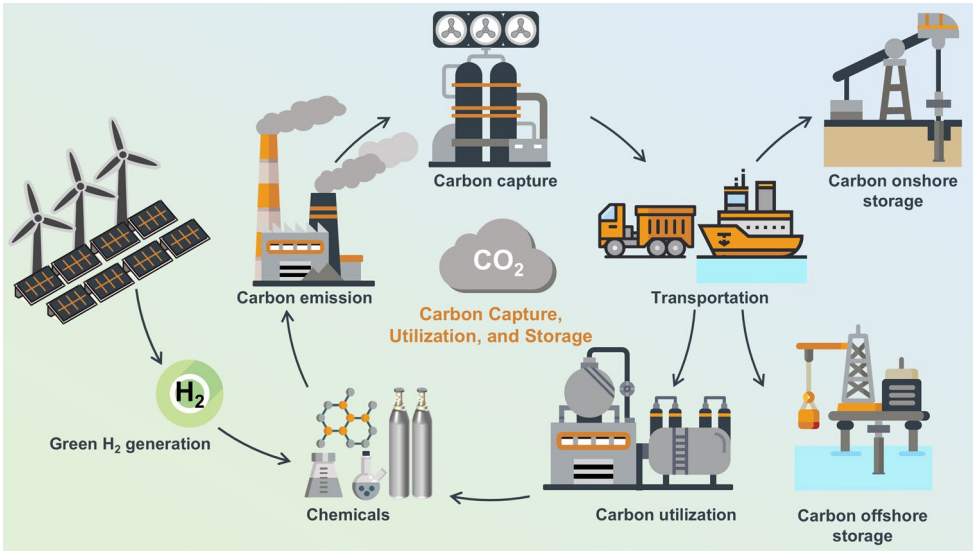


Fig. 1 Conceptual figure exemplifying the major steps of CCUS

surface of the semiconductor, where they participate in redox reactions with adsorbed CO_2* and H_2*.

In addition to the direct photoresponse of semiconductor materials, light can also induce photothermal conversion that facilitates catalytic reactions. In semiconductors, nonradiative relaxation represents the dominant photothermal conversion pathway [34, 35]. Upon illumination, electron–hole pairs undergo nonradiative recombination, where photoenergy transfers into lattice vibrations through electron–phonon coupling, resulting in localized heating [36]. For carbon-based materials, photothermal conversion proceeds through molecular vibrational excitation [37]. When incident photons possess energies matching electronic transition threshold, electrons are promoted from ground state to excited state [38]. Subsequently, via vibronic coupling, excited electrons undergo nonradiative relaxation back to the ground state, releasing excess energy as heat (Fig. 3b) [39, 40].

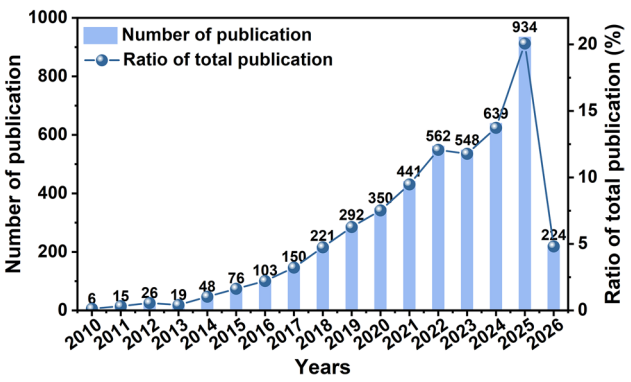


Fig. 2 Recent publications and their respective ratios of total publications related to photothermal CO_2 hydrogenation (Data for the graphs were obtained from the Web of Science Core Collection)

Noble metal nanostructures exhibit exceptional photothermal performance due to localized surface plasmon resonance (LSPR) [41]. Upon irradiation, conduction electrons in metal nanoparticles oscillate collectively to form surface plasmons. When the incident light frequency matches the resonance frequency, this collective oscillation is strongly amplified, significantly enhancing light absorption efficiency within the plasmonic metal system (Fig. 3c) [42, 43]. LSPR also intensifies local electric field at metal surface, promoting the generation of energetic charge carriers that facilitate reactant activation [44]. When this field enhancement peaks, part of the energy is released via radiative relaxation, while the majority dissipates through nonradiative processes. These nonradiative events generate energetic hot electrons, which may be injected into the conduction band of adjacent semiconductors or directly participate in surface redox reactions. Simultaneously, a portion of the absorbed energy is converted into heat, raising local reaction temperature and thereby enhancing catalytic kinetics (Fig. 3d).

2.2 Role of Heat in Photothermal Catalysis

From a kinetic perspective, localized temperature field in photothermal systems plays a crucial role in regulating

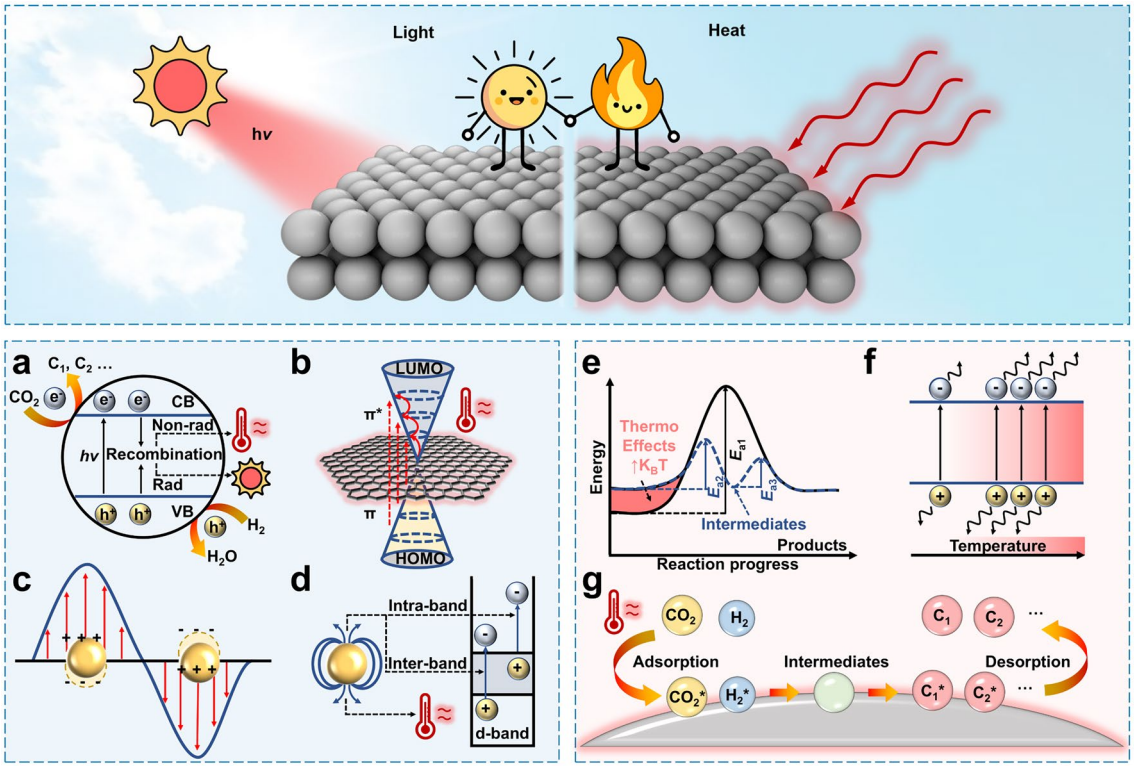


Fig. 3 Role of light and heat in photothermal catalysis. **a** Light effect on semiconductors. **b** Molecular thermal vibration on carbon-based materials. Reproduced with permission from Ref. [39], Copyright 2024 John Wiley and Sons. **c** Dynamics of excited plasmonic nanoparticles. Reproduced with permission from Ref. [42], Copyright 2019 American Chemical Society. **d** Hot carrier generation induced by LSPR effect. Reproduced with permission from Ref. [47], Copyright 2022 The Royal Society of Chemistry. **e** Thermochemical contributions to energy path of endothermic reactions. Reproduced with permission from Ref. [24], Copyright 2019 The Royal Society of Chemistry. **f** Thermochemical contributions to charge carrier migration. **g** Mass transfer processes

reaction rate. According to Arrhenius equation, an increase in temperature reduces the negative exponent, thereby enhancing the rate constant and accelerating elementary reaction steps. At molecular level, thermal activation enhances translational motion, thereby increasing both collision frequency and energy transfer efficiency during molecular collisions.

Furthermore, the influence of temperature can be interpreted from the perspective of the Boltzmann distribution. As temperature increases, the population of molecules occupying higher energy states rises due to slower decay of exponential energy distribution. This shift results in a substantially larger fraction of energetic species capable of initiating bond dissociation and overcoming activation energy barriers, thereby accelerating photothermal catalytic processes (Fig. 3e) [24].

Beyond accelerating intrinsic reaction kinetics, thermal effects also contribute to improved mass transport. In photothermal catalysis, localized heating can enhance charge carrier mobility and interfacial charge transfer efficiency (Fig. 3f) [45, 46], while in thermal-driven catalytic processes, it promotes reactant adsorption, intermediate migration, and product desorption, collectively leading to more efficient catalytic turnover (Fig. 3g) [47, 48].

2.3 Strengthening Mechanism and Evaluation Criteria of Photothermal Synergy

The essence of photothermal synergy lies in the coupling of photonic and thermal effects. In principle, light irradiation can generate excited carriers and modulate surface electronic structures, while the accompanying thermal effect accelerates elementary reaction steps, intermediate diffusion, and mass transfer. The coupling of these two effects may enhance CO_2 hydrogenation through three

© The authors
https://doi.org/10.1007/s40820-026-02351-0

main pathways: promoting charge transport, lowering reaction barriers, and regulating reaction routes. However, enhanced activity under illumination does not necessarily indicate true photothermal synergy, because light may also simply serve as a heat source. Therefore, the discussion of photothermal synergy should not only describe the improved catalytic performance under light and heat, but also provide criteria to distinguish thermal-dominated effects, photochemical effects, and photothermal synergy.

Temperature-matched light/dark comparison is the basic criterion for this distinction. Comparing illuminated reactions with dark reactions only at the same furnace temperature is insufficient, because light irradiation may create local temperature gradients on the catalyst surface. If illumination changes the reaction rate, product selectivity, apparent activation energy, intermediate evolution, or electronic structure under temperature-matched conditions, non-thermal photochemical effects, or true photothermal synergy should be considered [49]. For example, to distinguish non-thermal photon effects from localized heating, direct and indirect illumination experiments were performed using a Ti_2O_3 overlayer, which provided comparable thermal input while blocking direct photon access to the catalyst surface. Under direct illumination, CO_2 conversion showed a nearly linear dependence on light intensity in the range of 2.8–4.0 W cm^{-2}, indicating a significant non-thermal photon contribution. By contrast, indirect illumination led to a nonlinear conversion trend dominated by thermal effects. Under comparable conditions, CO_2 conversion under direct illumination was approximately 1.3 times that under indirect illumination, accompanied by an approximately 5% increase in C_{2+} product selectivity. Moreover, as the light intensity increased from 2.8 to 4.8 W cm^{-2}, the conversion difference between direct and indirect illumination decreased from 36.94% to 20.96%, suggesting that the relative contribution of non-thermal effects declined at higher irradiance because of enhanced thermal accumulation [50]. On this basis, kinetic analysis, operando spectroscopy, electronic structure characterization, and carrier dynamics measurements are required to further identify the specific contribution of light and heat.

Within this framework, photothermal synergy first optimizes charge transport and proton transfer. In photothermal catalysis, light irradiation generates electron–hole pairs, while thermal energy promotes charge carrier separation and migration, thereby enhancing redox activity. Such carrier-related contributions are commonly supported by electrochemical characterizations, including time-resolved photoluminescence, transient photocurrent measurements, and electrochemical impedance spectroscopy, which provide information on carrier lifetime, separation efficiency, recombination behavior, and interfacial charge transfer resistance [51]. Meanwhile, thermal effects can also influence carrier dynamics. Elevated temperatures significantly reduce migration impedance of photogenerated carriers in materials such as TiO_2, ZnO, and CeO_2, thus facilitating more efficient charge transport [52–54]. However, excessive thermal input may also increase the electron–hole recombination rate, which can be mitigated through rational structural engineering of catalysts. LSPR provides an alternative route to enhance electron and proton transport under photothermal conditions [55, 56]. In $Ru/SrTiO_3$ catalysts, LSPR-induced hot electrons and localized heating synergistically accelerated H_2 dissociation, promoting their migration and spillover to the metal–support interface, thereby facilitating the hydrogenation of CO_2 to CH_4 [57].

Electronic structure characterization is also essential for identifying carrier-mediated photothermal synergy, especially when CO_2 activation is proposed to proceed through surface redox cycles. In such cases, light irradiation not only increases local temperature but also induces electronic reconstruction and charge redistribution, whereas heat accelerates surface reaction kinetics. In situ X-ray photoelectron spectroscopy (XPS) and electron paramagnetic resonance (EPR) can provide such evidence by tracking electronic structure evolution under working conditions. For example, in $Ru/LaFeO_3$-mediated photothermal dry reforming, in situ XPS and EPR revealed light-induced charge redistribution and oxygen vacancy cycling under illumination [58]. The thermal effect further accelerated the turnover of this redox cycle, thereby promoting CO_2 activation and sustaining surface redox reactions beyond simple light-induced heating [59].

Second, photothermal synergy can reduce catalytic energy barriers. In this system, photoinduced carriers contribute redox capability, while thermal energy helps to overcome kinetic constraints. Apparent activation energies derived from Arrhenius analysis are frequently employed to quantify this effect under thermal and photothermal conditions [60]. Photothermal synergy can lower the apparent activation energy by approximately 10%−20%, primarily due to the direct involvement of photogenerated carriers, which introduce alternative reaction pathways [44, 54]. Furthermore,

light excitation can modify the energy landscape by altering the adsorption behavior of key intermediates. In Pt/Al_2O_3 system, light irradiation induced CO migration from Pt step sites to terrace sites, weakening CO–Pt interactions and lowering the CO desorption barrier from 1.43 to 1.24 eV, thereby facilitating CO_2 hydrogenation [61].

Finally, photothermal synergy enables regulation of reaction pathways and product selectivity. Photoexcitation can modulate electronic structure of catalyst surface, thereby altering the reaction mechanism and enabling control over product distribution and selectivity. In situ or operando vibrational spectroscopy is especially useful for distinguishing simple thermal acceleration from light-induced pathway regulation. When illumination changes the dominant intermediate, promotes the formation of a specific reactive species, or suppresses a competing route under comparable thermal conditions, pathway-level photothermal contribution can be inferred. Specifically, it was reported that photoexcitation can increase the electron density at metal sites, shifting CO_2 activation pathway from thermally driven HCOO* intermediates to photothermally promoted COOH* species, which lowered activation barrier and enhanced hydrogenation activity [62]. Theoretical insights further suggested that temperature variation can alter the rate-determining step and associated energy barrier in C_1 product formation, thereby influencing product selectivity. While higher temperatures can enhance the thermodynamic favorability of C_1 product formation across different surface sites, an optimal temperature likely exists to maximize selectivity [36].

Overall, true photothermal synergy should not be assigned solely on the basis of enhanced catalytic activity under illumination. Its reliable identification requires surface temperature-matched light/dark comparisons, carrier dynamics measurements, electronic structure characterization, apparent activation energy analysis, and operando vibrational spectroscopy. These criteria are essential for distinguishing thermal-dominated enhancement from photothermal synergy.

3 Reaction Pathway of Photothermal CO_2 Hydrogenation to C_2 Products

Understanding the reaction pathway of photothermal CO_2 hydrogenation is essential for rational design of catalysts toward multicarbon products. The conversion of CO_2 to C_{2+} products proceeds through a cascade reaction network involving CO_2 activation, C_1 intermediate formation, and subsequent C–C bond construction. In this network, the first stage involves CO_2 activation and its conversion into C_1 intermediates, including CO*, CH_x*, and CH_3OH-related species. The second stage involves C–C bond formation from these C_1 intermediates, which directly governs the formation and selectivity of C_{2+} products.

3.1 Reaction Pathway from CO_2 to C_1 Products

CO_2 activation to C_1 intermediates is the prerequisite for subsequent C–C coupling. Depending on the initial activation mode and hydrogenation sequence, CO_2 can be converted into CO*, CH_x*, and CH_3OH-related species through direct C=O cleavage, COOH*-mediated pathways, or HCOO*-mediated pathways. These C_1 species provide the upstream reactive intermediates for multicarbon product formation.

3.1.1 CO_2 Hydrogenation to CO

As the simplest C_1 product of CO_2 hydrogenation, CO plays a central intermediate role in downstream C−C coupling pathways. Owing to its endothermic nature ($\Delta_R H^0_{298K} = +41.2\ kJ\ mol^{-1}$), CO formation is particularly sensitive to localized thermal effects, making it well suited for photothermal catalysis. Table 1 summarizes recently reported catalysts for photothermal CO_2 hydrogenation to CO.

CO can be produced through direct cleavage of C=O bond, with the release of an oxygen atom at oxygenophilic sites to form adsorbed CO* intermediate (Fig. 4a). Consequently, catalysts capable of reversibly binding oxygen species are particularly effective for this pathway by preventing surface oxygen accumulation and sustaining active-site availability [63]. In this context, metal–metal oxide redox cycling contributes to efficient CO formation, as H-induced reduction of Fe_3O_4 to metallic Fe enables direct C=O dissociation of CO_2 to form CO, followed by reoxidation to Fe_3O_4 (Fig. 4b) [64]. Beyond metallic centers, dynamically generated oxygen vacancies further promote C=O bond cleavage by capturing terminal oxygen atoms from CO_2 under photothermal conditions [65, 66].

In addition to oxygen abstraction-driven C=O bond cleavage, photothermal CO_2 hydrogenation to CO frequently

© The authors https://doi.org/10.1007/s40820-026-02351-0

follows a COOH*-mediated reaction pathway, which can be directly observed through in situ diffuse reflectance infrared Fourier transform spectroscopy (DRIFTS) (Fig. 4c) [67]. Moreover, it was observed that the accumulation rate of COOH* intermediates on catalyst surfaces under concentrated light illumination is significantly higher than under dark thermal conditions, underscoring the advantages of photothermal coupling [46, 68].

3.1.2 CO_2 Hydrogenation to CH_4

Unlike CO formation, photothermal CO_2 hydrogenation to CH_4 requires cleavage of both C=O bonds through multiple hydrogenation steps, rendering the process mechanistically more complex. Despite the existence of multiple pathways, CH_4 formation commonly proceeds through surface CH_x* intermediates as the main species (Fig. 5a). Table 2 summarizes recent advances in photothermal CO_2 hydrogenation to CH_4.

Table 1 Recent developments in photothermal CO_2 hydrogenation to CO

Catalyst	Reactor type	P (bar)	Light	GHSV[a] (mL g^{-1} h^{-1})	H_2/CO_2 ratio	T (°C)	CO sel.[b] (%)	CO rate (mmol g^{-1} h^{-1})	Ref.[c]
Bi_2O_{3-x}	batch	N.R.[d]	LED lamp (0.011 W cm^{-2})	–	3:1	26	100	~0.01	[69]
$In_2O_{3-x}(OH)_y$	batch	1	300 W Xe lamp (1 W cm^{-2})	–	1:1	150	N.R.	~0.4	[70]
In_2O_{3-x}	batch	1	300 W Xe lamp (0.1 W cm^{-2})	–	1:1	340	~100	103.2	[71]
$Ni/LaInO_3$	batch	1	300 W Xe lamp (3 W cm^{-2})	–	4:1	280	~100	26.3	[67]
Pt/Al_2O_3	batch	N.R.	LED lamp (0.71 W cm^{-2})	–	6:1	400	~80	~4.8	[61]
PtRh/GaN/Si	batch	1	300 W Xe lamp (5.3 W cm^{-2})	–	12:1	350	98.5	11700	[46]
Co@CoN&C	batch	0.55	300 W Xe lamp	–	1:1	518	91.1	132	[72]
Co@C	batch	1	300 W Xe lamp (3 W cm^{-2})	–	1:1	380	92.6	536.7	[20]
$FeO-CeO_2$	batch	1.8	300 W Xe lamp (2.2 W cm^{-2})	–	4:1	419	99.9	19.6	[73]
Cs/In_2O_3	flow	1	300 W Xe lamp	15,000	4:1	230	100	28	[74]
Pd/TiO_2	flow	1	300 W Xe lamp (2.5 W cm^{-2})	24,000	4:1	250	86	7.2	[75]
Rh/TiO_2	flow	1	300 W Xe lamp (2.7 W cm^{-2})	24,000	4:1	250	100	20.6	[76]
$Ga-Cu/CeO_2$	flow	1	300 W Xe lamp (1.95 W cm^{-2})	12,000	1:1	280	~100	111.2	[77]
$Cu_2Zn_1Al_{0.5}Ce_5Zr_{0.5}O_x$	flow	1	Solar light source (0.1 W cm^{-2})	1,200	1:1	500	100	37.4	[68]
PI/A/S/S−Ni	flow	1	300 W Xe lamp (0.8 W cm^{-2})	1,622	5:1	230	87.3	516.9	[78]
Ni_3N	flow	1	300 W Xe lamp (2.7 W cm^{-2})	2,310,000	1:10	199	99	1212	[79]
Mo_2N/MoO_{2-x}	flow	1	300 W Xe lamp (0.1 W cm^{-2})	240,000	1:1	250	~100	355	[80]
K^+-Co-C	flow	1	300 W Xe lamp (2.8 W cm^{-2})	600,000	1:1	450	>95	758	[81]
$Co_{15}HAP$	flow	1	300 W Xe lamp (0.108 W cm^{-2})	15,600	1:1	400	83	62	[82]

[a]GHSV, gas hourly space velocity. [b]sel., selectivity. [c]Ref., reference. [d]N.R., not reported

In direct C=O bond cleavage pathway, one C=O bond of the adsorbed CO_2 molecule is cleaved to form CO*, followed by the cleavage of the second C=O bond under hydrogenation. Dalmon et al. (1978) first observed infrared bands corresponding to CO* vibrations during the chemisorption of CO_2 on a Ni/SiO_2 catalyst. Based on these observations, they proposed a pathway involving CO_2 (gas) → CO* + O* [83]. In photothermal catalytic systems, CO* and HCOO* species were detected on a Ru/TiO_2 catalyst, suggesting that the CO_2-to-CH_4 conversion can follow direct C=O bond cleavage pathway (Fig. 5b) [84].

In COOH* pathway, chemisorbed CO_2* reacts with dissociated H* to form a COOH* intermediate, which subsequently decomposes into CO* and H_2O. Depending on the hydrogenation position during the second C=O bond breakage, this pathway can be further divided into the COOH*-HCO* and COOH*-COH* routes [85]. Among them, the COOH*-HCO* pathway has been more extensively investigated experimentally [62, 86], whereas the COOH*-COH* pathway is more frequently proposed in theoretical studies [87, 88]. In a MnO−Co catalytic system, COOH* species were identified via in situ DRIFTS, while hydrogenation products such as CO* and H_xCO* were detected by in situ ambient pressure X-ray photoelectron spectroscopy (AP-XPS) C 1*s* spectra. These experimental findings provide compelling evidence for the COOH*-HCO* pathway in photothermal CO_2-to-CH_4 conversion (Fig. 5c) [62].

Moreover, CH_4 can be produced through HCOO* pathway, where CO_2 is initially hydrogenated at the carbon site to form an HCOO* intermediate [89, 90]. HCOO* then undergoes further hydrogenation at the oxygen site to produce HCOOH*. HCOOH* may either hydrogenate to H_2COOH* and subsequently dehydrate to form CH_2* [91], or hydrogenate to H_3COOH* and dehydrate to yield CH_3*, ultimately leading to CH_4 formation. After experimentally observing the HCOO* intermediate, Jia Zhu et al. employed density functional theory (DFT) calculations to investigate the CO_2 methanation pathway over

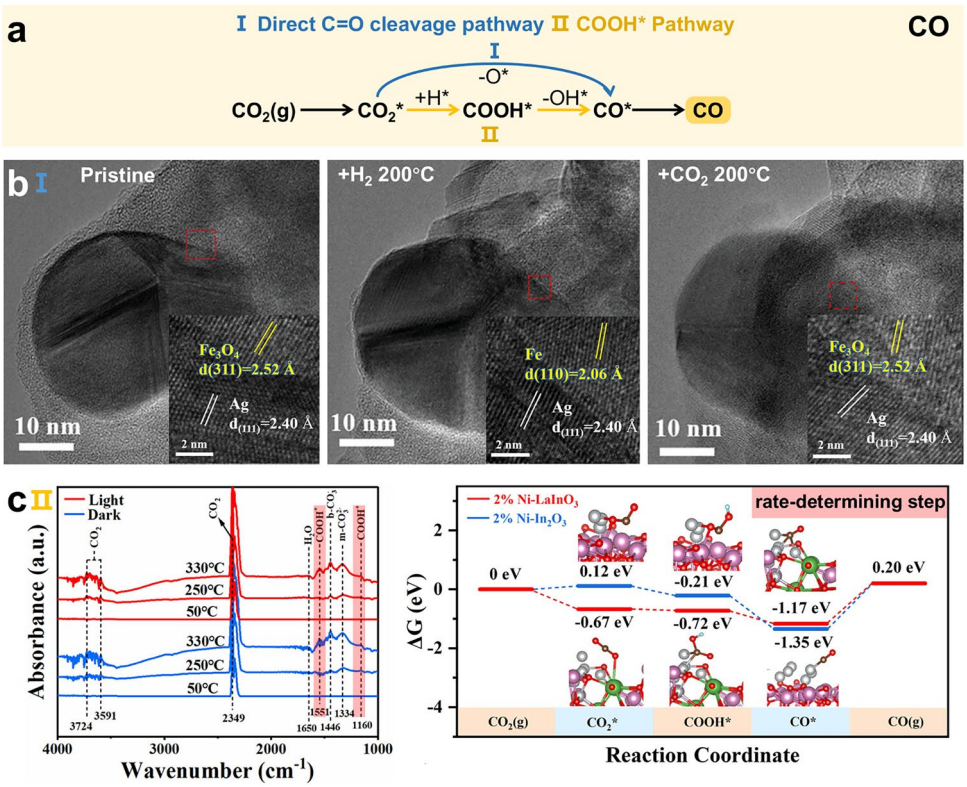


Fig. 4 Reaction pathways for photothermal CO_2 hydrogenation to CO. **a** Possible reaction pathways. **b** Direct C=O cleavage pathway revealed by in situ transmission electron microscopy (TEM) and density functional theory (DFT) calculations. Reproduced with permission from Ref. [64], Copyright 2025 John Wiley and Sons. **c** COOH* pathway revealed by in situ DRIFTS. Reproduced with permission from Ref. [67], Copyright 2023 John Wiley and Sons

© The authors
https://doi.org/10.1007/s40820-026-02351-0

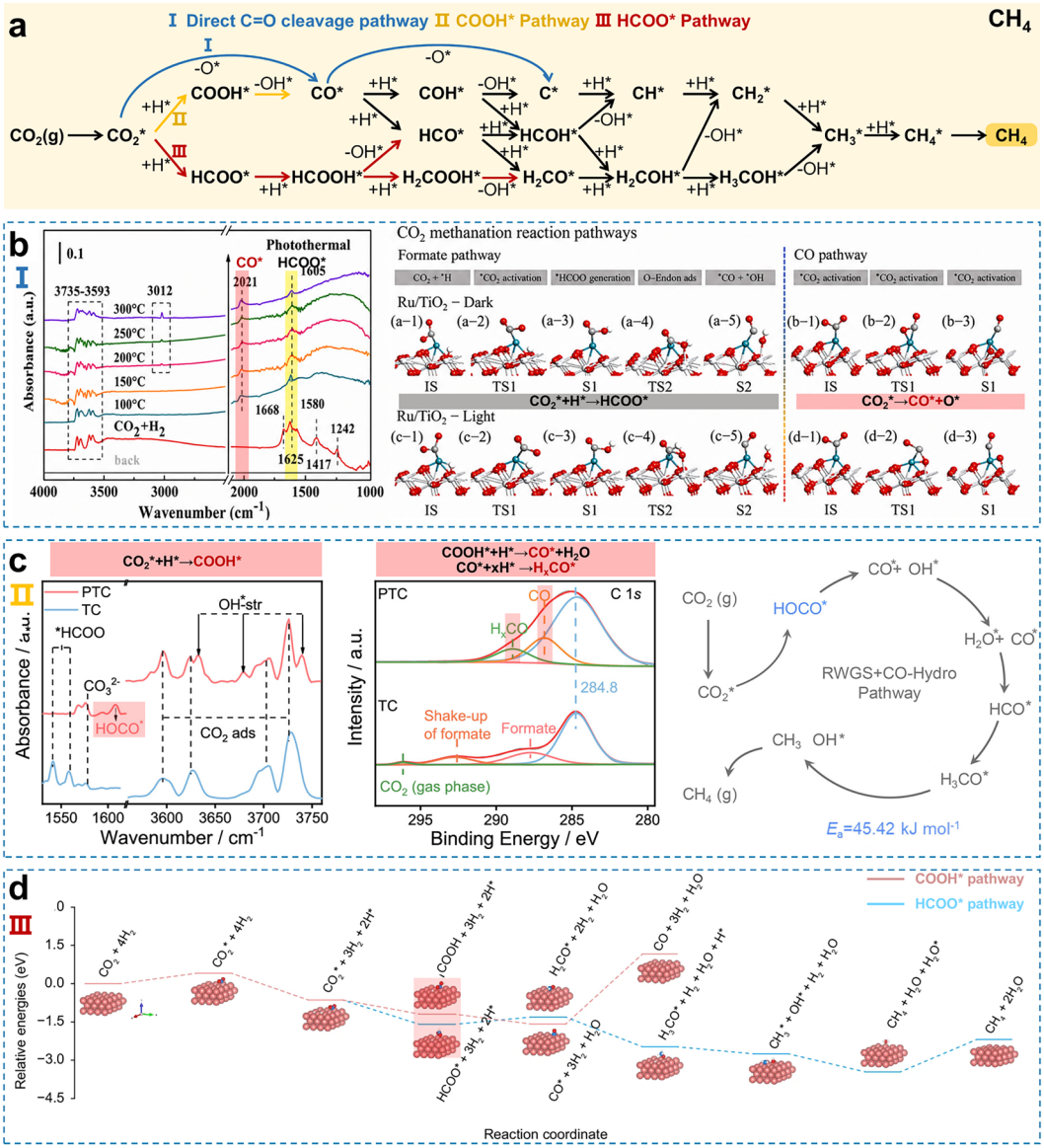


Fig. 5 Reaction pathways for photothermal CO_2 hydrogenation to CH_4. **a** Possible reaction pathways. **b** Direct C=O cleavage pathway revealed by in situ DRIFTS and DFT calculations. Reproduced with permission from Ref. [84], Copyright 2022 Elsevier. **c** COOH* pathway revealed by in situ DRIFTS and in situ AP-XPS. Reproduced with permission from Ref. [62], Copyright 2021 American Chemical Society. **d** HCOO* pathway revealed by DFT calculations. Reproduced with permission from Ref. [92], Copyright 2024 Springer Nature

Ru@m-$Ti_3C_2T_x$. HCOO* pathway exhibited more favorable thermodynamics than the COOH* pathway, ultimately confirming its dominance in photothermal CO_2 hydrogenation to CH_4 (Fig. 5d) [92].

3.1.3 CO_2 Hydrogenation to CH_3OH

CH_3OH is a simple saturated monohydric alcohol with a high hydrogen storage capacity per unit mass and volume, making it an ideal target product for photothermal CO_2 hydrogenation [106]. However, its formation is intrinsically challenging because it requires the cleavage of one C=O bond while retaining the other. Table 3 summarizes recent progress in photothermal CO_2 hydrogenation to CH_3OH. Additionally, CH_3OH also serves as a key intermediate in the reaction network for CO_2 hydrogenation to C_{2+} products, providing mechanistic insights for improving C_{2+} product yields [107].

Table 2 Recent developments in photothermal CO_2 hydrogenation to CH_4

Catalyst	Reactor type	P (bar)	Light	GHSV (mL g^{-1} h^{-1})	H_2/CO_2 ratio	T (°C)	CH_4 sel. (%)	CH_4 rate (mmol g^{-1} h^{-1})	Ref.
In_2O_3@In	batch	1.2	300 W Xe lamp (0.26 W cm^{-2})	–	4:1	250	>99	1.04	[93]
Ni@TiO_2	batch	N.R.	300 W Xe lamp (2.5 W cm^{-2})	–	4:1	420	81.8	286.5	[86]
MnO−Co	batch	1	300 W Xe lamp (1 W cm^{-2})	–	4:1	150	86.1	5.19	[62]
Co_3O_4	batch	15	Xe lamp	–	4:1	140	97.7	21.1	[94]
Ru/TiO_2	flow	1	300 W Xe lamp	11,000	4:1	300	87	N.R.	[84]
RuCo/TiO_2	flow	1	300 W Xe lamp (1.9 W cm^{-2})	24,000	4:1	250	94.6	191	[89]
Ru/H_xMoO_{3-y}	flow	1	Vis-NIR light (0.75 W cm^{-2})	4000	1:1	140	100	20.8	[95]
Ru/$MnCo_2O_4$	flow	1	300 W Xe lamp (1.25 W cm^{-2})	24,000	4:1	230	96	66.3	[96]
Ru/MnO/Mn_3O_4	flow	1	300 W Xe lamp (2.5 W cm^{-2})	40,000	4:1	200	99.5	166.7	[97]
Ru/Mg−CeO_2	flow	1	300 W Xe lamp	200,000	4:1	400	93.1	469	[98]
Co/CeO_2	flow	1	300 W Xe lamp	12,000	3:1	200	97.3	885.3	[99]
Ni/CeO_2	flow	1	300 W Xe lamp (~6 W cm^{-2})	32,000	4:1	~270	>99	9.12	[100]
Ni/TiO_2	flow	1	300 W Xe lamp (15.3 W cm^{-2})	150,000	4:1	283	96.9	41.5	[101]
50Ni/ZrO_2	flow	1	300 W Xe lamp (2.9 W cm^{-2})	150,000	4:1	394	95.4	583.3	[102]
MnNiZrRuCe HEMG	flow	1	300 W Xe lamp (1.14 W cm^{-2})	90,000	4:1	300	~100	290	[103]
Ir−CoO/Al_2O_3	flow	1	300 W Xe lamp (2 W cm^{-2})	24,000	4:1	250	92	128.9	[91]
Ir@UiO-66	flow	1	300 W Xe lamp (2.3 W cm^{-2})	24,000	4:1	250	~95	19.9	[104]
Pt/$LaCoO_3$	flow	1	300 W Xe lamp (1.2 W cm^{-2})	24,000	4:1	250	87	119.8	[105]

To date, CH_3OH synthesis via photothermal CO_2 hydrogenation typically proceeds through two primary intermediates: COOH* and HCOO* (Fig. 6a) [108]. The COOH* pathway involves two consecutive steps: (1) CO_2 is hydrogenated to form COOH*, which is further reduced to CO*, and (2) CO* is subsequently hydrogenated to produce CH_3OH [108, 109]. In contrast, in HCOO* pathway, CO_2 is initially hydrogenated at the carbon site to form HCOO*, which is then converted into HCOOH*. This intermediate subsequently generates CH_3O* and undergoes further hydrogenation to form CH_3OH [110]. It has also been reported that HCOOH* can follow an alternative hydrogenation route to generate HCO*, which is further hydrogenated at the oxygen site to produce CH_3OH [111].

In typical studies of photothermal CO_2 hydrogenation to CH_3OH, mechanistic pathways are often investigated by first applying in situ DRIFTS to detect surface intermediates, followed by DFT calculations to validate the proposed pathways. However, DRIFTS-based assignments of intermediates, including COOH*, HCOO*, and CH_3O* species, should be treated cautiously because their vibrational bands may overlap with carbonate or bicarbonate spectator species, and short-lived intermediates may remain undetected. Therefore, DFT calculations and isotope-labeling experiments are often needed to distinguish dominant

© The authors
https://doi.org/10.1007/s40820-026-02351-0

reaction routes from merely observable surface species. For example, on a cobalt phthalocyanine (CoPc)/carbon nanotube system, the introduction of CO_2 and H_2 led to the observation of stretching vibrations associated with COOH*, along with a weak absorption band attributed to HCOO*. Subsequent DFT calculations assessed the thermodynamic stability of adsorbed COOH* and HCOO*, revealing that HCOO* was thermodynamically less stable. Furthermore, the absence of hydrogenation intermediates derived from HCOO* in operando DRIFTS further evidenced COOH* pathway (Fig. 6b) [109]. HCOO* was first directly identified on Bi_2WO_6 nanosheets, and subsequent DFT calculations of CO_2 adsorption and hydrogenation further confirmed the thermodynamic feasibility of HCOO* pathway (Fig. 6c) [112]. Moreover, both COOH* and HCOO* pathways can coexist in photothermal CO_2 hydrogenation reactions, potentially working synergistically to enhance CH_3OH production [113, 114].

3.2 Reaction Pathway from C_1 Intermediates to C_2 Products

After C_1 intermediates are generated, C–C bond formation becomes the decisive step for C_{2+} product synthesis. According to the dominant coupling species, C–C coupling in CO_2 hydrogenation can be classified into CO*-mediated, CH_x*-mediated, and CH_3OH*-mediated routes. Table 4 summarizes recent progress in the photothermal hydrogenation of CO_2 toward multicarbon products.

3.2.1 *CO* Coupling*

CO* coupling in photothermal CO_2 hydrogenation to C_2 products can be further classified into CO*−CO* coupling, CO*−COH*/HCO* coupling, and CO*−CH_x* coupling (Fig. 7a).

In CO_2 hydrogenation, the widely accepted C−C coupling mechanism begins with the reduction of CO_2 to CO*, followed by the direct coupling of two CO* intermediates to form OCCO* species. This intermediate then undergoes successive hydrogenation and deoxygenation steps to yield C_2 products. Under photothermal conditions, AuCu alloy-modified g-C_3N_4 system proposed a direct CO*−CO* coupling mechanism, where CO_2 was initially reduced via COOH* pathway to CO*, and subsequently dimerized to form OCCO* [136]. Additionally, OCCO* intermediate was identified as vibrational peak during photothermal CO_2 reduction over Zn−O−Ge tri-atomic sites, providing direct evidence for the CO*−CO* coupling route (Fig. 7b) [137].

However, some studies suggested that the formation of OCCO* is associated with a relatively high energy barrier [138], whereas coupling between CO* and hydrogenated

Table 3 Recent developments in photothermal CO_2 hydrogenation to CH_3OH

Catalyst	Reactor type	P (bar)	Light	GHSV (mL g^{-1} h^{-1})	H_2/CO_2 ratio	T (°C)	CH_3OH sel. (%)	CH_3OH rate (μmol g^{-1} h^{-1})	Ref.
CoPc/CNT	batch	40	1000 W Xe lamp (2.0 W cm^{-2})	–	3:1	~245	~99	2400	[109]
In_2O_3	batch	6	Xe lamp (1.2 W cm^{-2})	–	3:1	200	61	1436	[115]
Au/In_2O_3	batch	25	300 W Xe lamp (0.1054 W cm^{-2})	–	3:1	250	~56	320	[116]
Pd_3Cu@UiO-66	batch	12.5	300 W Xe lamp	–	3:1	200	88	340	[117]
$CaCu_3Ti_4O_{12}$	flow	1	130 W Xe lamp	4800	3:1	250	17	14.1	[118]
Cu/ZnO	flow	1	Xe lamp (0.58 W cm^{-2})	60000	3:1	220	~13	2.1	[119]
$In_2O_{3-x}(OH)_y$	flow	1	130 W Xe lamp	32000	3:1	250	53	63.7	[110]
$H_zIn_2O_{3-x}(OH)_y$	flow	1	300 W Xe lamp (0.6 W cm^{-2})	N.R.	1:1	250	18.9	7.2	[120]
rh-$In_2O_{3-x}(OH)_y$	flow	1	130 W Xe lamp	24000	3:1	270	~13	180	[113]
$Bi_xIn_{2-x}O_3$	flow	1	300 W Xe lamp (2 W cm^{-2})	24000	3:1	230	14.7	158	[114]
Ru/In_2O_3	flow	1	300 W Xe lamp	120000	3:1	250	18	280.4	[108]

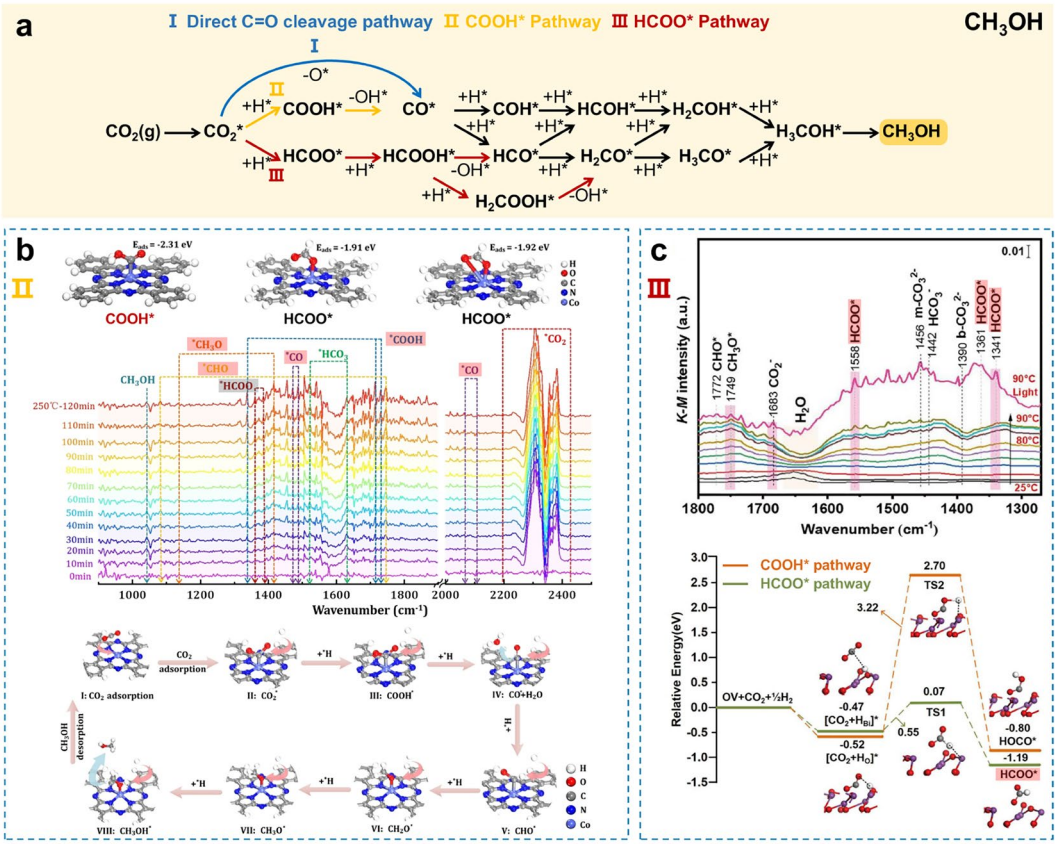


Fig. 6 Reaction pathways for photothermal CO_2 hydrogenation to CH_3OH. **a** Possible reaction pathways. **b** COOH* pathway revealed by in situ DRIFTS and DFT calculations. Reproduced with permission from Ref. [109], Copyright 2024 John Wiley and Sons. **c** HCOO* pathway revealed by in situ DRIFTS and DFT calculations. Reproduced with permission from Ref. [112], Copyright 2025 Springer Nature

species (e.g., HCO* or COH*) proceeds with lower activation energies, from an energy barrier of 1.52 eV (CO*+CO*) to 1.08 eV (CO*+CHO*) on Cu/TiO_2 [139]. In a Cu-promoted CoFe alloy catalyst, C_1 intermediates including HCO* and CO*, along with C_2 intermediates, C=CH*, were detected during CO_2 hydrogenation process. On this basis, mechanistic analysis suggested that the most thermodynamically favorable pathway involved the coupling of CO* and HCO* to form OCCHO*, followed by successive hydrogenation steps to generate COCH*, CHC*, and ultimately multicarbon alkenes and alkanes (Fig. 7c) [135].

Additionally, coupling between CO* and CH_x* species, leading to the formation of $COCH_x$*, represents another viable pathway for C_2 product generation. It is reported that ethanol can be formed via CO*–CH_3* coupling, based on the detection of CO*, CH_3*, and CH_3CH_2O* intermediates (Fig. 7d) [140].

Overall, CO*-mediated coupling requires sufficient CO* coverage and suitable adsorption configurations to stabilize C–C coupling intermediates. Direct CO*–CO* coupling can be promoted on sites with asymmetric electronic structures, whereas coupling between CO* and partially hydrogenated species is often more favorable when the surface can balance CO* retention and hydrogenation. Photothermal catalysis may further facilitate this process by combining localized thermal activation, which promotes intermediate mobility

© The authors https://doi.org/10.1007/s40820-026-02351-0

Table 4 Recent developments in photothermal CO_2 hydrogenation to multicarbon products

Catalyst	Reactor type	P (bar)	Light	GHSV (mL g^{-1} h^{-1})	H_2/CO_2 ratio	T (°C)	C_{2+} rate (mmol g^{-1} h^{-1})	Sel. (%)			Ref.
								C_{2+}	CO	CH_4	
TiO_2	batch	0.2	200 W Hg lamp (0.15 W cm^{-2})	–	1.5:1	120	~0.0041	3.1	44.7	52.2	[121]
$NiFeO_x$	batch	2.7	1000 W Xe lamp (5 W cm^{-2})	–	5:1	300	~12.72	21.6	0.7	77.7	[122]
NiO_x/Nb_2O_5	batch	1	N.R.	–	6:1	250	0.194	57.12	2.01	40.86	[123]
Na−Co@C	batch	2.8	1000 W Xe lamp (2.4 W cm^{-2})	–	5:1	235	4.12	39.7	0	62.7	[124]
MnO−Co	batch	1	300 W Xe lamp (1 W cm^{-2})	–	4:1	150	0.63	15.87	0	84.13	[62]
$Co_7Cu_1Mn_1O_x$	batch	1	300 W Xe lamp (0.234 W cm^{-2})	–	5:1	200	1.40	30.9	3.7	65.4	[125]
Fe/C	batch	1	300 W Xe lamp (2.05 W cm^{-2})	–	3:1	310	~0.82	15.2	59.8	25	[126]
Fe_3C	batch	1	300 W Xe lamp (2.05 W cm^{-2})	–	2:1	310	0.89	11.4	25.3	63.4	[126]
K−Ru/Fe_3O_4	batch	1	300 W Xe lamp (2.05 W cm^{-2})	–	3:1	420	0.63	23.8	67.2	9	[127]
CoFe alloy/Al_2O_3	batch	1.8	300 W Xe lamp (5.2 W cm^{-2})	–	4:1	320	~0.42	35.3	5.0	59.8	[128]
Fe/FeO_x/Al_2O_3−MgO	batch	1.8	300 W Xe lamp (1.88 W cm^{-2})	–	4:1	275	0.32	42.2	20.3	37.5	[129]
$CoFe_2O_4/(Fe_{1-x}Co_x)_5C$	batch	3	300 W Xe lamp (1.7 W cm^{-2})	–	3:1	305	2.64	63.4	19.4	17.2	[130]
Fe_3C/ZnO	flow	0	homemade light source (0.12 W cm^{-2})	2400	3:1	321	0.63	~25.80	~62.0	~12.20	[131]
K-$Fe_{10}Mn_1$	flow	20	300 W Xe lamp (4 W cm^{-2})	12000	4:1	250	4.80	59.6	24.1	16.3	[50]
CoFe alloy/Al_2O_3	flow	1.8	300 W Xe lamp (2.16 W cm^{-2})	9000	4:1	250	~0.26	21.01	45.95	33.04	[132]
NiFe alloy/Al_2O_3	flow	1.8	300 W Xe lamp (2.16 W cm^{-2})	9000	4:1	250	~0.74	0.96	1.24	97.79	[132]
NiCo alloy/Al_2O_3	flow	1.8	300 W Xe lamp (2.16 W cm^{-2})	9000	4:1	250	~0.52	0.29	0.79	99.44	[132]
CoFe/$CoFe_2O_4$	flow	1	300 W Xe lamp (2 W cm^{-2})	7895	4:1	300	1.10	29.8	50	21.2	[133]
Co−CoOx/$MgAl_2O_4$	flow	3	LED (1.2 W cm^{-2})	2400	3:1	325	1.16	35.2	24.3	40.5	[134]
$Cu_{0.65}/Co_{0.35}Fe_2$	flow	1	LED (0.045 W cm^{-2})	14400	3:1	320	~1.6	31.8	56.9	11.3	[135]

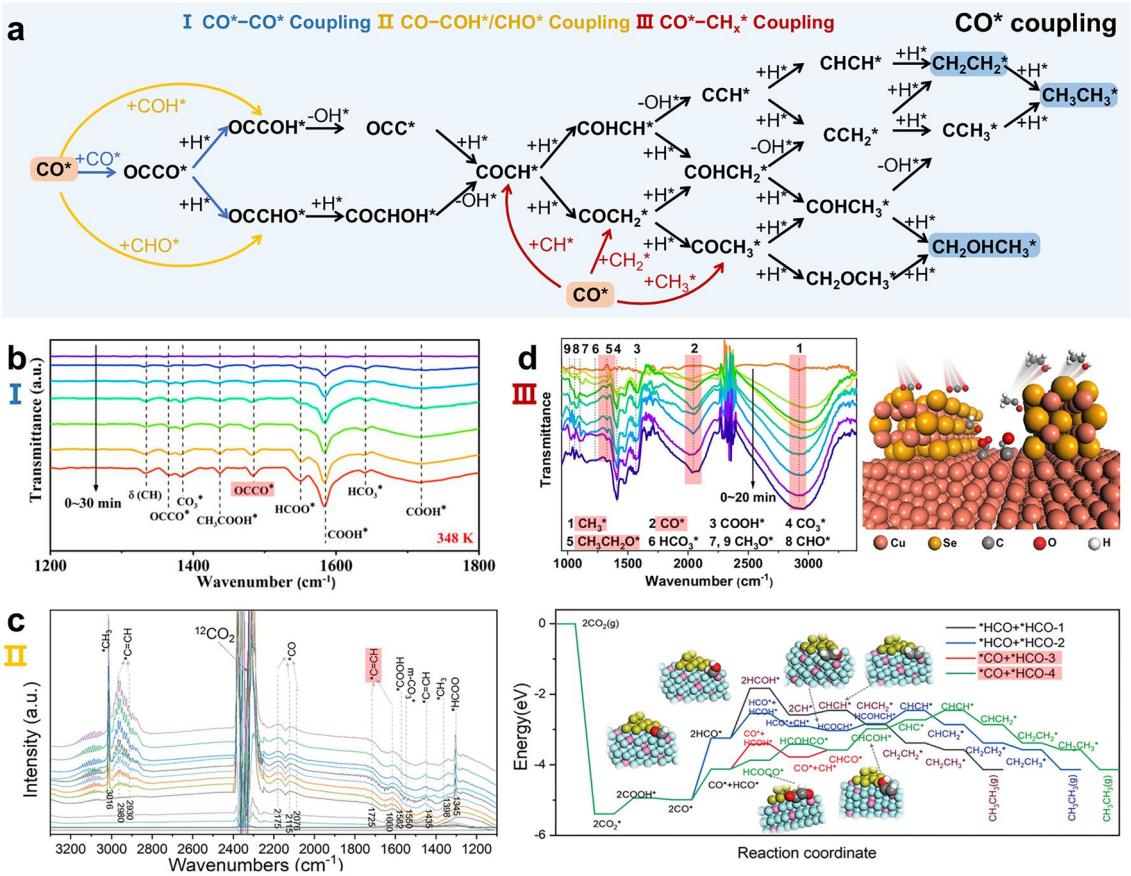


Fig. 7 Reaction pathways for CO_2 hydrogenation to C_2 products via CO* coupling. **a** Possible reaction pathways via CO* coupling. **b** CO*–CO* pathway revealed by in situ DRIFTS. Reproduced with permission from Ref. [137], Copyright 2021 American Chemical Society. **c** CO*–HCO* pathway revealed by in situ DRIFTS and DFT calculations. Reproduced with permission from Ref. [135], Copyright 2024 John Wiley and Sons. **d** CO*–CH_3* pathway revealed by in situ DRIFTS. Reproduced with permission from Ref. [140], Copyright 2024 Springer Nature

and collision, with photoinduced electronic modulation, which optimizes adsorption configuration and charge distribution of CO*-derived species [137].

3.2.2 CH_x* Coupling

In photothermal CO_2 hydrogenation, C_2H_4 and C_2H_6 are typically formed via C–C coupling between CH_x* intermediates (Fig. 8a). On a Co–CoO_x/$MgAl_2O_4$ catalyst, CH* species can couple to form CHCH* during photothermal catalysis, which yield C_2H_4 and C_2H_6 (Fig. 8b) [134]. Similarly, in another study on photothermal CO_2 hydrogenation to C_2 products, CH_2*–CH_2* coupling was identified as the dominant route for carbon chain elongation [127]. In addition, CH_3*–CH_3* coupling has also been proposed as a principal pathway for C_2H_6 formation [123].

Beyond symmetric CH_x* coupling, C–C bond formation can also occur through asymmetric coupling. Tierui Zhang et al. reported a CoFe alloy/Al_2O_3 catalyst, which exhibited high C_2 selectivity in the CO_2 hydrogenation process. According to DFT calculations, the most favorable C–C coupling pathway on the $Co_{11}Fe_5$(110) surface involves the coupling of CH* and CH_2* with an adsorbed barrier of 0.86 eV (Fig. 8c) [128].

In summary, CH_x*-mediated coupling requires a delicate balance between the formation of hydrogenated C_1 intermediates and the suppression of excessive hydrogenation to CH_4. Photothermal catalysis is particularly useful for this route because localized heating can accelerate the generation and migration of CH_x* species, while photoinduced charge redistribution at alloy or metal–oxide interfaces can tune their hydrogenation degree and coupling

© The authors https://doi.org/10.1007/s40820-026-02351-0

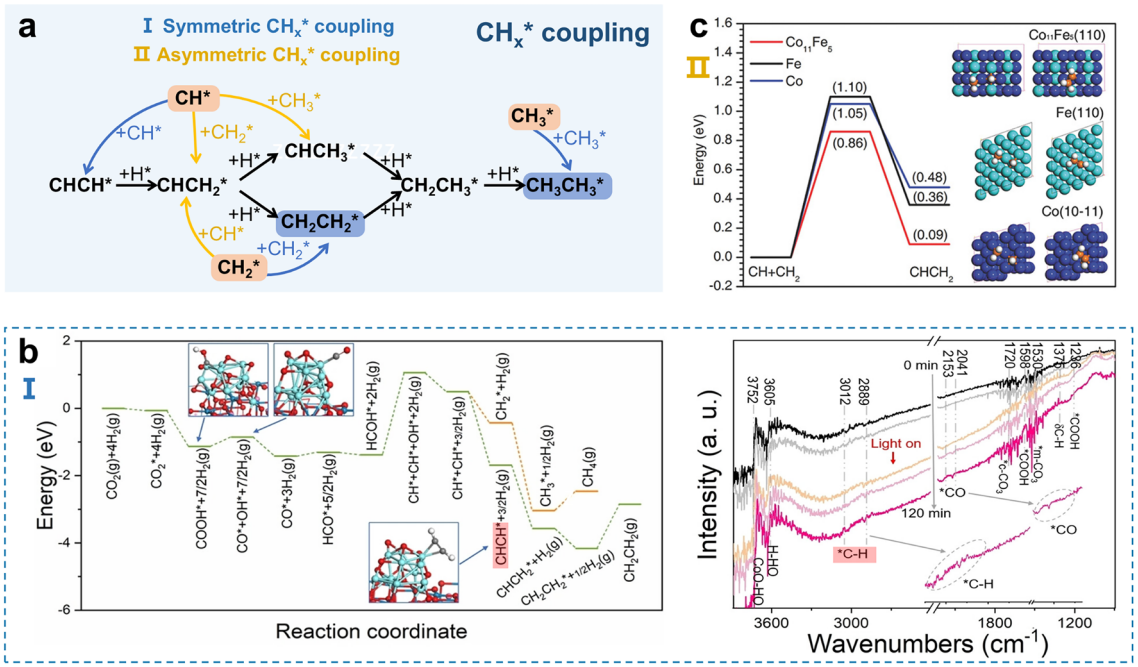


Fig. 8 Reaction pathways for CO_2 hydrogenation to C_2 products via CH_x* coupling. **a** Possible reaction pathways via CH_x* coupling. **b** Symmetric CH*−CH* pathway revealed by in situ DRIFTS and DFT calculations. Reproduced with permission from Ref. [134], Copyright 2023 John Wiley and Sons. **c** Asymmetric CH*−CH_2* pathway revealed by DFT calculations. Reproduced with permission from Ref. [128], Copyright 2017 John Wiley and Sons

tendency. Together with the CO*-mediated route discussed above, these pathways demonstrate that light-induced electronic modulation and localized thermal activation can jointly promote C_1 intermediate formation and subsequent C–C coupling in photothermal CO_2 hydrogenation. To clarify the mechanistic distinction among different coupling routes, Table 5 summarizes their reaction pathway, key intermediates, and representative catalysts.

3.2.3 CH_3OH* Coupling

Unlike the CO*- and CH_x*-mediated routes discussed above, CH_3OH*-mediated C–C coupling has been primarily established in thermal catalysis. The CH_3OH*-mediated pathway is considered an effective route for producing olefins and alkanes, as this pathway circumvents the limitations of the Anderson–Schulz–Flory (ASF) distribution and significantly enhances the selectivity toward higher hydrocarbons [141–143]. Although methanol can clearly be generated through COOH* or HCOO* pathways, subsequent C−C coupling of methanol to form olefins, alkanes, or even aromatics is highly complex. This complexity has sparked ongoing debate over direct versus indirect mechanisms, primarily due to the lack of direct spectroscopic evidence. Consequently, more than twenty reaction pathways have been proposed to account for the formation of these products. Specifically focusing on C_2 product formation, some researchers have suggested that CH_3OH* can couple with another CH_3OH* intermediate via dehydration to form CH_3OCH_3*, which can then undergo hydrogenation and deoxygenation to generate $CHCH_2$* [144, 145]. It has also been reported that CH_3OH* can couple with COOH* to form $HCOOCH_3$*, which subsequently undergoes hydrogenation to produce $CHCH_2$*. This intermediate may then proceed through further hydrogenation and C−C coupling steps to yield aromatic compounds [146, 147]. Additionally, HCOO* intermediate has also been implicated in CH_3OH-mediated C−C coupling reactions [148].

CH_3OH*-mediated CO_2 hydrogenation generally involves a tandem catalytic system. These systems employ bifunctional catalysts composed of metal oxides and zeolites, wherein the metal oxide component facilitates the hydrogenation of CO_2 to methanol, which then diffuses into the zeolite phase for further conversion into multicarbon

Table 5 Reaction pathways from CO_2 activation to C_1 intermediates and C_{2+} products in photothermal CO_2 hydrogenation

Reaction stage	Pathway	Key intermediates	Reported Products	Representative catalysts	Ref.
CO_2 activation to C_1 intermediates	Direct C=O cleavage	CO*, HCO*, COH*, CH_x*	CO, CH_4	AgK/Fe_3O_4, Ru/TiO_2	[64, 84]
	COOH* pathway	CO*, HCO*, COH*, CH_3OH*, CH_x*	CO, CH_3OH, CH_4	Ni/$LaInO_3$, Ru/In_2O_3, Ni/TiO_2	[67, 86, 108]
	HCOO* pathway	HCOOH*, HCO*, H_2COOH*, CH_3OH*, CH_x*	CH_3OH, CH_4	Ir-CoO/Al_2O_3, IrPd-In_2O_3	[91, 111]
C–C coupling to C_{2+} products	CO*-mediated coupling	CO*–CO*, CO*–HCO*, CO*–CHO*, CO*–CH_x*	C_2H_4, C_2H_6, C_2H_5OH	Zn_2GeO_4, Cu/CoFe, Cu_2Se-Cu_2O	[135, 137, 140]
	CH_x*-mediated coupling	CH_x*–CH_x*, CH*–CH_x*, CH_2*–CH_3*	C_2H_4, C_2H_6	Co−CoO_x/$MgAl_2O_4$, CoFe/Al_2O_3	[128, 134]

hydrocarbons. Owing to their well-defined pore structures and abundant Brønsted acid sites, zeolites serve as shape-selective catalysts and play a pivotal role in methanol coupling pathways during thermal CO_2 hydrogenation to higher hydrocarbons [149]. However, incorporating zeolite catalysts into photothermal CO_2 hydrogenation systems remains challenging due to two primary limitations. On the one hand, conventional zeolites, mainly composed of aluminosilicates, possess wide bandgaps and can only absorb ultraviolet light ($\lambda < 400$ nm) [150, 151]. As visible and infrared light account for the majority of solar irradiation, their poor absorption in these regions results in limited photothermal conversion efficiency, making it difficult to reach the temperatures required for efficient photothermal catalysis. On the other hand, photogenerated charge carriers must migrate to the catalyst surface to participate in redox reactions of photothermal catalysis. Previous studies have shown that shorter migration distances promote charge separation, while longer pathways increase the probability of recombination [152]. The extended pore networks in zeolites inherently prolong the migration distance, thereby exacerbating carrier recombination. Additionally, the high electrical resistivity of aluminosilicate zeolites further impedes the effective transport of photogenerated electrons and holes, intensifying recombination losses and diminishing photothermal catalytic performance [153, 154]. Thus, future research should focus on enhancing the photothermal responsiveness of zeolite-based catalysts and improving charge carrier dynamics to enable their broader use in photothermal catalytic systems.

4 Modification Strategies for Photothermal CO_2 Hydrogenation Catalysts

Based on pathways discussed above, both product yield and selectivity toward C_{2+} hydrocarbons are predominantly governed by two key steps: CO_2 activation to C_1 intermediates and subsequent C−C coupling of these intermediates. Accordingly, we propose a series of modification strategies aimed at improving reaction performance by facilitating the activation of CO_2 to C_1 species and promoting efficient C−C coupling (Fig. 9).

4.1 Facilitating CO_2 Activation to C_1 Products

4.1.1 Control of Morphology

In photothermal CO_2 hydrogenation, catalyst morphology plays a pivotal role in determining both the photothermal conversion efficiency and the efficiency of reactant activation. By tailoring the surface properties and microstructure of the catalyst, it is possible to significantly enhance solar-to-thermal energy conversion as well as increase the number of accessible active sites. Such morphology optimization strategies offer new opportunities for realizing efficient CO_2 hydrogenation into C_1 products.

(1) Photothermal conversion efficiency

To maximize photothermal conversion efficiency, catalysts should achieve strong solar light absorption while

© The authors
https://doi.org/10.1007/s40820-026-02351-0

minimizing thermal radiation losses under illumination [155–157]. Morphological modifications have proven effective in boosting photothermal efficiency. Hierarchical porous structure of K^+−Co−C can enhance photon trapping and scattering within the bulk, thereby increasing local temperature under light intensity and ultimately improving photothermal reaction performance (Fig. 10a) [81]. The unique hierarchical structures of nanocages enable Ru-loaded carbon nanocages achieved nearly 90% light absorption across the solar spectrum. Under 2.4 W cm^{-2} light irradiation, the catalyst exhibited a record CO production rate of 3.1 mol g_{Ru}^{-1} h^{-1} in flow reactor, with selectivity exceeding 90% [158].

Beyond enhancing light absorption, morphological control also helps reduce thermal emissivity. In Janus-structured Ru@m-$Ti_3C_2T_x$ materials for photothermal CO_2 methanation, the smooth side exhibited a remarkably low mid-infrared emissivity (~21%), which effectively suppressed radiative heat loss and enabled localized heat accumulation, while the porous side facilitated reactant diffusion and product transport, together leading to enhanced CH_4 yields (Fig. 10b) [92].

(2) Reactant activation capability

Catalyst morphology also plays a key role in reactant activation, as both surface and internal regions typically serve as primary sites for CO_2 and H_2 activation. Increasing the specific surface area is a widely used strategy to improve reactant adsorption and activation. Compared with bulk materials, nanostructured catalysts offer significantly higher surface areas and a greater number of active sites, thus enhancing reactant activation capability. Nanostructured bismuthene sheets exhibited a photothermal CO_2 hydrogenation activity 4.6 times higher than that of commercial bulk bismuth (Fig. 10c) [159].

Porous materials are promising for photothermal CO_2 hydrogenation because their tailored pore structures can simultaneously improve reactant adsorption, mass transport, and active-site dispersion [160]. For example, a Pd-loaded hierarchically porous titanium-based metal–organic framework (Pd/hMUV-10) achieved a CO yield of 65.9 mmol g^{-1} h^{-1} under photothermal conditions at 350 °C. Its performance was attributed to the etching-generated mesoporous structure, which enhanced CO_2 adsorption and activation, and to the hierarchical pore network, which facilitated

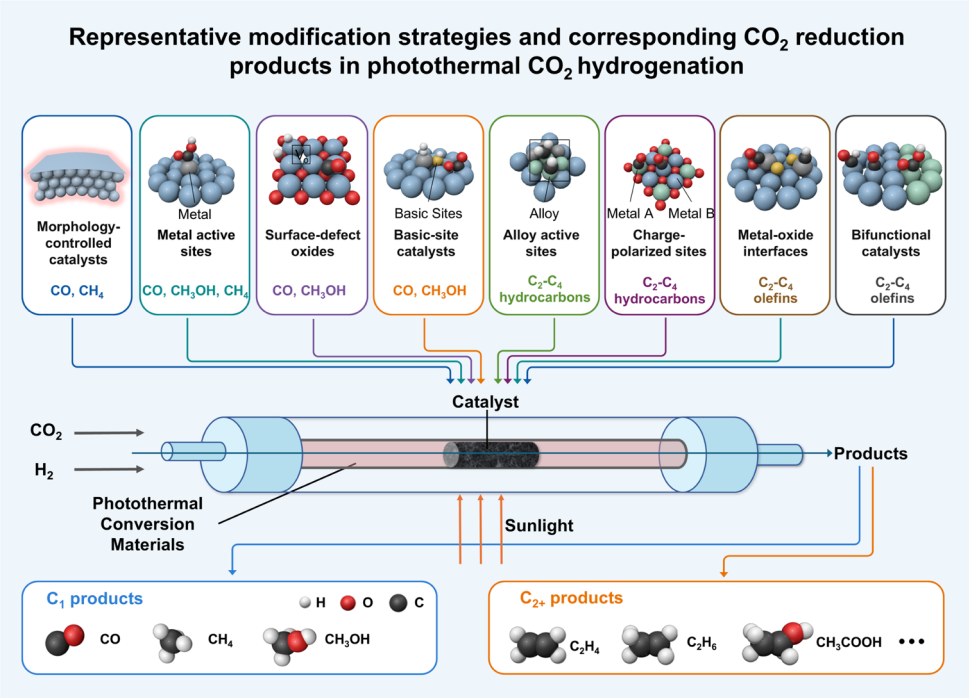


Fig. 9 Representative modification strategies and corresponding CO_2 reduction products in photothermal CO_2 hydrogenation

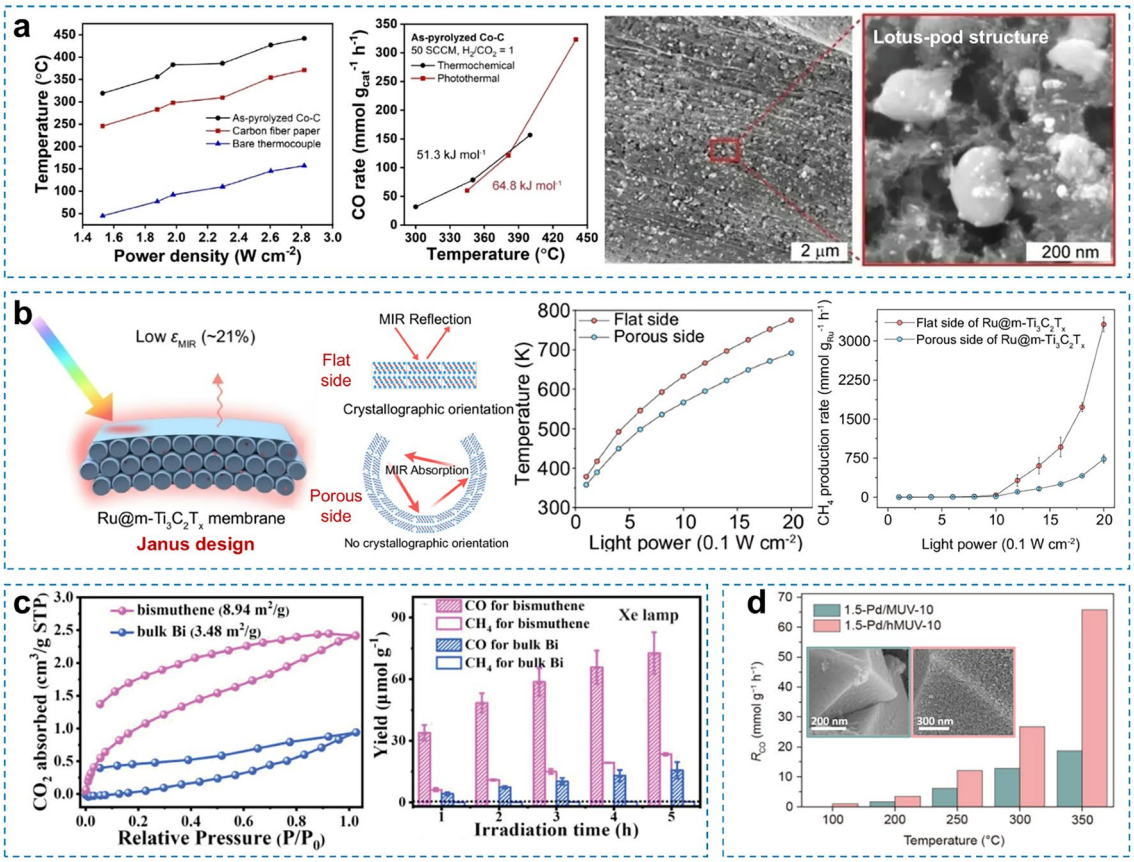


Fig. 10 Effect of morphology control on facilitating the activation of CO_2 to C_1 products. **a** Light absorption enhancement by hierarchical porous-structured K^+−Co−C. Reproduced with permission from Ref. [81], Copyright 2023 John Wiley and Sons. **b** Thermal radiation suppression by smooth side of Janus-structured Ru@m-$Ti_3C_2T_x$. Reproduced with permission from Ref. [92], Copyright 2024 Springer Nature. **c** Specific surface area increases by bismuthene nanosheets. Reproduced with permission from Ref. [159], Copyright 2024 John Wiley and Sons. **d** Porous-structured construction by Pd/hMUV-10 with hierarchical mesopores. Reproduced with permission from Ref. [161], Copyright 2023 Springer Nature

uniform Pd dispersion across both internal and external surfaces (Fig. 10d) [161].

In summary, morphology control mainly strengthens the physical basis of photothermal catalysis by improving light absorption, heat localization, reactant diffusion, and active-site exposure. Nevertheless, these effects primarily facilitate upstream CO_2 activation and do not necessarily ensure selective product formation. Therefore, morphology optimization should be integrated with chemical active-site design to achieve more efficient and selective CO_2 hydrogenation.

4.1.2 Construction of Basic Sites

Basic sites, including alkali metals, alkaline earth metals, and certain transition metal oxides, are widely introduced to enhance CO_2 activation in photothermal hydrogenation. Owing to their intrinsic basicity, alkali and alkaline earth promoters strengthen the interaction between CO_2 and catalyst surface, thereby facilitating CO_2 activation. By contrast, transition metal oxides generally promote reactant activation through electronic modulation of catalyst surface.

(1) Alkali metals

Alkali metal promoters can donate electron density to the catalyst surface and strengthen the electrostatic interaction with adsorbed CO_2*, thereby facilitating CO_2 adsorption and activation. Jorge Gascon et al. investigated a series of alkali metal-promoted In_2O_3 catalysts for selective photothermal CO_2 hydrogenation to CO and found that Cs-promoted In_2O_3 exhibited the highest catalytic activity. This enhancement

© The authors https://doi.org/10.1007/s40820-026-02351-0

was attributed to strong electronic effects induced by Cs. Moreover, the surface temperatures of K-, Rb-, and Cs-promoted In_2O_3 catalysts were over 30 °C higher than that of pristine In_2O_3, indicating that alkali metal promoters also contribute to improved photothermal conversion efficiency (Fig. 11a) [74].

(2) Transition metal oxides

Certain transition metal oxides can serve as basic active sites by modulating surface charge density, thereby enhancing reactant activation. In Cu/CeO_2 catalysts, the introduction of Ga_2O_3 altered the electronic structure and facilitated the reduction of CeO_2, resulting in a higher concentration of oxygen vacancies that promote CO_2 adsorption. In addition, Ga_2O_3 played a critical role in enabling hydrogen spillover, which accelerated the conversion of adsorbed carbonates into formates. These effects collectively contributed to the enhanced photothermal reverse water–gas shift (RWGS) performance (Fig. 11b) [77].

Basic sites enhance CO_2 activation by strengthening catalyst–CO_2 interactions and regulating surface electronic structure. However, excessive basicity may lead to strongly adsorbed carbonate species and slow intermediate conversion. Thus, efficient catalyst design requires a balance between CO_2 adsorption strength, H_2 activation ability, and photothermal energy utilization.

4.1.3 Creation of Surface Defects

Surface defect engineering strategies, particularly the introduction of oxygen vacancies and the creation of surface-frustrated Lewis pairs (SFLPs), hold significant promise for enhancing photothermal CO_2 hydrogenation.

(1) Oxygen vacancies

The beneficial role of oxygen vacancies in promoting C_1 product formation can be attributed to two main mechanisms. First, they enhance photothermal conversion by introducing mid-gap states and narrowing the band gap, thereby broadening solar absorption and facilitating photon utilization (Fig. 12a) [162]. Second, they substantially promote reactant activation, particularly for CO_2 [108, 160]. Under reaction conditions, oxygen atoms from CO_2 can fill oxygen vacancy sites by integrating into bridge-bonded oxygen, effectively healing the defect [163]. This process lowers the CO_2 activation barrier due to strong attraction between oxygen vacancies and O atoms in CO_2, thus facilitating CO_2 activation. In addition, oxygen vacancies can trap photogenerated electrons, suppress charge recombination, and improve charge separation [162]. On black In_2O_{3-x} nanosheets, oxygen vacancies generated localized electrons that were transferred to the antibonding orbitals of CO_2, thereby stabilizing intermediates and facilitating CO_2 activation. DFT calculations further revealed that oxygen vacancies reduced the dissociative adsorption energy of H_2, promoting its activation and subsequent CO_2 hydrogenation (Fig. 12b) [71].

However, oxygen vacancies may also introduce stability issues. Specifically, incorporation of oxygen atoms from CO_2 into surface oxygen vacancies may hinder product desorption [164], and the continuous consumption of oxygen vacancies during reaction can lead to catalyst deactivation over time [165]. Therefore, future efforts should focus on strategies to enhance the durability and regeneration of oxygen vacancies in photothermal CO_2 hydrogenation systems.

(2) Surface-frustrated Lewis pairs

Metal oxides usually contain surface Lewis acid–base pairs, but these sites often form stable Lewis adducts that are inactive toward CO_2 activation. Introducing structural defects, especially oxygen vacancies, can disrupt local lattice order and expose adjacent Lewis acid–base sites. When the distance between these sites is appropriately regulated, typically around 4 Å, SFLPs can form and become active for small-molecule activation.

In oxide-based SFLPs, the Lewis basic sites are often hydroxyl groups coordinated to metal atoms, while the Lewis acidic sites are coordinatively unsaturated metal cations (created by oxygen vacancies). Geoffrey A. Ozin et al. have conducted a series of studies investigating how SFLPs facilitate CO_2 and H_2 activation during photothermal CO_2 hydrogenation. In $In_2O_{3-x}(OH)_y$ (2015), adjacent hydroxyl groups and indium cations associated with oxygen vacancies formed molecular SFLPs that could heterolytically cleave H_2 and reversibly adsorb CO_2, enabling its conversion to CO (Fig. 13a) [70]. In 2016, In and InOH SFLPs were identified as active sites responsible for CO_2 activation to CO (Fig. 13b) [166, 167]. In 2018, beyond CO production, the SFLP InOH···In in rod-shaped $In_2O_{3-x}(OH)_y$ nanocrystal

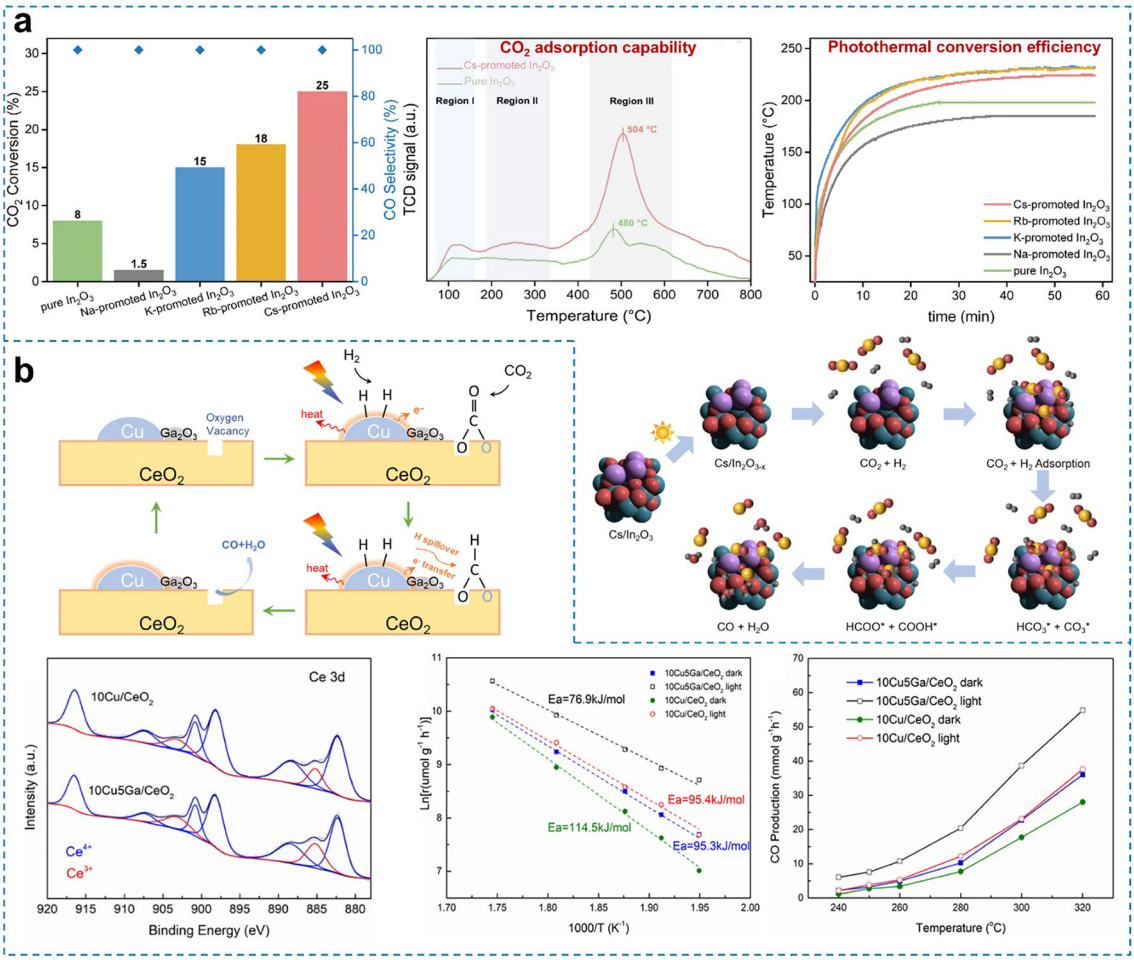


Fig. 11 Effect of basic sites on facilitating the activation of CO_2 to C_1 products. **a** Alkali metal introduction in Cs-promoted In_2O_3. Reproduced with permission from Ref. [74], Copyright 2024 The Royal Society of Chemistry. **b** Transition metal oxides incorporation in 10Cu5Ga/CeO_2. Reproduced with permission from Ref. [77], Copyright 2021 Elsevier

superstructures was found to facilitate CO_2 hydrogenation to CH_3OH under ambient pressure (Fig. 13c) [110]. In 2019, tuning the Lewis acidity and basicity of SFLPs through polymorph selection was found to regulate both activity and selectivity in photothermal CO_2 hydrogenation (Fig. 13d) [113]. More recently, CH_3OH production over $H_zIn_2O_{3-x}(OH)_y$ was proposed to proceed through a tandem mechanism in which SFLPs, InOH···In sites, first heterolytically dissociated H_2, followed by CO_2 activation and conversion via the COOH* pathway. More importantly, the oxygen vacancy sites could be regenerated after CH_3OH desorption, contributing to catalyst stability (Fig. 13f) [120]. Recently, Miao et al. further extended the SFLP concept beyond In_2O_3-based systems by showing that dynamic surface reconstruction of plasmonic Pt/TiN generated an oxygen vacancy-rich TiO_x shell, where surface oxygen vacancies and hydroxyl groups formed SFLPs that promoted CO_2 adsorption and activation under photothermal conditions [168].

Besides hydroxyl-containing SFLPs, another SFLP type consists of coordinatively unsaturated metal cations as Lewis acidic sites and adjacent lattice oxygen atoms as Lewis basic sites [169]. In $Bi_xIn_{2-x}O_3$ (2020), isomorphic substitution of In^{3+} by Bi^{3+} generated Bi^{3+}–O^{2-} SFLPs that strongly polarized H_2 and promoted its dissociation into H* species, thereby promoting reactant activation (Fig. 13e) [114].

Overall, the activity of SFLPs originates from their cooperative dual-site character: Lewis acidic sites interact with the oxygen atoms of CO_2, whereas Lewis basic sites

© The authors https://doi.org/10.1007/s40820-026-02351-0

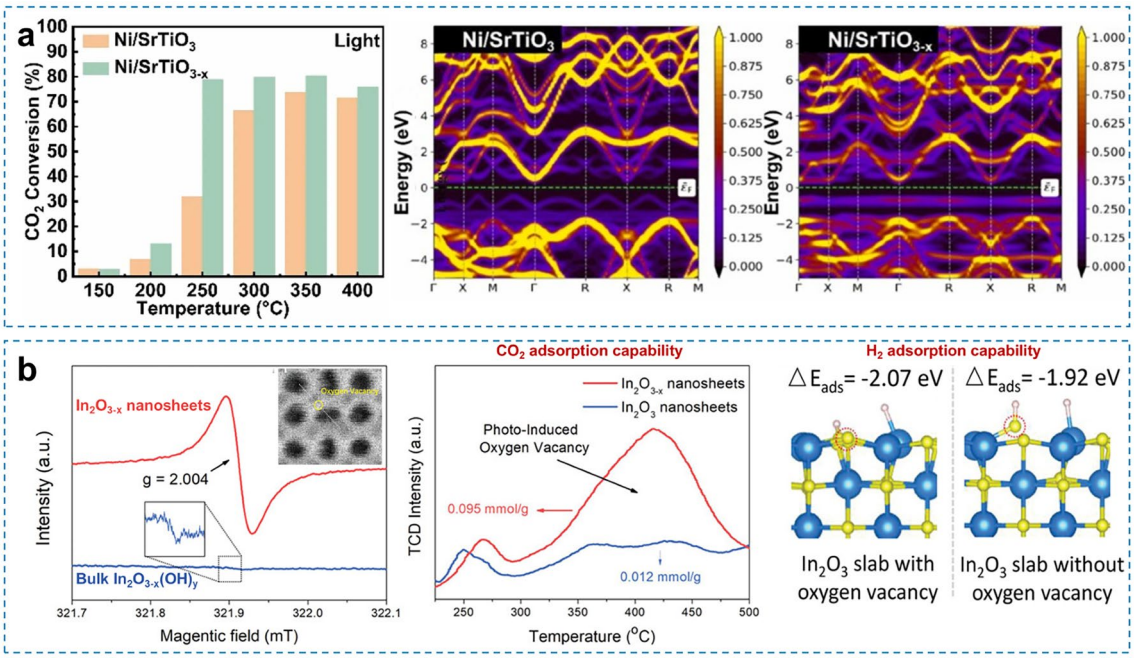


Fig. 12 Effect of surface defects on facilitating the activation of CO_2 to C_1 products. **a** Oxygen vacancy creation in Ni/$SrTiO_{3-x}$. Reproduced with permission from Ref. [162], Copyright 2024 Elsevier. **b** Oxygen vacancy creation in In_2O_{3-x} nanosheets. Reproduced with permission from Ref. [71], Copyright 2019 John Wiley and Sons

facilitate polarization of the carbon-centered bonds or H_2, thereby lowering the activation barrier for subsequent reactions. Although SFLPs are highly promising for defect engineering, achieving stable and durable SFLP configurations under photothermal reaction conditions remains a key challenge.

4.1.4 Introduction of Metal Active Sites

Introducing metal active sites can promote CO_2 activation through strong orbital interactions with adsorbed molecules and facilitate H_2 dissociation by modulating the local electronic structure, thereby enhancing reactant activation in photothermal CO_2 hydrogenation. In some cases, metal active sites can also induce LSPR effects under light irradiation, generating localized heating and further improving photothermal catalytic performance.

(1) Noble metal active sites

Among the various candidates, noble metals have been most extensively explored because of their outstanding ability to promote both charge transfer and reactant activation. Ir nanoparticles confined within the UiO-66 framework enabled efficient photothermal CO_2 hydrogenation to CH_4, achieving a production rate of 19.9 mmol g_{cat}^{-1} h^{-1} by promoting charge separation and transfer, thereby accelerating H_2 dissociation and CO_2 activation [104].

In addition to facilitating reactant activation, noble metal active sites can also enhance photothermal conversion through plasmonic effects. In an Au-grafted $Ce_{0.95}Ru_{0.05}O_2$ solid solution catalyst, $Ce_{0.95}Ru_{0.05}O_2$ acted as a broadband light absorber to provide localized photothermal heating, while Au nanoparticles introduced visible-light LSPR at the Au/$Ce_{0.95}Ru_{0.05}O_2$ interface. The role of Au was not simply assigned to additional heating, because $Au_{0.1}$/$Ce_{0.95}Ru_{0.05}O_2$ and $Ce_{0.95}Ru_{0.05}O_2$ exhibited comparable surface temperatures under identical illumination. Arrhenius analysis showed similar apparent activation energies but an approximately 6–8-fold increase in the pre-exponential factor after Au loading, suggesting an increased number of effective active sites rather than pure Arrhenius thermal acceleration. Further analysis showed that LSPR-induced hot-electron injection promoted the formation of Ru–oxygen vacancy active centers, thereby enhancing CO_2 methanation and enabling a CH_4 yield of approximately 86%,

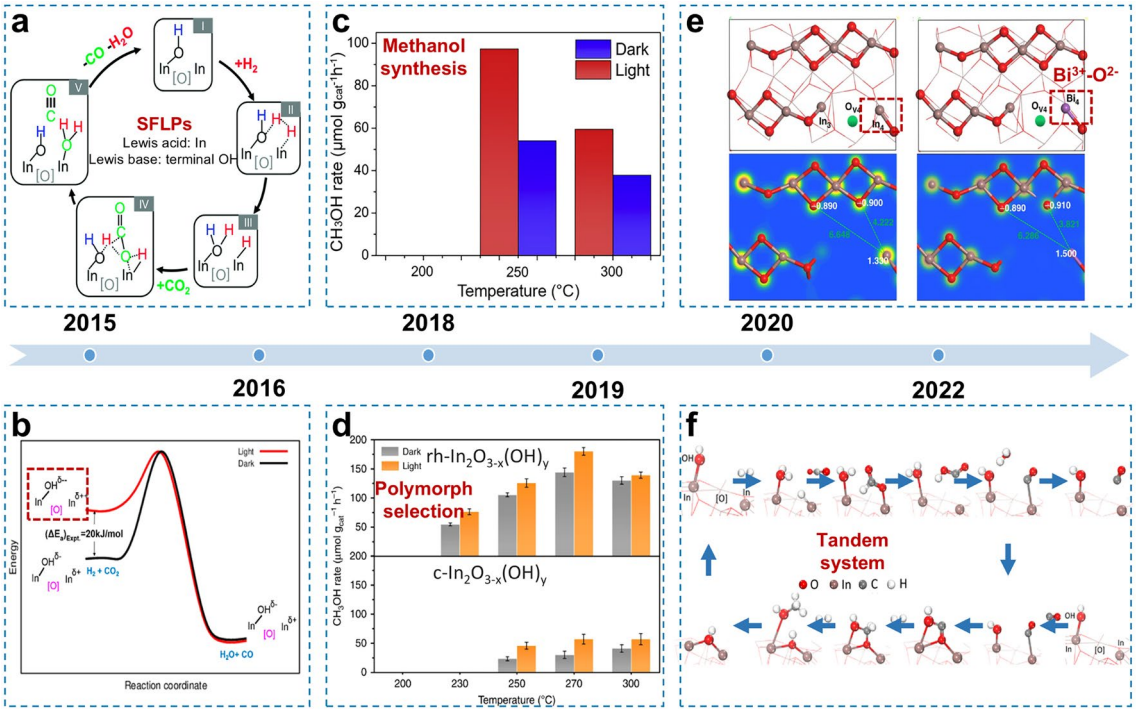


Fig. 13 A brief overview of SFLP application in photothermal CO_2 hydrogenation from the group of Geoffrey A. Ozin. **a** Proposed mechanism of SFLPs in $In_2O_{3-x}(OH)_y$. Reproduced with permission from Ref. [70], Copyright 2015 The Royal Society of Chemistry. **b** Experimental and theoretical elucidation of SFLPs in $In_2O_{3-x}(OH)_y$. Reproduced with permission from Ref. [167], Copyright 2016 American Chemical Society. **c** Promotion of photothermal CO_2 to CH_3OH by SFLPs $In_2O_{3-x}(OH)_y$ nanocrystal superstructure. Reproduced with permission from Ref. [110], Copyright 2018 Elsevier. **d** Regulation of SFLPs acidity basicity via polymorph selection of $In_2O_{3-x}(OH)_y$. Reproduced with permission from Ref. [113], Copyright 2019 Springer Nature. **e** Promotion of photothermal CO_2 to CH_3OH by SFLPs Bi^{3+}–O^{2-} pairs in $Bi_xIn_{2-x}O_3$. Reproduced with permission from Ref. [114], Copyright 2020 Springer Nature. **f** Tandem photothermal CO_2 hydrogenation to CH_3OH enabled by SFLPs (InOH···In) in $H_zIn_2O_{3-x}(OH)_y$. Reproduced with permission from Ref. [120], Copyright 2022 Springer Nature

close to the thermodynamic limit (Fig. 14a) [44]. A similar LSPR-assisted promotion was also reported for Ru/In_2O_3 in photothermal CO_2 hydrogenation to methanol, where LSPR-induced hot carriers enhanced both surface heating and reactant activation [108].

(2) Transition metal active sites

Despite their high activity, the limited abundance and high cost of noble metals have driven increasing interest in transition metal alternatives. In this regard, transition metal active sites can also effectively regulate surface electronic structure and promote key elementary steps in photothermal CO_2 hydrogenation. For instance, In_2O_3@Ni with uniformly dispersed Ni sites was reported to selectively catalyze CO_2 hydrogenation to CH_4, where the isolated Ni centers enhanced CO_2 activation by modulating the surface electronic structure of In_2O_3, while also lowering the barrier for H_2 dissociation to provide reactive hydrogen species (Fig. 14b) [93].

Furthermore, when Ni species present as metallic nanoparticles, they not only facilitated reactant mass transfer but also served as local thermal hotspots via the LSPR effect, providing an additional contribution to photothermal catalytic performance [170, 171].

Metal active sites enhance photothermal CO_2 hydrogenation by improving H_2 dissociation, CO_2 activation, interfacial charge transfer, and, in some systems, plasmon-assisted light utilization. Noble metals usually show higher intrinsic activity, whereas transition metals provide lower-cost alternatives with tunable electronic structures. Nevertheless, metal aggregation, uncertain active-state evolution, and the difficulty in distinguishing thermal and electronic contributions remain important challenges. Therefore, future studies should combine metal-site stabilization with operando characterization and temperature-matched controls.

© The authors
https://doi.org/10.1007/s40820-026-02351-0

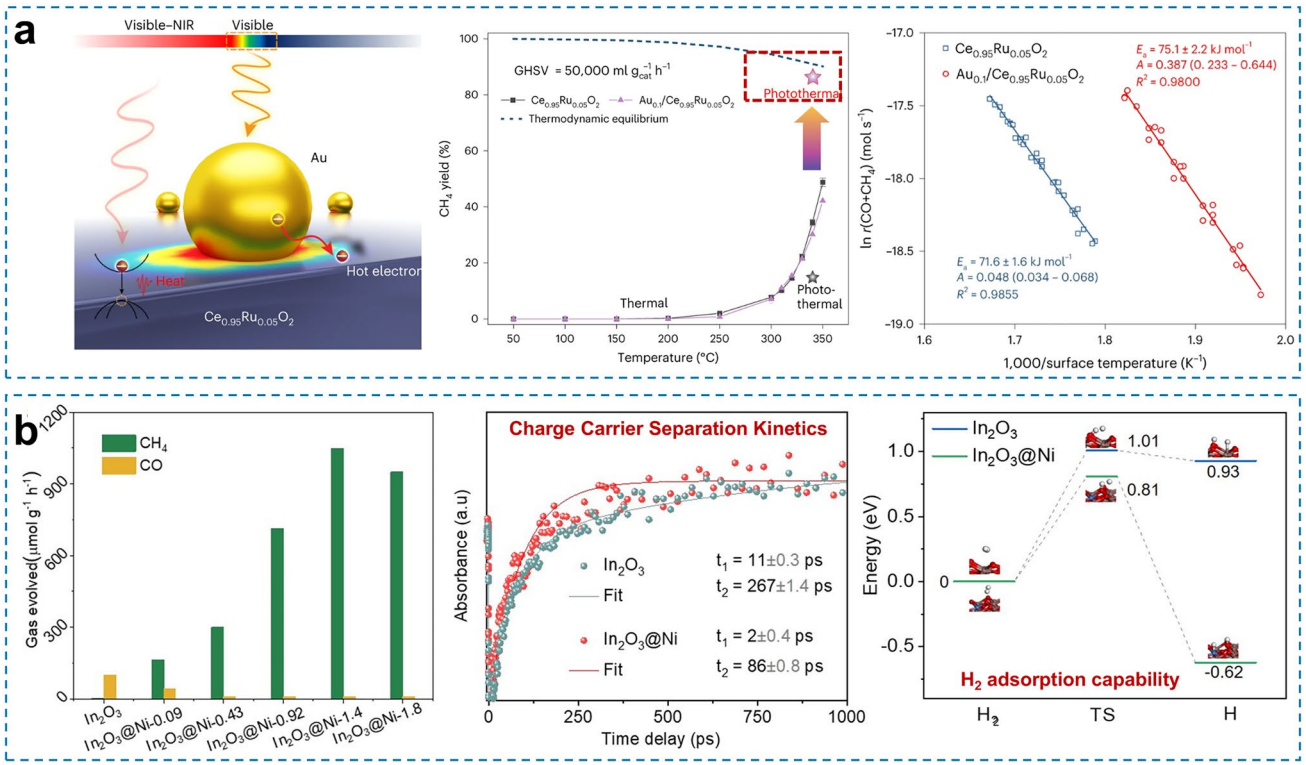


Fig. 14 Effect of metal active sites on facilitating the activation of CO_2 to C_1 products. **a** Introduction of noble metal active sites Au in $Ce_{0.95}Ru_{0.05}O_2$. Reproduced with permission from Ref. [44], Copyright 2023 Springer Nature. **b** Anchoring of transition metal active sites Ni onto In_2O_3. Reproduced with permission from Ref. [93], Copyright 2024 American Chemical Society

4.2 Promoting C−C Coupling of C_1 Intermediates to C_{2+} Products

The coupling of C_1 intermediates to form C−C bonds is a key step governing both the rate and selectivity of C_{2+} products in photothermal CO_2 hydrogenation. Accordingly, catalyst design has increasingly focused on strengthening C−C coupling along distinct C_1-mediated pathways to produce multicarbon products.

4.2.1 CO Coupling*

Achieving efficient C_2 product formation through the CO*-mediated pathway requires not only sufficient CO* coverage, but also favorable adsorption configurations and electronic environments for subsequent C−C coupling. Accordingly, current catalyst design strategies have mainly focused on alloy active sites, charge-polarized dual-active centers, and bifunctional catalyst systems.

(1) Fabrication of alloy active sites

Alloying is an effective strategy for promoting C_{2+} formation as the introduction of a secondary metal can tune the electronic and geometric structure of the host metal, thereby strengthening CO_2 adsorption and facilitating its conversion to CO* intermediates [172]. The resulting increase in surface CO* coverage is beneficial for subsequent C−C coupling. In AuCu alloy nanoparticles supported on g-C_3N_4 nanosheets, the alloy interface played a central role in regulating the surface electronic structure, leading to electron enrichment at Cu sites and therefore more efficient activation of CO_2 to CO. Coupled with accelerated carrier migration at the alloy–support interface and the higher collision frequency of CO* intermediates under photothermal heating, this alloying effect promoted CO*−CO* coupling and enhanced ethanol production (Fig. 15a) [136].

(2) Design of charge-polarized dual-active sites

Charge-polarized dual-active sites can facilitate C−C bond formation by creating asymmetric electronic environments that reduce the electrostatic repulsion between neighboring C_1 intermediates [173–176]. In an In−S_V−Bi active site, the rational spatial arrangement and asymmetric electronic environment between In and Bi atoms facilitated the coupling of CO* intermediates into OCCO*, lowering energy barriers for both CO_2 activation and C−C coupling [177]. In oxygen vacancy-rich Zn_2GeO_4 nanobelts, quasi-in situ Raman spectroscopy directly identified Zn−O−Ge as active site for photothermal catalysis, enabling simultaneous CO_2 adsorption on both Zn and Ge atoms. The presence of oxygen vacancies further amplified the electronic asymmetry of these Zn−O−Ge sites, resulting in uneven charge distribution across neighboring CO* species. Combined with the higher collision probability of CO* intermediates under photothermal heating, this vacancy-enhanced asymmetry facilitated C−C coupling and favored acetate formation, affording an acetate selectivity of 66.9% and a CO_2 conversion ratio of 29.95% (Fig. 15b) [137].

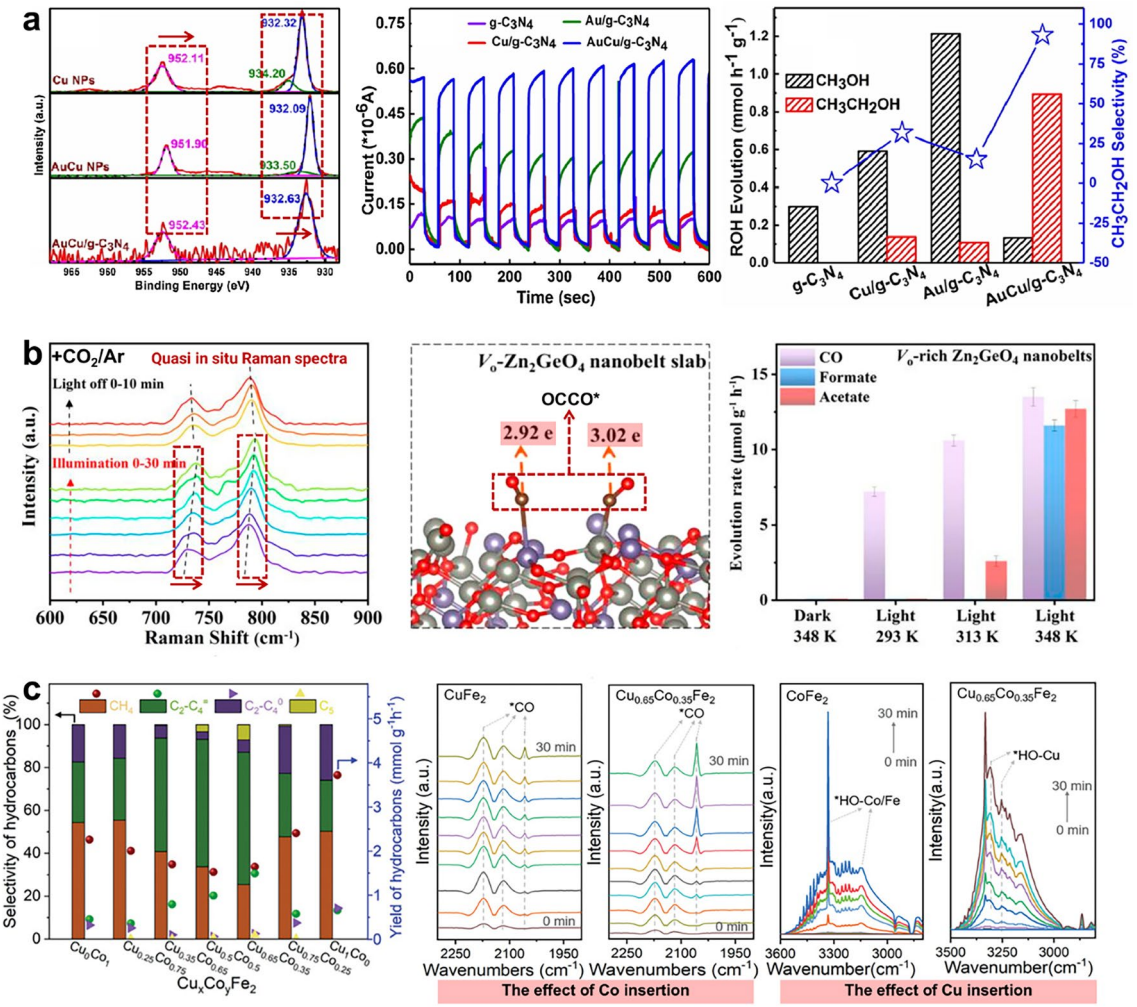


Fig. 15 Surface optimization strategies for promoting C−C coupling of C_1 intermediates via CO* coupling. **a** Fabrication of AuCu alloy sites to facilitate CO*−CO* coupling. Reproduced with permission from Ref. [136], Copyright 2020 Elsevier. **b** Design of charge-polarized Zn−O−Ge to promote CO*−CO* coupling. Reproduced with permission from Ref. [137], Copyright 2021 American Chemical Society. **c** Construction of bifunctional catalyst Cu/CoFe to promote CO*−HCO* coupling. Reproduced with permission from Ref. [135], Copyright 2024 John Wiley and Sons

© The authors https://doi.org/10.1007/s40820-026-02351-0

(3) Construction of bifunctional catalysts

The synergy between two complementary functions is particularly beneficial for C_{2+} olefin formation, especially when one component promotes the generation and coupling of carbon-containing intermediates, while the other suppresses excessive hydrogenation. This cooperative effect was realized in a Cu-promoted CoFe alloy catalyst, which delivered a C_{2+} hydrocarbon selectivity of 73.7%, including 56.5% selectivity toward C_2−C_4 olefins. In this system, Cu enhanced CO_2 adsorption and facilitated hydrogen spillover, which modulated the surface hydrogenation behavior and inhibited further hydrogenation of carbon-containing intermediates. Meanwhile, Co in the CoFe alloy favored bridged CO* adsorption and, together with Fe, provided stable sites for C_1 intermediate coupling, thereby promoting C−C bond formation and favoring C_2−C_4 olefin production (Fig. 15c) [135].

In summary, CO*-mediated coupling is highly dependent on sufficient CO* coverage and suitable adsorption configurations. Alloying, charge-polarized dual-active sites, and bifunctional catalyst design can enhance this process by regulating CO_2 activation, CO* adsorption, interfacial charge distribution, and hydrogenation behavior. Nevertheless, the key challenge is to avoid either excessive CO* stabilization or rapid hydrogenation to C_1 products. Thus, effective CO* coupling catalysts should simultaneously promote CO* formation, maintain appropriate intermediate mobility, and provide favorable sites for C–C bond formation.

4.2.2 CH_x Coupling*

As one of the most extensively investigated routes toward C_{2+} products in photothermal CO_2 hydrogenation, the CH_x*-mediated pathway places demands on both the surface availability of CH_x* intermediates and the catalytic environment required for their subsequent coupling. In response, catalyst design has been directed mainly toward metal–oxide interfaces, alloy active sites, and charge-polarized dual-active sites.

(1) Formation of metal–oxide interfaces

The formation of metal–oxide interfaces can reshape interfacial charge transfer and thereby favor C−C coupling in photothermal CO_2 hydrogenation. In a K−Ru/Fe_3O_4 catalyst, while CO_2 activation and hydrogenation predominantly occurred on Ru sites, Ru−FeO_x interface served as the key site for C_{2+} product generation. Upon light irradiation, photoexcited electrons in Fe_3O_4 were transferred across the Ru−FeO_x interface to Ru, increasing electron accumulation at the interface and promoting C−C coupling (Fig. 16a). Meanwhile, K not only facilitated the construction of the Ru−FeO_x interface but also increased its electron density, which lowered the charge state of Ru, ultimately improving C_2H_4 selectivity [127].

(2) Fabrication of alloy active sites

Tuning the interaction between the catalyst surface and CH_x* intermediates is crucial for promoting C−C coupling toward C_{2+} hydrocarbons. In this regard, CoFe alloy sites are particularly effective because alloying modifies the electronic structure relative to monometallic Co or Fe, optimizes the adsorption strength of CH_x* species, and thus favors the balance between intermediate stabilization and further hydrogenation [178]. In a CoFe catalyst derived from CoFeAl-layered double-hydroxide nanosheets, this electronic modulation lowered the barrier for the CH*−CH_2* coupling step compared with individual Co, Fe, or their physical mixtures, leading to more efficient C−C bond formation (Fig. 16b) [128]. Within a CoFe/$CoFe_2O_4$ heterostructure, CoFe alloy sites also played an important role in promoting C_2−C_4 hydrocarbon formation, giving a production rate of 1.1 mmol g^{-1} h^{-1} with 29.8% selectivity at a CO_2 conversion of 12.9% under ambient pressure. In this system, CO_2 activation occurred on $CoFe_2O_4$ to form adsorbed CO_2* species, while the CoFe alloy promoted hydrocarbon chain growth via C−C coupling (Fig. 16c) [133].

(3) Design of charge-polarized dual-active sites

Charge-polarized dual-active sites can effectively promote CH_x*-mediated C−C coupling by maintaining a sufficiently high surface population of CH_x* intermediates while suppressing their excessive hydrogenation. This balance was effectively achieved on $MgAl_2O_4$-supported Co^0−$Co^{\delta+}$ dual sites, where light irradiation enabled a C_2−C_4 hydrocarbon production rate of 1303 μmol g^{-1} h^{-1} with a carbon selectivity of 62.5%. The electronic contrast between Co^0 and $Co^{\delta+}$ sites shifted the reaction pathway from HCOO* to COOH*,

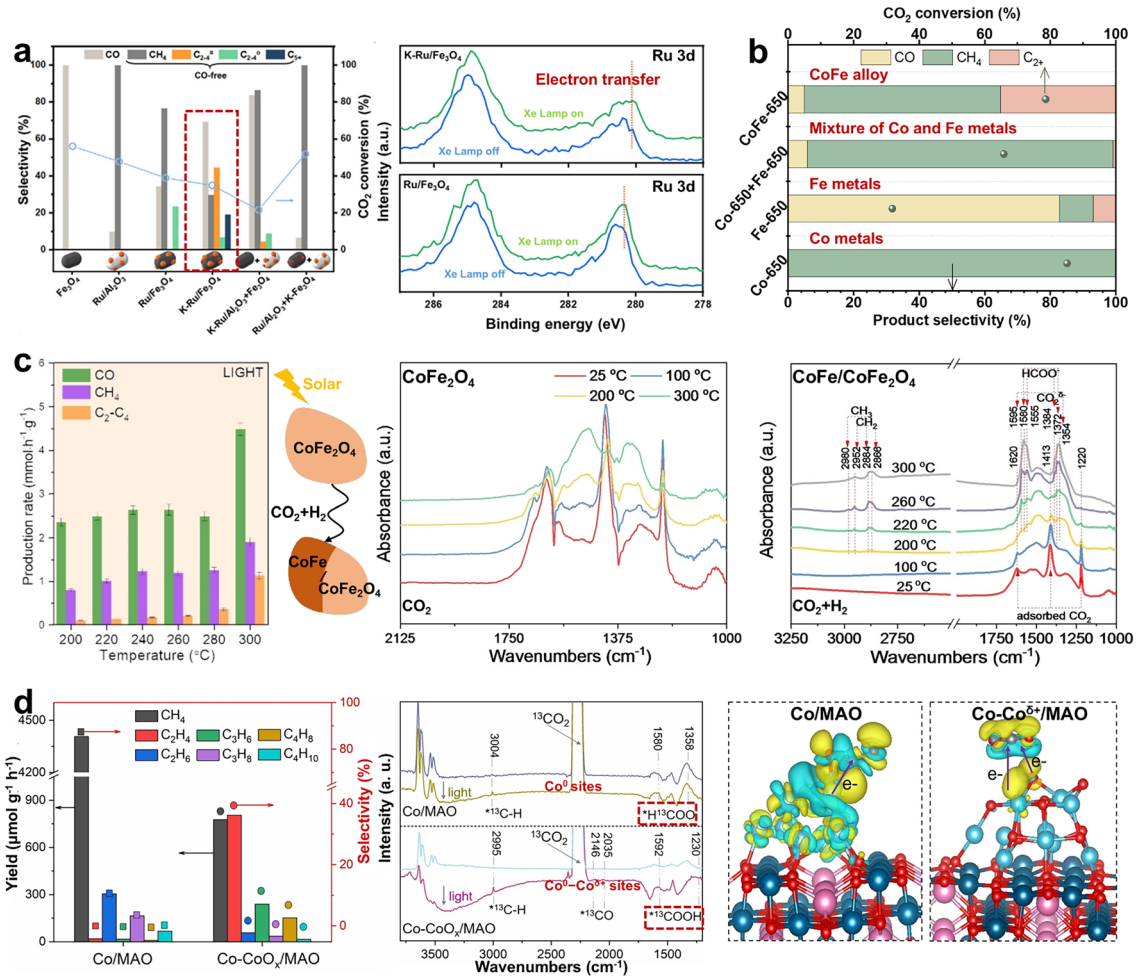


Fig. 16 Surface optimization strategies for promoting C−C coupling of C_1 intermediates via CH_x* coupling. **a** Formation of Ru−FeO_x interface to facilitate CH_2*−CH_2* coupling. Reproduced with permission from Ref. [127], Copyright 2024 Elsevier. **b** Fabrication of CoFe alloy active sites to facilitate CH*−CH_2* coupling. Reproduced with permission from Ref. [128], Copyright 2017 John Wiley and Sons. **c** Fabrication of CoFe alloy active sites to facilitate C−C coupling. Reproduced with permission from Ref. [133], Copyright 2023 John Wiley and Sons. **d** Design of charge-polarized Co^0−$Co^{\delta+}$ to facilitate CH*−CH* coupling. Reproduced with permission from Ref. [134], Copyright 2023 John Wiley and Sons

thereby favoring olefin formation. In this system, Co^0 promoted CO_2 adsorption and activation to generate C_1 intermediates, whereas electron-deficient $Co^{\delta+}$ lowered the barrier for CHCH* formation and, by withdrawing electron density from neighboring Co^0 sites, inhibited the over-hydrogenation of CH_x* intermediates (Fig. 16d) [134]. The same design logic was also effective in Fe/FeO_x/Al_2O_3−MgO, which achieved a C_{2+} hydrocarbon selectivity of 52.9% under ultraviolet–visible illumination. There, FeO_x suppressed further hydrogenation of CH_2* and CH_3* intermediates on Fe^0 sites, thus increasing the surface concentration of CH_x* species and facilitating C−C coupling [129].

Overall, charge-polarized dual-active sites create asymmetric charge environments for C_1 intermediates through their distinct valence states and electron densities, thereby promoting C−C coupling while suppressing excessive hydrogenation. In particular, electron-deficient metal species can act as electron acceptors to inhibit further hydrogenation of C_1 intermediates and thus favor C−C bond formation [169].

4.2.3 CH_3OH Coupling*

As direct studies on CH_3OH*-mediated C−C coupling in photothermal CO_2 hydrogenation remain unavailable,

© The authors
https://doi.org/10.1007/s40820-026-02351-0

insights from thermal catalysis provide a useful basis for catalyst design. Current efforts have centered on tandem systems that integrate metal oxides with zeolites, where the former are responsible for generating oxygenated intermediates and the latter provide confined acidic environments for subsequent C−C bond formation. Within such systems, the efficiency of multicarbon product formation is governed largely by pore architecture and acidity of the zeolite, as well as spatial intimacy between the two catalytic components.

(1) Regulation of pore size structure

Tuning the pore architecture of zeolite catalysts significantly influences the C−C coupling process, primarily through confinement effects. Properly sized microporous environments can spatially restrict the diffusion of CO_2, H_2, and key hydrogenated intermediates (e.g., CO*, HCO*, CH_x*), thereby enriching their local concentration and enhancing the probability of C−C bond formation [179]. In this regard, zeolites with 10-membered rings provide a more suitable confinement environment for the oligomerization of hydrocarbon pool species, whereas 8- or 12-membered-ring frameworks tend to impose either overly strong or insufficient confinement, making them less favorable for C−C bond formation [180]. Structural variations introduced during zeolite synthesis can further affect product selectivity. In a Cu-modified Fe_2O_3/HZSM-5 system, HZSM-5 prepared by a phase transfer method showed improved performance for the selective formation of benzene, toluene, and xylene, which was associated with the abundant mesopores (5−12 nm) that facilitated molecular diffusion and intermediate stabilization (Fig. 17a) [181].

(2) Adjustment of zeolite acidity

Brønsted acid sites within zeolites play a critical role in promoting the formation of C_{2+} products, as they catalyze essential carbon chain growth reactions, including alcohol dehydration, olefin oligomerization/polymerization, and alkylation with aromatics. This acidity can be finely regulated through the Si/Al ratio, which determines both the density and strength of Brønsted acid sites [182, 183]. Higher acid-site density generally favors the formation of aromatics and heavier olefins, whereas weaker or less abundant acid sites are more conducive to lighter olefins (Fig. 17b). Such differences are attributed to the higher catalytic activity of strongly acidic zeolites in facilitating olefin-to-aromatic conversions, which simultaneously generated reactive hydrogen species via olefin dehydro-aromatization. These hydrogen species can be consumed in CO_2 or CO reduction, accelerating the RWGS and Fischer–Tropsch synthesis processes. However, overly strong acidity may lead to excessive cracking, thereby reducing the selectivity toward C_{5+} products [184].

(3) Optimization of proximity effect

The efficiency of C_{2+} hydrocarbon formation in oxide–zeolite tandem systems is governed to a large extent by how rapidly oxygenated intermediates, such as CH_3OH*, can migrate from metal–oxide sites to Brønsted acid sites in the zeolite. Therefore, the proximity effect between the two components is a decisive factor influencing both activity and selectivity [185].

In the $ZnZrO_x$/SSZ-13 system, a separation distance of 20−50 nanometers was found to be most favorable for light-olefin production (Fig. 17c). Although shorter distances may increase local intermediate concentrations, they also risk pore blockage, reduced surface area, and restricted diffusion, ultimately impairing hydrocarbon production. By contrast, excessively large separations hinder intermediate transfer and lower overall conversion efficiency. A well-balanced proximity can enhance proton mobility and intermediate diffusion, increasing local concentration of carbon species and facilitating subsequent chain growth. Moreover, compared to stepwise operation, this tandem route via CH_3OH* intermediate is both thermodynamically and kinetically advantageous [143].

Compared with CO* or CH_x* coupling routes, systems involving CH_3OH* intermediates require more complex catalyst design, yet they offer a distinct advantage in breaking away from the conventional ASF distribution, allowing for higher selectivity toward C_{2+} products. Although CH_3OH*-mediated C−C coupling has not yet been demonstrated in photothermal CO_2 hydrogenation, the incorporation of zeolites into photothermal catalytic systems has already begun to attract attention [186]. Hence, integrating oxide–zeolite tandem architectures into photothermal CO_2 hydrogenation may provide a promising route toward higher activity and improved C_{2+} selectivity.

Overall, as compared in Table 6, these strategies indicate that efficient C_{2+} synthesis requires the cooperative regulation of upstream CO_2 activation and downstream C–C

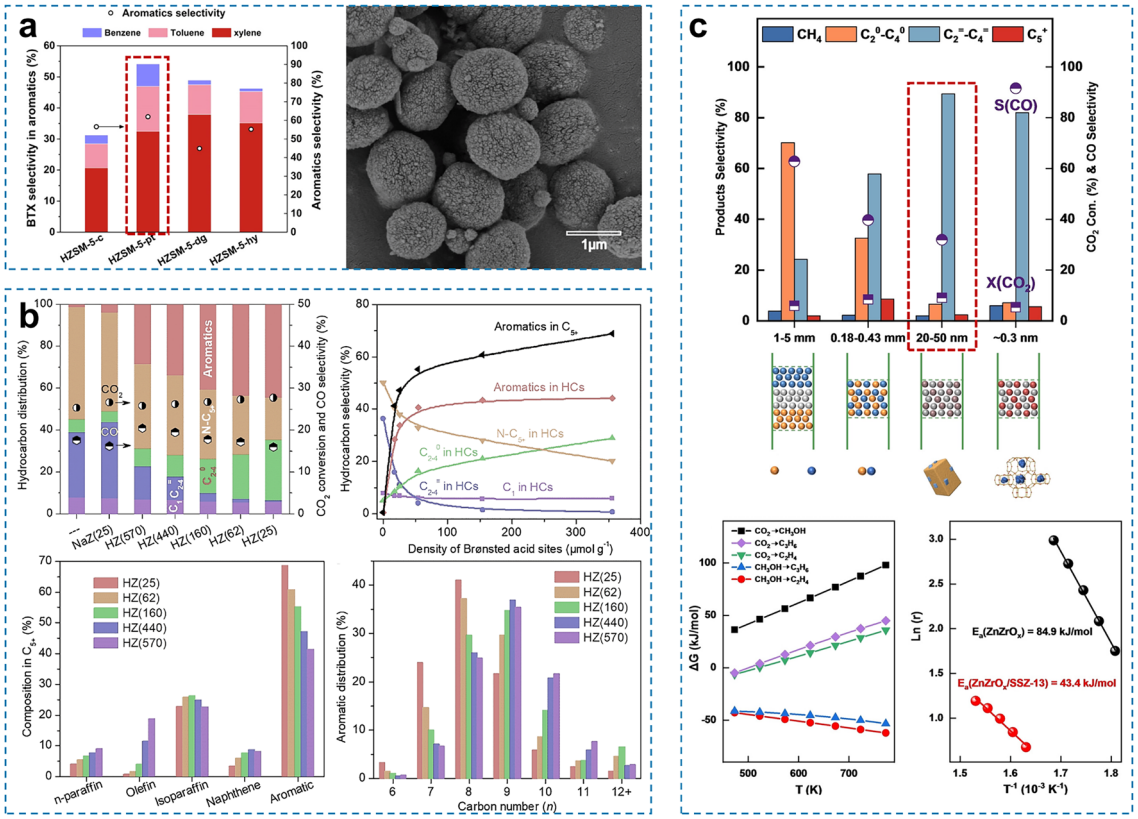


Fig. 17 Surface optimization strategies for promoting C−C coupling of C_1 intermediates via CH_3OH* coupling. **a** Pore size structure regulation in HZSM-5. Reproduced with permission from Ref. [181], Copyright 2020 American Chemical Society. **b** Zeolite acidity adjustment in HZ. Reproduced with permission from Ref. [184], Copyright 2021 Elsevier. **c** Proximity effect optimization in $ZnZrO_x$/SSZ-13. Reproduced with permission from Ref. [143], Copyright 2024 John Wiley and Sons

coupling. Future catalyst design should therefore integrate photothermal field regulation, active-site construction, intermediate stabilization, and coupling-site engineering rather than optimizing a single material feature alone.

5 Scale Demonstration of Photothermal CO_2 Hydrogenation

The long-term appeal of photothermal CO_2 hydrogenation to C_{2+} products lies in its potential to enable efficient and value-added CO_2 conversion using solar energy as the sole energy input, while avoiding secondary pollution. Recent studies have increasingly moved beyond laboratory-scale evaluation toward demonstrations under direct sunlight, aiming to assess the scalability of photothermal CO_2 hydrogenation. However, most scale demonstrations reported so far remain centered on CO, CH_4, or methanol. These C_1-oriented scale systems are still important as they provide key intermediates and engineering experience for downstream C–C coupling. Thus, this section highlights representative scale demonstrations as useful references for the future scale-up of photothermal CO_2-to-C_{2+} conversion.

5.1 Scale Demonstrations of Catalytic CO_2 Hydrogenation Enabled by Optical Concentration-Enhanced Solar Energy Harvesting

When solar energy serves as the sole energy input, the local temperature generated on photothermal catalysts under natural sunlight is often insufficient to reach the optimal range required for efficient CO_2 hydrogenation, even for materials with high photothermal conversion efficiency. To overcome this limitation, solar concentrators have been introduced to intensify incident sunlight, thereby elevating catalyst surface temperatures to levels suitable for efficient reaction performance [187, 188].

© The authors
https://doi.org/10.1007/s40820-026-02351-0

Table 6 Comparison of catalyst modification strategies for photothermal CO_2 hydrogenation toward C_{2+} products

Strategy	Advantages	Challenges	Application scope
Control of morphology	Most useful when light absorption or heat delivery limits the rate Provides an engineering basis for flow and outdoor reactors	Rate gains may be purely thermal without matched temperature controls Hot spots can induce sintering, coking, and spatial selectivity gradients	RWGS/CO generation, methanation, and C_1 precursor formation Requires additional C−C coupling sites for selective C_{2+} synthesis
Construction of basic sites	Builds reactive C_1 precursor pools using simple promoter chemistry Compatible with many metal and oxide catalysts	Strong basicity can trap carbonate/formate species Provides little intrinsic C−C coupling ability	CO and methanol precursor formation Auxiliary module for C_{2+} catalysts when paired with coupling sites
Creation of surface defects	Links light absorption, carrier trapping, and oxide surface chemistry Can tune COOH*/HCOO* pathway preference	Defects and SFLPs are dynamic under CO_2/H_2/light/heat Assignments often need operando, isotope, or regeneration evidence	Oxide-mediated CO and methanol routes C_{2+} use requires stable, regenerable defects
Introduction of metal active sites	Strong gas activation at low temperature or under light Useful models for separating thermal, plasmonic, and carrier effects	High hydrogenation activity can favor CH_4 over C_{2+} products Cost, sintering, and hot-carrier ambiguity limit generality	Methanation, methanol formation, and upstream C_1 activation Needs coupling control sites for C_{2+} selectivity
Alloy-mediated coupling-site engineering	Directly links composition to C−C coupling probability Can balance CO_2 activation, H supply, and chain growth	Active ensembles are phase- and composition-sensitive Segregation, oxidation, or excess H coverage can redirect selectivity	CO*- or CH_x*-mediated ethanol, acetate, and C_2−C_4 hydrocarbons Requires operando identification of the active alloy/interface state
Interface and bifunctional engineering	Balances C_1 generation with suppression of overhydrogenation Particularly valuable for olefin-oriented systems	Performance is highly proximity-dependent Interface reconstruction and multiple active phases complicate mechanism assignment	CO*−HCO*/CO*−COH* coupling and CH_x*-mediated olefin routes Systems needing balanced activation, spillover, and hydrogenation control
Charge-polarized dual-site engineering	Targets the intrinsic C−C coupling bottleneck directly Can bias selectivity toward light olefins, ethanol, or acetate	Precise, stable paired-site construction remains difficult Similar trends may also arise from alloys, interfaces, or thermal coverage effects	High-selectivity C_2 design via CO*−CO* or CH_x*−CH_x* coupling Best used with operando spectroscopy and DFT verification
Tandem and confinement engineering	Bypasses ASF-type limitations Offers a clear route to olefin and aromatic selectivity	Direct photothermal C_{2+} evidence remains limited Coking, diffusion limits, and heat transfer mismatch can erode performance	CH_3OH*/oxygenate-mediated olefins, aromatics, and liquid fuels Hybrid thermal photothermal tandem systems

Among the available designs, parabolic trough concentrators enhance local irradiance by focusing sunlight onto a linear focal region, thereby improving photothermal reaction efficiency [189]. Under such concentrated irradiation, light intensity can reach 300 mW cm^{-2}, giving a surface temperature of about 56 °C on γ-Al_2O_3|TiO_2|CotpyP (Fig. 18a). To prevent catalyst sintering and coking under intensified heating, water-jacketed cooling systems can be incorporated into reactor designs to maintain operating conditions below deactivation thresholds [190]. Additionally, panel-type photoreactors integrating V-shaped concentrators with tubular reaction cavities have also been developed as alternative solar concentration configurations. This configuration, composed of hundreds of parallel reaction channels, enabled a more uniform photon flux distribution within the active zone, improved quantum efficiency, and showed promise for decentralized rooftop-scale applications (Fig. 18b) [191].

Unlike traditional convex lenses, Fresnel lenses retain the refractive geometry while removing internal bulk material, thereby reducing thickness and shortening focal length (Fig. 18c) [192]. The reduced thickness minimizes internal light absorption, allowing for cost-effective production using materials such as plastic [81].

Applied to a Ru/Mo_2TiC_2 catalyst under outdoor conditions, the Fresnel lens increased the incident intensity to 3.7 W cm^{-2} and raised catalyst temperature to ~360 °C within 30 s, resulting in an outdoor CO production rate of 3.9 mol g_{Ru}^{-1} h^{-1} with 90% selectivity (Fig. 18d) [193]. Building on this concept, a three-stage flow reactor was further developed to improve overall CO_2 conversion under outdoor operation. As the reactant stream passed sequentially through three catalytic zones containing Ru-Al_2O_{3-x}-L microchannel catalysts, the product yield increased progressively, while the CO_2 concentration decreased, ultimately giving a CO_2

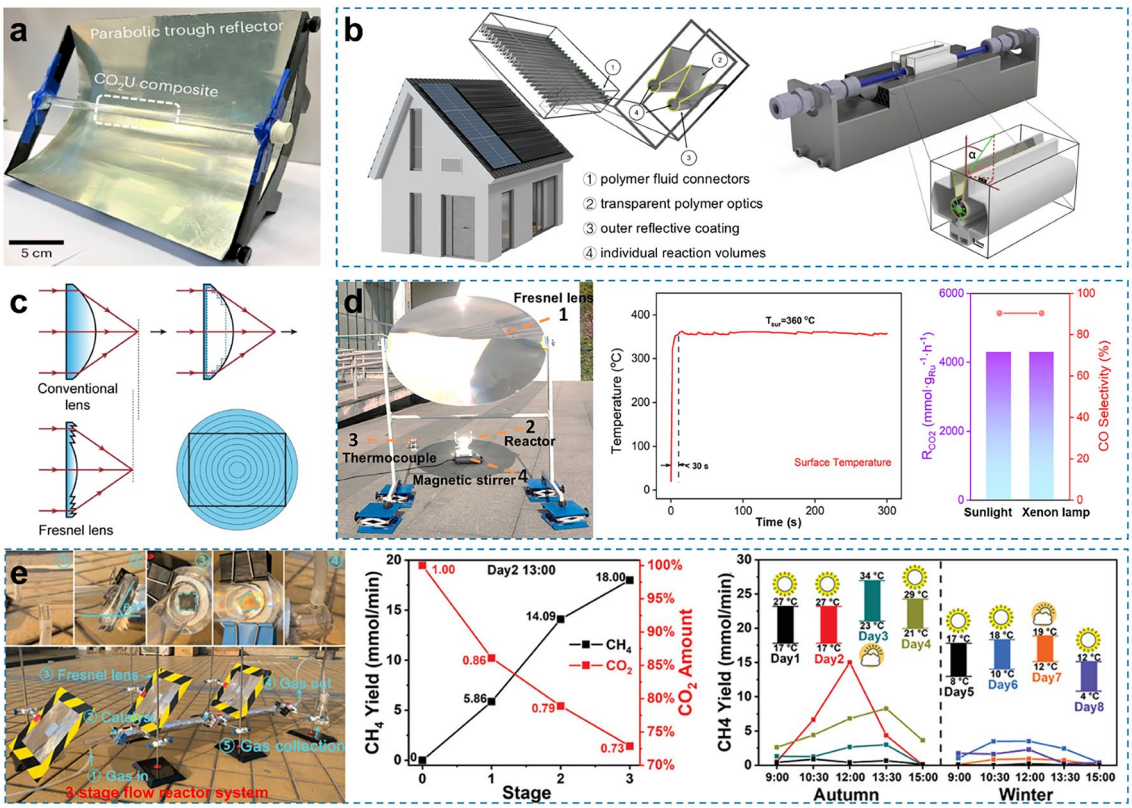


Fig. 18 Scale demonstrations of photothermal CO_2 hydrogenation enabled by optical concentration-enhanced solar energy harvesting. **a** Parabolic trough concentrator. Reproduced with permission from Ref. [190], Copyright 2025 Springer Nature. **b** V-shaped solar concentrator for solar-driven synthesis. Reproduced with permission from Ref. [191], Copyright 2023 Elsevier. **c** Comparison between conventional lens and Fresnel lens. Reproduced with permission from Ref. [81], Copyright 2023 John Wiley and Sons. **d** Fresnel lens-based concentrator on Ru/Mo_2TiC_2. Reproduced with permission from Ref. [193], Copyright 2022 American Chemical Society. **e** Three-stage flow Fresnel lens-based concentrator on Ru-Al_2O_{3-x}-L. Reproduced with permission from Ref. [194], Copyright 2022 John Wiley and Sons

© The authors
https://doi.org/10.1007/s40820-026-02351-0

conversion of 27.10% and a CH_4 production rate of 18.00 mmol min^{-1} (Fig. 18e). However, performance remains closely tied to solar availability: the highest product yields were observed at around 13:30 in autumn and 12:00 in winter [194], and product formation rates under clear skies were nearly twice those measured under cloudy conditions [195].

5.2 Scale Demonstrations of Catalytic CO_2 Hydrogenation Enabled by Solar-to-Thermal Energy Conversion

An alternative route for scaling up solar-driven photothermal CO_2 hydrogenation relies on solar-to-thermal conversion devices that harvest sunlight, store it as heat, and deliver the accumulated thermal energy to the catalytic reactor. This solar-to-thermal conversion pathway offers a practical means to stabilize reaction conditions while exploiting renewable solar input.

Since 2022, a series of scale demonstrations based on solar-to-thermal energy conversion have been reported. Early work employed a Bi_2Te_3/Cu-based device for photothermal methanol reforming to hydrogen, in which Bi_2Te_3 served as an efficient solar absorber capable of converting up to 99% of incident light into heat, while the highly conductive Cu layer suppressed infrared radiative loss. As a result, the device reached an internal temperature of 307 °C under one-sun illumination [196]. In 2023, TiC/Cu-based devices were employed in outdoor demonstrations of photothermal CO_2 hydrogenation, with TiC assumed to function analogously to Bi_2Te_3 (Fig. 19a). Under one-sun illumination, the enclosed catalyst could reach surface temperatures of 350–380 °C, providing sufficient thermal energy to drive the CO_2 hydrogenation reaction solely via solar-to-thermal conversion.

This TiC/Cu platform was subsequently extended to progressively larger outdoor demonstrations. In a small-scale system using $Cu_2Zn_1Al_{0.5}Ce_5Zr_{0.5}O_x$ catalyst, a parabolic reflector was incorporated to concentrate diffuse sunlight and maintain elevated operating temperatures throughout the day (Fig. 19b) [68]. The same strategy was then applied to a 20 m^2 illuminated area with AgK/Fe_3O_4 as the catalyst, where substantial CO production was sustained even at ambient temperatures below 10 °C, demonstrating reliable operation under relatively harsh outdoor conditions (Fig. 19c) [64]. Further scale-up to a 103 m^2 field was achieved in 2024, together with photovoltaic water electrolysis as the hydrogen source, thereby establishing an artificial photosynthetic system for outdoor syngas production. This integrated system produced about 21.14 m^3 of green syngas with an H_2/CO ratio close to 1, demonstrating promising efficiency, scalability, and economic potential for outdoor application (Fig. 19d) [197]. More recently, this solar-to-thermal strategy was extended to a self-sustained continuous demonstration of photothermal CO_2 methanation. Owing to the exothermic nature of CO_2 methanation, the reaction could continue even in the dark once sufficient heat had been accumulated, and a water-cooling system was introduced to maintain the catalyst surface at 300 °C and avoid thermal deactivation. This design enabled continuous day-and-night operation while simultaneously generating usable hot water, further broadening the practical prospects of solar-driven photothermal CO_2 hydrogenation (Fig. 19e) [198].

5.3 Scale Demonstration of Catalytic CO_2 Hydrogenation Enabled by Solar-to-Chemical Energy Conversion

Scale demonstrations of thermal catalytic CO_2 hydrogenation based on solar-to-chemical energy conversion represent an emerging paradigm for sustainable fuel synthesis. In this approach, solar energy is initially stored in molecular carriers such as H_2, which subsequently serve as energy carriers to drive catalytic CO_2 conversion. This pathway not only facilitates continuous operation under fluctuating solar input but also addresses the challenge of securing a green hydrogen supply.

Kazunari Domen et al. coupled photocatalytic water splitting with thermocatalytic CO_2 methanation in an artificial photosynthesis platform (Fig. 20a) [199]. Using a 100 m^2 panel-type reactor array loaded with $SrTiO_3$:Al (Fig. 20b), the photocatalytic unit generated 1770 L of oxyhydrogen in a single day under strong summer sunlight, from which 96.5% pure H_2 was obtained after gas separation and subsequently used for CO_2 methanation. During a three-day experiment, the integrated system yielded a total of 43.9 L of crude methane with a purity of 61.2% [200]. In addition, the "kiloton-scale liquid solar fuel synthesis demonstration project" led by Can Li integrated photovoltaic power generation, water electrolysis, and CO_2 hydrogenation for methanol synthesis. Solar electricity drove large-scale electrolyzers to produce H_2 at rates above 1000 m^3 h^{-1}, which was then converted with

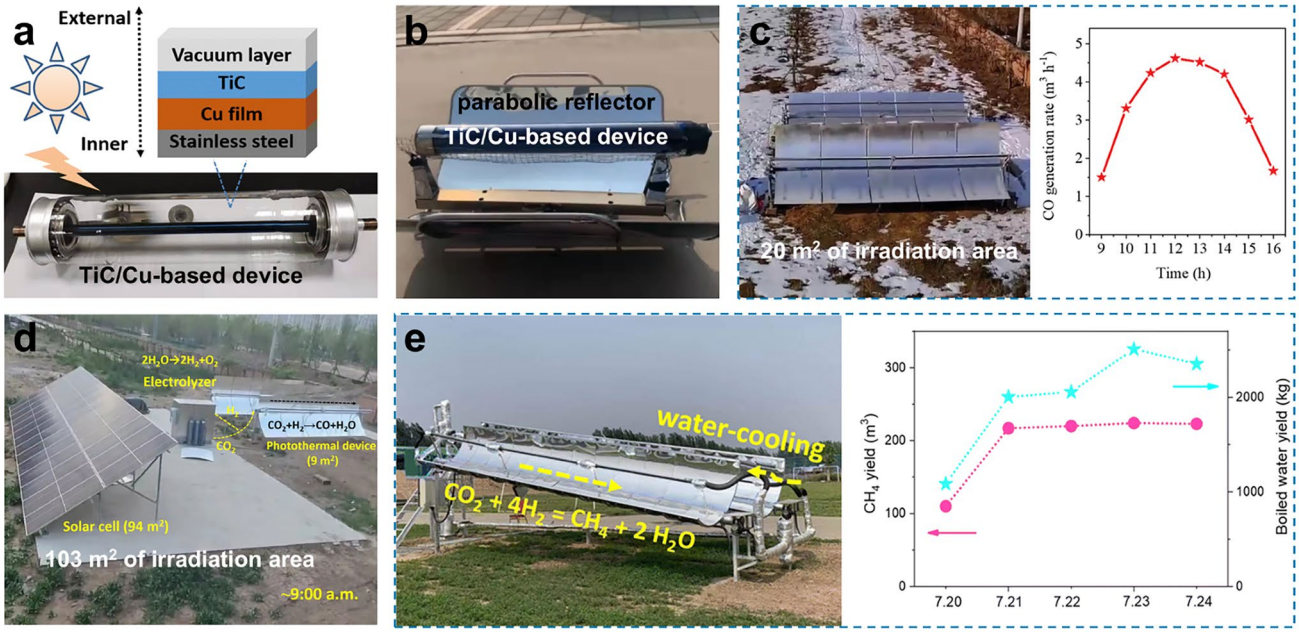


Fig. 19 Scale demonstrations of photothermal CO_2 hydrogenation enabled by solar-to-thermal energy conversion. **a** TiC/Cu-based solar-to-thermal devices. Reproduced with permission from Ref. [198], Copyright 2025 The Royal Society of Chemistry. **b** TiC/Cu-based solar-to-thermal devices on $Cu_2Zn_1Al_{0.5}Ce_5Zr_{0.5}O_x$. Reproduced with permission from Ref. [68], Copyright 2023 Springer Nature. **c** 20 m^2 TiC/Cu-based solar-to-thermal devices on AgK/Fe_3O_4. Reproduced with permission from Ref. [64], Copyright 2024 John Wiley and Sons. **d** 103 m^2 TiC/Cu-based solar-to-thermal devices on $Ni_1Ag_{0.02}O_1$. Reproduced with permission from Ref. [197], Copyright 2024 The Authors. **e** Self-sustained TiC/Cu-based solar-to-thermal devices on $Ni_1Ce_1O_3$. Reproduced with permission from Ref. [198], Copyright 2025 The Royal Society of Chemistry

CO_2 over $ZnZrO_x$ solid solution catalysts in an adiabatic fixed-bed reactor. Commissioned in January 2020, the system reached a methanol purity of 99.5 mol% within 3 h.

5.4 Practical Feasibility of Scaled Photothermal CO_2 Hydrogenation

Although recent scale demonstrations have shown that photothermal CO_2 hydrogenation can operate under real sunlight, practical deployment requires further evaluation beyond reactor size, product output, or short-term activity. Two issues are particularly important for scaled systems: catalyst durability under long-term photothermal operation and techno-economic feasibility at the process level. The former determines whether activity and selectivity can be maintained under fluctuating light and temperature fields, whereas the latter determines whether solar-driven CO_2 hydrogenation can compete with established thermocatalytic or fossil-based production routes.

5.4.1 Catalyst Feasibility

Catalyst durability is a prerequisite for the practical deployment of photothermal CO_2 hydrogenation. Compared with conventional thermal catalysis, photothermal catalysis operates under spatially non-uniform light and temperature fields, where localized hot spots and repeated light/dark cycling may accelerate structural evolution of catalysts [130]. This issue becomes more critical for C_{2+} product synthesis, because C–C coupling and chain growth reactions involve multiple surface intermediates and may promote the accumulation of heavier hydrocarbons or carbonaceous species [26, 182]. Therefore, long-term stability should be evaluated not only by maintaining product yield, but also by tracking selectivity evolution, active-site structure, surface temperature distribution, and carbon balance during operation.

The deactivation of photothermal CO_2 hydrogenation catalysts generally originates from several pathways. First, metal nanoparticles may undergo sintering or aggregation under localized high-temperature conditions, leading to the

© The authors
https://doi.org/10.1007/s40820-026-02351-0

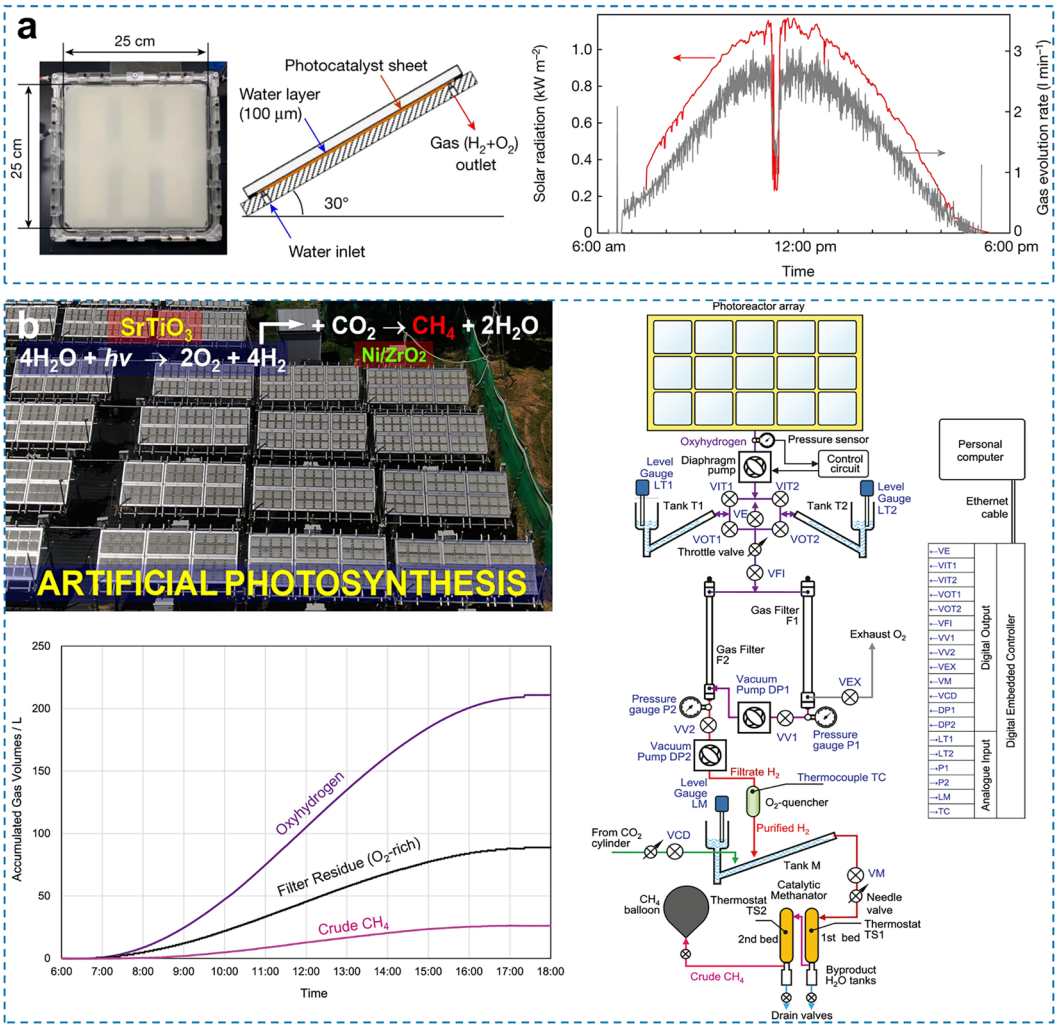


Fig. 20 Scale demonstrations of photothermal CO_2 hydrogenation enabled by solar-to-chemical energy conversion. **a** Panel reactor for solar-driven water splitting. Reproduced with permission from Ref. [199], Copyright 2021 Springer Nature. **b** Artificial photosynthesis system via solar-to-chemical energy conversion. Reproduced with permission from Ref. [200], Copyright 2023 American Chemical Society

loss of exposed active sites and weakened metal–support interfaces. For example, post-reaction characterization of plasmonic Pt/TiN showed that Pt species transformed from single atoms/clusters into 1–2 nm nanoparticles under reaction conditions, and this sintering was identified as the reason for the gradual activity decline [168]. Second, active metal or oxide sites may experience oxidation, reduction, or structural reconstruction during redox operation, thereby changing the adsorption and activation behavior of CO_2 and H_2. For instance, TiO_x overlayers formed on Ni/TiO_2 after high-temperature reduction were removed under CO_2 hydrogenation conditions, demonstrating that metal–oxide interfacial structures can dynamically reconstruct during reaction [201]. Third, oxygen vacancies and other surface defects may be gradually consumed or passivated by oxygen-containing intermediates, resulting in decreased CO_2 activation ability. This possibility is supported by theoretical and experimental studies showing that CO_2 dissociation at oxygen vacancy sites can insert oxygen into the vacancy and reoxidize the reduced surface. For example, on defective TiO_2, CO_2 dissociation at oxygen vacancies leads to CO formation while the reduced surface becomes oxidized, indicating that oxygen vacancies can be consumed during CO_2 activation [202]. Therefore, when oxygen vacancy regeneration is insufficient, defect-mediated CO_2 activation may gradually weaken during long-term operation. In addition, photothermal hot spots

may induce support phase transformation, pore collapse, or interfacial reconstruction, further reducing catalytic stability. This concern is consistent with general thermal deactivation mechanisms, where high-temperature operation can cause active-phase crystallite growth, loss of support surface area through pore collapse, and transformation of catalytic phases into less active phases.

Improving the durability of photothermal CO_2 hydrogenation catalysts requires coordinated optimization of catalyst structure, active-site regeneration, and reactor-level heat management. Stable catalyst architectures, such as confined metal nanoparticles, alloy structures, strongly coupled metal–support interfaces, and defect-anchored active sites, can suppress structural degradation under localized photothermal heating [20]. Meanwhile, reducible supports, hydrogen spillover pathways, and redox-cycling treatments can help maintain defect-mediated CO_2 activation [203]. For catalysts affected by strongly adsorbed intermediates or carbon deposits, controlled regeneration treatments are needed to restore active sites [204]. In addition, uniform irradiation, efficient heat dissipation, and improved mass transport are essential for reducing hot-spot-induced degradation. These strategies should be combined with long-term stability tests and post-reaction characterization to establish reliable durability criteria for practical photothermal CO_2 hydrogenation.

5.4.2 Economic Feasibility

Beyond catalyst durability, the practical deployment of scaled photothermal CO_2 hydrogenation also depends on whether the overall process can become economically competitive. Economic feasibility should therefore be evaluated from a system-level perspective rather than solely from catalytic activity or reactor productivity. Key cost factors include renewable H_2 supply, CO_2 capture and purification, catalyst lifetime, reactor capital investment. These factors are especially important for C_{2+} synthesis, which typically involves higher H_2 input, more complex reaction networks, exhibits lower single-pass selectivity, and imposes greater downstream separation costs than C_1 production. Recent techno-economic analysis estimated the levelized costs of photothermal CO_2 conversion to CO, CH_4, CH_3OH, and C_{2+} products to be 723.59, 617.37, 716.91, and 989.07 USD t^{-1}, respectively [205]. Since these values remain higher than the corresponding market prices, current photothermal CO_2 conversion technologies still lack broad cost competitiveness.

Among the system-level cost contributors, green H_2 plays a central role in determining the economics of CO_2-derived fuels and chemicals. It has been reported that renewable methanol production using electrolytic H_2 and flue-gas-captured CO_2 has a levelized cost of approximately 960 € t^{-1}, more than twice the international methanol market price of about 450 € t^{-1}. The cost penalty mainly arises from electrolyzer investment and renewable electricity demand [206]. For olefin production through CO_2 hydrogenation using green H_2 and CO_2 captured by direct air capture, the minimum selling price of olefins was estimated to be approximately £3.67 kg^{-1}, with electricity cost remaining the dominant cost driver [207]. From the perspective of H_2 consumption per unit product, methanol production requires approximately 0.188 t H_2 per ton of CH_3OH, whereas ethylene production requires approximately 0.429 t H_2 per ton of C_2H_4. Therefore, as the target products extend from C_1 compounds to C_{2+} products, H_2 demand and the associated cost pressure will further increase. Reducing the cost of green H_2, particularly through low-cost renewable electricity, improved electrolyzer utilization, and optimized H_2 storage and system integration, is therefore essential for the economic viability of photothermal CO_2 hydrogenation.

The CO_2 source represents another critical cost variable. Most laboratory and pilot-scale photothermal CO_2 hydrogenation studies use high-purity CO_2, whereas industrial deployment would require CO_2 from point-source capture, biogenic sources, or direct air capture. Among these options, point-source CO_2 is more attractive because capture cost decreases significantly as CO_2 concentration increases. According to the International Energy Agency, CO_2 capture costs are about 15–25 USD t^{-1} for relatively pure or highly concentrated industrial CO_2 streams, such as those from ethanol production and natural gas processing, but increase to 40–120 USD t^{-1} for more dilute sources, including cement production and coal-fired power generation. By contrast, direct air capture still suffers from substantially higher energy demand and cost because the CO_2 concentration in air is much lower than that in flue gas or industrial process streams. Therefore, coupling photothermal CO_2 hydrogenation with highly concentrated or low-cost point-source CO_2 is likely to be more economically feasible in the near term. Although direct-air-capture-coupled systems are

© The authors https://doi.org/10.1007/s40820-026-02351-0

potentially attractive for long-term carbon-neutral or carbon-negative fuel synthesis, their feasibility will depend on substantial reductions in capture cost, regeneration energy demand, and the cost of low-carbon heat or electricity.

From the perspective of scale-up routes, as summarized in Table 7, different pathways exhibit distinct advantages and limitations. Optical concentration-enhanced systems directly enhance photon flux and catalyst temperature, but their productivity is highly sensitive to direct solar irradiance, weather conditions, optical alignment, and tracking efficiency. Moreover, highly concentrated light may increase local product yield but can also waste photons when light penetration, catalyst utilization, and heat distribution are not optimized [205]. Solar-to-thermal systems can to some degree mitigate solar irradiation fluctuations by heat accumulation and are therefore attractive for exothermic reactions such as CO_2 methanation, as evidenced by recent day-and-night photothermal methanation. However, this approach requires additional costs for solar absorbers, insulation materials, heat transfer modules, and cooling systems [198]. By contrast, solar-to-chemical integrated systems couple photovoltaic water electrolysis or photocatalytic water splitting with CO_2 hydrogenation, which can partially decouple solar energy harvesting from catalytic conversion and thereby improve operational flexibility. Nevertheless, the economic feasibility of such systems remains highly dependent on the capital cost of water-splitting devices, H_2 purification and compression costs, and the overall system capacity factor.

Table 7 Scale-up demonstrations of solar-driven CO_2 conversion routes

Route	Catalytic System	Product	Scale	Rate	Stability	Advantages	Disadvantages	Ref.
Optical concentration-enhanced solar energy harvesting	Ni/C-In_2O_3	CO	~7 cm^2	20.96 mmol g_{cat}^{-1} h^{-1}	2 d	Direct photon flux enhancement Higher catalyst temperature High local productivity Compact optical reactors	Direct irradiance sensitivity Weather dependence Optical alignment demand Limited light penetration Uneven heat distribution	[188]
	Ru/Mo_2TiC_2	CO	4.91 cm^2	3.9 mol g_{Ru}^{-1} h^{-1}	10 h			[193]
	Ru-Al_2O_3−x-L	CH_4	4 cm^2	18.00 mmol min^{-1}	8 d			[194]
	Ru-TiO_x	CH_4	4 cm^2	~0.95−1.12 mmol g_{cat}^{-1} h^{-1}	7 d			[195]
	Ru_1/CeO_2-AS	CH_4	~0.785 cm^2	32.36 mol g_{Ru}^{-1} h^{-1}	7 d			[208]
	Ru_1/CeO_2	CO	~0.785 cm^2	42.53 mol g_{Ru}^{-1} h^{-1}	7 d			[208]
	$CoFe_2O_4$ /$(Fe_{1-x}Co_x)_5C_2$	C_2-C_4 olefins	706.5 cm^2	66.1 L m^{-2} day^{-1}	1 d			[130]
Solar-to-thermal energy conversion	5%AgK/Fe_3O_4	CO	20 m^2	1925 mmol g^{-1} h^{-1}	1 d	Heat accumulation buffering Lower fluctuation sensitivity Suited to exothermic reactions for day-and-night operation	Insulation material cost Heat transfer modules Cooling system demand Thermal management complexity	[64]
	$Cu_2Zn_1Al_{0.5}Ce_5Zr_{0.5}O_x$	CO	0.0396 m^2	248.5 mmol g^{-1} h^{-1}	7 d			[68]
	$Ni_1Ag_{0.02}O_1$	CO	9 m^2	1434 mmol g^{-1} h^{-1}	4 d			[197]
	$Ni_1Ce_1O_3$	CH_4	N.R.	179.6 m^3 d^{-1}	5 d			[198]
Solar-to-chemical energy conversion	Ni/ZrO_2	CH_4	12.19 m^2	26.9 L d^{-1}	3 d	PV–electrolysis coupling Photocatalytic H_2 coupling Harvesting/conversion decoupling Improved operational flexibility	Water-splitting efficiency H_2 purification cost Capacity factor dependence Full-system integration cost	[200]

In summary, photothermal CO_2 hydrogenation offers an attractive strategy for reducing external thermal input by integrating solar energy harvesting and catalytic conversion within a single system. However, its economic advantage over established thermocatalytic processes and fossil-derived chemical production routes remains to be fully demonstrated. Future scale demonstrations should therefore move beyond proof-of-concept validation and provide standardized techno-economic indicators. In the case of C_{2+} products, additional benchmarks, such as C_{2+} carbon selectivity, olefin/paraffin ratio, single-pass carbon efficiency, and separation cost for multi-product streams, should be carefully reported. Establishing such standardized techno-economic benchmarks will be essential for determining whether photothermal CO_2 hydrogenation can progress from scalable demonstration to economically viable industrial deployment.

6 Conclusions and Perspectives

Photothermal CO_2 hydrogenation to C_{2+} products represents a promising green chemistry approach, offering not only a viable pathway for CO_2 emission reduction but also significant industrial potential for the synthesis of high-value chemicals. Nevertheless, achieving efficient and selective formation of C_{2+} products remains challenging due to limitations in reactant mass transfer and difficulties in C−C bond formation. This review systematically summarizes recent advances in photothermal CO_2 hydrogenation to C_{2+} products. The fundamental principles of photothermal catalysis are first discussed from the perspectives of photo-induced, thermal, and synergistic effects. Subsequently, the activation of CO_2 to C_1 intermediates and the C−C coupling pathways leading to C_{2+} products are analyzed. Based on these mechanistic insights, we outline a series of catalyst design and modification strategies. To enhance CO_2 activation toward C_1 intermediates, we review catalyst engineering approaches that improve photothermal conversion efficiency and promote reactant activation, grounded in core principles of photothermal catalysis. For the C−C coupling of C_1 intermediates into C_{2+} products, multiple catalyst design strategies are summarized according to different coupling routes. Additionally, recent progress in scaled-up demonstrations is highlighted to support the development of practical, scalable CO_2 hydrogenation technologies. Overall, this review offers theoretical guidance for the rational design of photothermal catalysts toward efficient and selective CO_2 conversion to multicarbon products.

Despite notable progress, several critical challenges remain, which should be addressed in future research:

(1) At the material level, future progress requires a transition from empirical catalyst optimization to data-driven catalyst construction. Current trial-and-error strategies are inefficient for discovering C_{2+}-selective photothermal CO_2 hydrogenation catalysts as relevant compositional, structural, and interfacial space is extremely broad. Although machine learning has been increasingly used in CO_2 catalytic conversion, its application to photothermal CO_2 hydrogenation, especially C_{2+} formation, remains limited. Future studies should establish standardized datasets that integrate catalyst structure, light absorption, and product performance, enabling predictive models for activity and selectivity. Active learning can then identify high-value experiments and update models with informative feedback, while inverse design can generate catalyst candidates that meet predefined targets. In the long term, closed-loop autonomous platforms combining prediction, synthesis, testing, and feedback may accelerate the discovery of efficient and stable C_{2+}-selective photothermal catalysts.

(2) At the reaction level, future research should shift from activity-oriented CO_2 conversion to selectivity-oriented C_{2+} synthesis. Current photothermal CO_2 hydrogenation systems mainly produce C_1 products, whereas C_{2+} olefin formation is limited by the sluggish kinetics of C–C bond formation and the competing over-hydrogenation reaction. As discussed in this review, C–C coupling can proceed through CO*-mediated, CH_x*-mediated, and CH_3OH*-mediated pathways. Among them, the CH_3OH*-mediated route is particularly attractive because it may alleviate the restriction of ASF distribution and improve C_{2+} selectivity through tandem transformation. However, zeolite-based systems have rarely been applied in photothermal catalysis due to their insufficient photothermal response and inefficient charge transport. Future designs should therefore enhance the light-harvesting and charge transfer capabilities of zeolite-based hybrid catalysts. If these limitations can be effectively addressed, a feasible short-term benchmark would be to achieve C_{2+} product selectivity above 70%. In the long term, these improved reaction modules are expected to support stable, pathway-directed C_{2+} synthesis under continuous photothermal operation.

© The authors
https://doi.org/10.1007/s40820-026-02351-0

(3) At the system level, future research should bridge the gap between short-term photothermal demonstrations and reliable outdoor solar fuel operation. Current photothermal CO_2 hydrogenation systems can operate under natural sunlight, but their stability remains limited by fluctuating solar irradiation, which induces variations in reactor temperature, reaction rate, H_2 demand, and product distribution. Future systems should therefore integrate solar energy collection, thermal buffering, green H_2 supply, CO_2 conversion, and product separation into an adaptive platform. In such systems, H_2 supply should be dynamically matched with real-time temperature and catalytic consumption to improve resource utilization. Machine learning-driven multi-objective optimization can further identify stable operating windows by balancing C_{2+} productivity, product selectivity, solar-to-chemical efficiency, H_2 utilization, and operational stability. Once such optimized operating windows are established, the next practical milestone should be stable outdoor operation over hundreds of hours with quantified solar-to-chemical efficiency.

(4) At the industrial level, the key challenge is to translate scalable photothermal CO_2 hydrogenation from demonstration systems into economically meaningful processes. Although recent scale-up studies suggest practical potential, larger reactor size or longer operation time alone cannot establish industrial feasibility. The total process cost is strongly affected by green H_2 supply, CO_2 capture and purification, reactor construction, catalyst durability, and downstream separation. This challenge is more pronounced for C_{2+} products, where higher H_2 demand and multi-product separation increase both energy input and operating cost. Therefore, future demonstrations should be guided by techno-economic analysis and life-cycle assessment at the design stage, with levelized product cost and carbon intensity reported together with catalytic performance. In the near term, deployment should prioritize low-cost point-source CO_2 and renewable H_2 to establish economically favorable scenarios. In the long term, cost parity with fossil-derived products and verified life-cycle carbon reduction should become the criteria for industrial relevance.

Acknowledgments This work was supported by National Key Research and Development Program of China (No. 2023YFC3710800) and National Natural Science Foundation of China (NSFC No. 22376207).

Author Contributions Yanlin Liao contributed to investigation, writing—original draft, writing—review & editing. Ying Luo contributed to investigation, writing—original draft, writing—review & editing, and funding acquisition. Zheng Wang contributed to conceptualization, investigation, writing—original draft, writing—review & editing, funding acquisition, and supervision. Qiang Wang contributed to conceptualization, writing—review & editing, and supervision. Hong He contributed to conceptualization, writing—review & editing, funding acquisition, and supervision. All authors have approved the final manuscript.

Declarations

Conflict of interest The authors declare no interest conflict. They have no known competing financial interests or personal relationships that could have appeared to influence the work reported in this paper.

Open Access This article is licensed under a Creative Commons Attribution 4.0 International License, which permits use, sharing, adaptation, distribution and reproduction in any medium or format, as long as you give appropriate credit to the original author(s) and the source, provide a link to the Creative Commons licence, and indicate if changes were made. The images or other third party material in this article are included in the article's Creative Commons licence, unless indicated otherwise in a credit line to the material. If material is not included in the article's Creative Commons licence and your intended use is not permitted by statutory regulation or exceeds the permitted use, you will need to obtain permission directly from the copyright holder. To view a copy of this licence, visit http://creativecommons.org/licenses/by/4.0/.

References

1. Z. Liu, P. Ciais, Z. Deng, S.J. Davis, B. Zheng et al., Carbon Monitor, a near-real-time daily dataset of global CO_2 emission from fossil fuel and cement production. Sci. Data **7**, 392 (2020). https://doi.org/10.1038/s41597-020-00708-7
2. S. Piao, P. Ciais, Y. Huang, Z. Shen, S. Peng et al., The impacts of climate change on water resources and agriculture in China. Nature **467**(7311), 43–51 (2010). https://doi.org/10.1038/nature09364
3. R.M. Cuéllar-Franca, A. Azapagic, Carbon capture, storage and utilisation technologies: a critical analysis and comparison of their life cycle environmental impacts. J. CO2 Util. **9**, 82–102 (2015). https://doi.org/10.1016/j.jcou.2014.12.001
4. M. Bui, C.S. Adjiman, A. Bardow, E.J. Anthony, A. Boston et al., Carbon capture and storage (CCS): the way forward. Energy Environ. Sci. **11**(5), 1062–1176 (2018). https://doi.org/10.1039/c7ee02342a
5. Z. Zhang, T. Wang, M.J. Blunt, E.J. Anthony, A.A. Park et al., Advances in carbon capture, utilization and storage. Appl. Energy **278**, 115627 (2020). https://doi.org/10.1016/j.apenergy.2020.115627
6. C. Hepburn, E. Adlen, J. Beddington, E.A. Carter, S. Fuss et al., The technological and economic prospects for CO_2 utilization and removal. Nature **575**(7781), 87–97 (2019). https://doi.org/10.1038/s41586-019-1681-6

7. Z. Zhang, S.-Y. Pan, H. Li, J. Cai, A.G. Olabi et al., Recent advances in carbon dioxide utilization. Renew. Sustain. Energy Rev. **125**, 109799 (2020). https://doi.org/10.1016/j.rser.2020.109799
8. Y. Yang, Y. Zhang, J.S. Hu, L.J. Wan, Progress in the mechanisms and materials for CO_2 electroreduction toward C_{2+} products. Acta Phys. Chim. Sin. **36**(1), 70–82 (2020). https://doi.org/10.3866/PKU.WHXB201906085
9. B. Chang, H. Pang, F. Raziq, S. Wang, K.-W. Huang et al., Electrochemical reduction of carbon dioxide to multicarbon (C_{2+}) products: challenges and perspectives. Energy Environ. Sci. **16**(11), 4714–4758 (2023). https://doi.org/10.1039/d3ee00964e
10. F. Wang, Artificial photosynthetic systems for CO_2 reduction: progress on higher efficiency with cobalt complexes as catalysts. Chemsuschem **10**(22), 4393–4402 (2017). https://doi.org/10.1002/cssc.201701385
11. S. Chen, Y. Qi, C. Li, K. Domen, F. Zhang, Surface strategies for particulate photocatalysts toward artificial photosynthesis. Joule **2**(11), 2260–2288 (2018). https://doi.org/10.1016/j.joule.2018.07.030
12. L. Guo, J. Sun, Q. Ge, N. Tsubaki, Recent advances in direct catalytic hydrogenation of carbon dioxide to valuable C_{2+} hydrocarbons. J. Mater. Chem. A **6**(46), 23244–23262 (2018). https://doi.org/10.1039/c8ta05377d
13. J. Hu, Y. Cai, J. Xie, D. Hou, L. Yu et al., Selectivity control in CO_2 hydrogenation to one-carbon products. Chem **10**(4), 1084–1117 (2024). https://doi.org/10.1016/j.chempr.2024.02.017
14. C. Lv, X. Bai, S. Ning, C. Song, Q. Guan et al., Nanostructured materials for photothermal carbon dioxide hydrogenation: regulating solar utilization and catalytic performance. ACS Nano **17**(3), 1725–1738 (2023). https://doi.org/10.1021/acsnano.2c09025
15. Z. Wang, Z. Yang, Z.C. Kadirova, M. Guo, R. Fang et al., Photothermal functional material and structure for photothermal catalytic CO_2 reduction: recent advance, application and prospect. Coord. Chem. Rev. **473**, 214794 (2022). https://doi.org/10.1016/j.ccr.2022.214794
16. Y. Song, X. Zhang, K. Xie, G. Wang, X. Bao, High-temperature CO_2 electrolysis in solid oxide electrolysis cells: developments, challenges, and prospects. Adv. Mater. **31**(50), 1902033 (2019). https://doi.org/10.1002/adma.201902033
17. X. Zhang, Y. Song, G. Wang, X. Bao, Co-electrolysis of CO_2 and H_2O in high-temperature solid oxide electrolysis cells: recent advance in cathodes. J. Energy Chem. **26**(5), 839–853 (2017). https://doi.org/10.1016/j.jechem.2017.07.003
18. S. Yoshino, T. Takayama, Y. Yamaguchi, A. Iwase, A. Kudo, CO_2 reduction using water as an electron donor over heterogeneous photocatalysts aiming at artificial photosynthesis. Acc. Chem. Res. **55**(7), 966–977 (2022). https://doi.org/10.1021/acs.accounts.1c00676
19. E. Boutin, L. Merakeb, B. Ma, B. Boudy, M. Wang et al., Molecular catalysis of CO_2 reduction: recent advances and perspectives in electrochemical and light-driven processes with selected Fe, Ni and Co aza macrocyclic and polypyridine complexes. Chem. Soc. Rev. **49**, 5772 (2020). https://doi.org/10.1039/d0cs00218f
20. J. Ma, J. Yu, G. Chen, Y. Bai, S. Liu et al., Rational design of N-doped carbon-coated cobalt nanoparticles for highly efficient and durable photothermal CO_2 conversion. Adv. Mater. **35**(42), 2302537 (2023). https://doi.org/10.1002/adma.202302537
21. Y. Wan, F. Fang, R. Sun, J. Zhang, K. Chang, Metal oxide semiconductors for photothermal catalytic CO_2 hydrogenation reactions: recent progress and perspectives. Acta Phys. Chim. Sin. (2023). https://doi.org/10.3866/pku.whxb202212042
22. X. Cui, Q. Ruan, X. Zhuo, X. Xia, J. Hu et al., Photothermal nanomaterials: a powerful light-to-heat converter. Chem. Rev. **123**(11), 6891–6952 (2023). https://doi.org/10.1021/acs.chemrev.3c00159
23. S. Luo, X. Ren, H. Lin, H. Song, J. Ye, Plasmonic photothermal catalysis for solar-to-fuel conversion: current status and prospects. Chem. Sci. **12**(16), 5701–5719 (2021). https://doi.org/10.1039/d1sc00064k
24. M. Ghoussoub, M. Xia, P.N. Duchesne, D. Segal, G. Ozin, Principles of photothermal gas-phase heterogeneous CO_2 catalysis. Energy Environ. Sci. **12**(4), 1122–1142 (2019). https://doi.org/10.1039/c8ee02790k
25. W. Zhou, K. Cheng, J. Kang, C. Zhou, V. Subramanian et al., New horizon in C1 chemistry: breaking the selectivity limitation in transformation of syngas and hydrogenation of CO_2 into hydrocarbon chemicals and fuels. Chem. Soc. Rev. **48**(12), 3193–3228 (2019). https://doi.org/10.1039/c8cs00502h
26. S. Kasipandi, J.W. Bae, Recent advances in direct synthesis of value-added aromatic chemicals from syngas by cascade reactions over bifunctional catalysts. Adv. Mater. **31**(34), 1803390 (2019). https://doi.org/10.1002/adma.201803390
27. X. Zhu, H. Zong, C.J.V. Pérez, H. Miao, W. Sun et al., Supercharged CO_2 photothermal catalytic methanation: high conversion, rate, and selectivity. Angew. Chem. Int. Ed. **62**(22), e202218694 (2023). https://doi.org/10.1002/anie.202218694
28. H. Liu, T.D. Dao, L. Liu, X. Meng, T. Nagao et al., Light assisted CO_2 reduction with methane over group VIII metals: universality of metal localized surface plasmon resonance in reactant activation. Appl. Catal. B Environ. **209**, 183–189 (2017). https://doi.org/10.1016/j.apcatb.2017.02.080
29. J. Ding, P. Du, J. Zhu, Q. Hu, D. He et al., Light-driven C-C coupling for targeted synthesis of CH_3COOH with nearly 100 % selectivity from CO_2. Angew. Chem. Int. Ed. **63**(13), e202400828 (2024). https://doi.org/10.1002/anie.202400828
30. S. Wang, F. Li, J. Zhao, Y. Zeng, Y. Li et al., Manipulating C-C coupling pathway in electrochemical CO_2 reduction for selective ethylene and ethanol production over single-atom alloy catalyst. Nat. Commun. **15**, 10247 (2024). https://doi.org/10.1038/s41467-024-54636-w
31. S. Chen, T. Takata, K. Domen, Particulate photocatalysts for overall water splitting. Nat. Rev. Mater. **2**(10), 17050 (2017). https://doi.org/10.1038/natrevmats.2017.50

© The authors https://doi.org/10.1007/s40820-026-02351-0

32. Y. Dong, R. Song, Z. Zhang, X. Han, B. Wang et al., Advances in photothermal CO_2 hydrogenation catalysis for C1 molecules. Cell Rep. Phys. Sci. **5**(10), 102227 (2024). https://doi.org/10.1016/j.xcrp.2024.102227
33. W. Wang, C. Zeng, N. Tsubaki, Recent advancements and perspectives of the CO_2 hydrogenation reaction. Green Carbon **1**(2), 133–145 (2023). https://doi.org/10.1016/j.greenca.2023.10.003
34. H. Yang, K. Dai, J. Zhang, G. Dawson, Inorganic-organic hybrid photocatalysts: syntheses, mechanisms, and applications. Chin. J. Catal. **43**(8), 2111–2140 (2022). https://doi.org/10.1016/S1872-2067(22)64096-8
35. Z. Wang, C. Li, K. Domen, Recent developments in heterogeneous photocatalysts for solar-driven overall water splitting. Chem. Soc. Rev. **48**(7), 2109–2125 (2019). https://doi.org/10.1039/c8cs00542g
36. L. Zhang, C. Li, Y. Liu, C. Xu, Y. Zhang, Unraveling active sites regulation and temperature-dependent thermodynamic mechanism in photothermocatalytic CO_2 conversion with H_2O. npj Comput. Mater. **10**, 132 (2024). https://doi.org/10.1038/s41524-024-01325-3
37. Q. Li, Y. Gao, M. Zhang, H. Gao, J. Chen et al., Efficient infrared-light-driven photothermal CO_2 reduction over MOF-derived defective Ni/TiO_2. Appl. Catal. B Environ. **303**, 120905 (2022). https://doi.org/10.1016/j.apcatb.2021.120905
38. V. Georgakilas, J.A. Perman, J. Tucek, R. Zboril, Broad family of carbon nanoallotropes: classification, chemistry, and applications of fullerenes, carbon dots, nanotubes, graphene, nanodiamonds, and combined superstructures. Chem. Rev. **115**(11), 4744–4822 (2015). https://doi.org/10.1021/cr500304f
39. D. He, G. Huang, Z. Zhou, Q. Hu, J. Ding et al., Recent progress for designing of catalysts for photothermal conversion of plastic wastes. Adv. Funct. Mater. **36**(6), 2419801 (2026). https://doi.org/10.1002/adfm.202419801
40. Y. Liu, G. Tan, S. Feng, B. Zhang, T. Liu et al., Localized surface plasmon resonance effect of V_4C_3-MXene for enhancing photothermal reduction of CO_2 in full solar spectrum. Sep. Purif. Technol. **326**, 124726 (2023). https://doi.org/10.1016/j.seppur.2023.124726
41. J. Zhou, H. Liu, H. Wang, Photothermal catalysis for CO_2 conversion. Chin. Chem. Lett. **34**(2), 107420 (2023). https://doi.org/10.1016/j.cclet.2022.04.018
42. A. Gellé, T. Jin, L. de la Garza, G.D. Price, L.V. Besteiro et al., Applications of plasmon-enhanced nanocatalysis to organic transformations. Chem. Rev. **120**(2), 986–1041 (2020). https://doi.org/10.1021/acs.chemrev.9b00187
43. D. Mateo, J.L. Cerrillo, S. Durini, J. Gascon, Fundamentals and applications of photo-thermal catalysis. Chem. Soc. Rev. **50**(3), 2173–2210 (2021). https://doi.org/10.1039/d0cs00357c
44. H. Jiang, L. Wang, H. Kaneko, R. Gu, G. Su et al., Light-driven CO_2 methanation over Au-grafted $Ce_{0.95}Ru_{0.05}O_2$ solid-solution catalysts with activities approaching the thermodynamic limit. Nat. Catal. **6**(6), 519–530 (2023). https://doi.org/10.1038/s41929-023-00970-z
45. J. Zheng, L. Lu, K. Lebedev, S. Wu, P. Zhao et al., Fe on molecular-layer MoS_2 as inorganic Fe-S_2-Mo motifs for light-driven nitrogen fixation to ammonia at elevated temperatures. Chem. Catal. **1**(1), 162–182 (2021). https://doi.org/10.1016/j.checat.2021.03.002
46. J. Li, B. Sheng, L. Qiu, J. Yang, P. Wang et al., Photo-thermal synergistic CO_2 hydrogenation towards CO over PtRh bimetal-decorated GaN nanowires/Si. Chem. Sci. **15**(20), 7714–7724 (2024). https://doi.org/10.1039/d4sc01530d
47. S. Fang, Y.H. Hu, Thermo-photo catalysis: a whole greater than the sum of its parts. Chem. Soc. Rev. **51**(9), 3609–3647 (2022). https://doi.org/10.1039/d1cs00782c
48. R.-T. Guo, C. Xia, Z.-X. Bi, Z.-R. Zhang, W.-G. Pan, Recent progress of photothermal effect on photocatalytic reduction of CO_2. Fuel Process. Technol. **241**, 107617 (2023). https://doi.org/10.1016/j.fuproc.2022.107617
49. G. Baffou, I. Bordacchini, A. Baldi, R. Quidant, Simple experimental procedures to distinguish photothermal from hot-carrier processes in plasmonics. Light Sci. Appl. **9**, 108 (2020). https://doi.org/10.1038/s41377-020-00345-0
50. X. Wang, A. Rendón-Patiño, D. Mateo, J. Gascon, Highly selective photothermal CO_2 hydrogenation to C_2^+ hydrocarbons over Mn-modified K–Fe catalysts. EES Catal. **4**(3), 734–743 (2026). https://doi.org/10.1039/d6ey00013d
51. J. Wang, W. Liao, Y. Tan, O. Henrotte, Y. Kang et al., Transfer dynamics of photo-generated carriers in catalysis. Chem. Soc. Rev. **54**(13), 6553–6596 (2025). https://doi.org/10.1039/d5cs00512d
52. G. Kim, H.J. Choi, H.I. Kim, J. Kim, D. Monllor-Satoca et al., Temperature-boosted photocatalytic H_2 production and charge transfer kinetics on TiO_2 under UV and visible light. Photochem. Photobiol. Sci. **15**(10), 1247–1253 (2016). https://doi.org/10.1039/c6pp00263c
53. M. Wang, H. Mo, X. Zhang, J. Hong, C. Xu et al., Tuning recombination of carriers during radiative conversion with Cuprum and Ferrum co-doping in the photothermal synergy. Int. J. Hydrogen Energy **57**, 126–135 (2024). https://doi.org/10.1016/j.ijhydene.2023.12.287
54. R. Bai, J. Niu, X. Zhang, Q. Li, C. Dong et al., Enhanced photocatalytic CO_2 reduction in floatable CMF/Bi_2WO_6/C_3N_4 gas-liquid-solid three-phase heterojunction system. Appl. Catal. B Environ. Energy **374**, 125395 (2025). https://doi.org/10.1016/j.apcatb.2025.125395
55. L. Pei, H. Feng, Q. Mao, L. Wang, Y. Zhang et al., A synergistic photothermal-dual site strategy to accelerate proton–electron transfer enables enhanced CO_2-to-syngas conversion. J. Mater. Chem. A **13**(17), 12147–12158 (2025). https://doi.org/10.1039/d4ta09093d
56. Y. Ren, Y. Si, M. Du, C. You, C. Zhang et al., Photothermal synergistic effect induces bimetallic cooperation to modulate product selectivity of CO_2 reduction on different CeO_2 crystal facets. Angew. Chem. Int. Ed. **63**(46), e202410474 (2024). https://doi.org/10.1002/anie.202410474
57. Z. Luo, F. Yang, S. Zhang, G. He, C. Du et al., Engineering crystalline facets to boost the performance of Ru/$SrTiO_3$ in photo-thermal coupling hydrogenation of CO_2. Appl. Catal.

B Environ. Energy **375**, 125397 (2025). https://doi.org/10.1016/j.apcatb.2025.125397

58. J. Li, J. Zhao, S. Wang, K.-S. Peng, B. Su et al., Activating lattice oxygen in perovskite ferrite for efficient and stable photothermal dry reforming of methane. J. Am. Chem. Soc. **147**(17), 14705–14714 (2025). https://doi.org/10.1021/jacs.5c03098
59. J. Li, X. Hao, J. Zhao, J. Li, B. Su et al., Light-induced electronic structure modulation in perovskite ferrite for efficient photothermal dry reforming of methane. Chem. Sci. **17**(3), 1647–1655 (2026). https://doi.org/10.1039/d5sc05708f
60. X. Wan, Y. Zhao, Y. Li, J. Ma, Y. Gu et al., Tailoring oxygen vacancies with atomically dispersed Cu sites for stable and efficient photothermal CO_2 conversion. Angew. Chem. Int. Ed. **64**(30), e202505244 (2025). https://doi.org/10.1002/anie.202505244
61. Z. Zhao, D.E. Doronkin, Y. Ye, J.-D. Grunwaldt, Z. Huang et al., Visible light-enhanced photothermal CO_2 hydrogenation over Pt/Al_2O_3 catalyst. Chin. J. Catal. **41**(2), 286–293 (2020). https://doi.org/10.1016/S1872-2067(19)63445-5
62. B. Zhao, M. Sun, F. Chen, W. Wang, S. Lu et al., Photoinduced reaction pathway change for boosting CO_2 hydrogenation over a MnO-co catalyst. ACS Catal. **11**(16), 10316–10323 (2021). https://doi.org/10.1021/acscatal.1c02644
63. Y. Hu, J. Wu, Y. Han, W. Xu, L. Zhang et al., Intensified solar thermochemical CO_2 splitting over iron-based redox materials *via* perovskite-mediated dealloying-exsolution cycles. Chin. J. Catal. **42**(11), 2049–2058 (2021). https://doi.org/10.1016/S1872-2067(21)63857-3
64. Q. Wu, J. Wang, D. Yuan, Y. Wang, Y. Li et al., Ambient sunlight driven photothermal green syngas production at 100 m^3 scale by the dynamic structural reconstruction of iron oxides with 38.7% efficiency. Adv. Funct. Mater. **35**(2), 2412562 (2025). https://doi.org/10.1002/adfm.202412562
65. K. Wang, M. Cao, J. Lu, Y. Lu, C.H. Lau et al., Operando DRIFTS-MS investigation on plasmon-thermal coupling mechanism of CO2 hydrogenation on Au/TiO2: the enhanced generation of oxygen vacancies. Appl. Catal. B Environ. **296**, 120341 (2021). https://doi.org/10.1016/j.apcatb.2021.120341
66. X. Yue, D. Zheng, M. Gao, K. Wang, Z. Zhang et al., CO_2 adsorption-mediated oxygen defects for photothermal catalysis self-decomposition over low-crystalline Nb_2O_5 nanoribbons. ACS Catal. **13**(24), 15841–15850 (2023). https://doi.org/10.1021/acscatal.3c04590
67. J. Yu, A. Muhetaer, X. Gao, Z. Zhang, Y. Yang et al., Highly active hydrogen-rich photothermal reverse water gas shift reaction on $Ni/LaInO_3$ perovskite catalysts with near-unity selectivity. Angew. Chem. Int. Ed. **62**(28), e202303135 (2023). https://doi.org/10.1002/anie.202303135
68. Y. Li, X. Bai, D. Yuan, C. Yu, X. San et al., Cu-based high-entropy two-dimensional oxide as stable and active photothermal catalyst. Nat. Commun. **14**, 3171 (2023). https://doi.org/10.1038/s41467-023-38889-5
69. Y. Li, M. Wen, Y. Wang, G. Tian, C. Wang et al., Plasmonic hot electrons from oxygen vacancies for infrared light-driven catalytic CO_2 reduction on Bi_2O_{3-x}. Angew. Chem. Int. Ed. **60**(2), 910–916 (2021). https://doi.org/10.1002/anie.202010156
70. K.K. Ghuman, T.E. Wood, L.B. Hoch, C.A. Mims, G.A. Ozin et al., Illuminating CO_2 reduction on frustrated Lewis pair surfaces: investigating the role of surface hydroxides and oxygen vacancies on nanocrystalline $In_2O_{(3-x)}(OH)_y$. Phys. Chem. Chem. Phys. **17**(22), 14623–14635 (2015). https://doi.org/10.1039/c5cp02613j
71. Y. Qi, L. Song, S. Ouyang, X. Liang, S. Ning et al., Photoinduced defect engineering: enhanced photothermal catalytic performance of 2D black In_2O_{3-x} nanosheets with bifunctional oxygen vacancies. Adv. Mater. Deerfield Beach Fla **32**(6), e1903915 (2020). https://doi.org/10.1002/adma.201903915
72. S. Ning, H. Xu, Y. Qi, L. Song, Q. Zhang et al., Microstructure induced thermodynamic and kinetic modulation to enhance CO_2 photothermal reduction: a case of atomic-scale dispersed co–N species anchored Co@C hybrid. ACS Catal. **10**(8), 4726–4736 (2020). https://doi.org/10.1021/acscatal.9b04963
73. J. Zhao, Q. Yang, R. Shi, G.I.N. Waterhouse, X. Zhang et al., FeO–CeO_2 nanocomposites: an efficient and highly selective catalyst system for photothermal CO_2 reduction to CO. NPG Asia Mater. **12**, 5 (2020). https://doi.org/10.1038/s41427-019-0171-5
74. X. Wang, A. Rendón-Patiño, J.M.R. Gallo, D. Mateo, J. Gascon, Alkali-promoted indium oxide as a highly active and selective catalyst for photo-thermal CO_2 hydrogenation. J. Mater. Chem. A **12**(35), 23541–23550 (2024). https://doi.org/10.1039/d4ta04387a
75. Z. Yang, T. Zhao, Y. Tang, Y. Jiang, H. Kitagawa et al., Size-modulated photo-thermal catalytic CO_2 hydrogenation performances over Pd nanoparticles. J. Catal. **424**, 22–28 (2023). https://doi.org/10.1016/j.jcat.2023.05.007
76. Y. Tang, S. Wu, Y. Wang, L. Song, Z. Yang et al., Photo-assisted catalytic CO_2 hydrogenation to CO with nearly 100% selectivity over Rh/TiO_2 catalysts. Energy Fuels **37**(1), 539–546 (2023). https://doi.org/10.1021/acs.energyfuels.2c03604
77. B. Deng, H. Song, K. Peng, Q. Li, J. Ye, Metal-organic framework-derived $Ga-Cu/CeO_2$ catalyst for highly efficient photothermal catalytic CO_2 reduction. Appl. Catal. B Environ. **298**, 120519 (2021). https://doi.org/10.1016/j.apcatb.2021.120519
78. S. Liu, X. Wang, Y. Chen, Y. Li, Y. Wei et al., Efficient thermal management with selective metamaterial absorber for boosting photothermal CO_2 hydrogenation under sunlight. Adv. Mater. Deerfield Beach Fla **36**(21), e2311957 (2024). https://doi.org/10.1002/adma.202311957
79. S. Singh, R. Verma, N. Kaul, J. Sa, A. Punjal et al., Surface plasmon-enhanced photo-driven CO_2 hydrogenation by hydroxy-terminated nickel nitride nanosheets. Nat. Commun. **14**(1), 2551 (2023). https://doi.org/10.1038/s41467-023-38235-9
80. X. Wan, Y. Li, Y. Chen, J. Ma, Y.-A. Liu et al., A nonmetallic plasmonic catalyst for photothermal CO_2 flow conversion with high activity, selectivity and durability. Nat.

© The authors https://doi.org/10.1007/s40820-026-02351-0

Commun. **15**(1), 1273 (2024). https://doi.org/10.1038/s41467-024-45516-4

81. H. Wang, S. Fu, B. Shang, S. Jeon, Y. Zhong et al., Solar-driven CO_2 conversion *via* optimized photothermal catalysis in a lotus pod structure. Angew. Chem. Int. Ed. **62**(30), e202305251 (2023). https://doi.org/10.1002/anie.202305251
82. Y. Peng, H. Szalad, P. Nikacevic, G. Gorni, S. Goberna et al., Co-doped hydroxyapatite as photothermal catalyst for selective CO_2 hydrogenation. Appl. Catal. B Environ. Energy **333**, 122790 (2023). https://doi.org/10.1016/j.apcatb.2023.122790
83. G.A. Martin, M. Primet, J.A. Dalmon, Reactions of CO and CO_2 on Ni SiO_2 above 373 K as studied by infrared spectroscopic and magnetic methods. J. Catal. **53**(3), 321–330 (1978). https://doi.org/10.1016/0021-9517(78)90104-5
84. Y. Li, Z. Liu, Z. Rao, F. Yu, W. Bao et al., Experimental and theoretical insights into an enhanced CO_2 methanation mechanism over a Ru-based catalyst. Appl. Catal. B Environ. **319**, 121903 (2022). https://doi.org/10.1016/j.apcatb.2022.121903
85. T. Yang, H. Yang, B. Su, X. Lin, X.F. Lu et al., Regulating product selectivity in photothermal CO_2 conversion through Ni loading on metallic MoO_2. ACS Sustain. Chem. Eng. **14**(1), 827–836 (2026). https://doi.org/10.1021/acssuschemeng.5c12251
86. J. Ma, T. Liu, G. Chen, S. Liu, W. Gong et al., Tuning the selectivity of photothermal CO_2 hydrogenation through photo-induced interaction between Ni nanoparticles and TiO_2. Appl. Catal. B Environ. Energy **344**, 123600 (2024). https://doi.org/10.1016/j.apcatb.2023.123600
87. Y. Yang, J. Liu, F. Liu, D. Wu, Reaction mechanism of CO_2 methanation over Rh/TiO_2 catalyst. Fuel **276**, 118093 (2020). https://doi.org/10.1016/j.fuel.2020.118093
88. S. Sun, M.D. Higham, X. Zhang, C.R.A. Catlow, Multi-scale investigation of the mechanism and selectivity of CO_2 hydrogenation over Rh(111). ACS Catal. **14**(8), 5503–5519 (2024). https://doi.org/10.1021/acscatal.3c05939
89. Y. Tang, H. Wang, C. Guo, Z. Yang, T. Zhao et al., Ruthenium-cobalt solid-solution alloy nanoparticles for enhanced photopromoted thermocatalytic CO_2 hydrogenation to methane. ACS Nano **18**(17), 11449–11461 (2024). https://doi.org/10.1021/acsnano.4c02416
90. X. Zhang, X. Xu, B. Su, X. Lin, K. Liu et al., Efficient photothermal CO_2 methanation over Ni nanoparticles on oxygen-deficient V_2O_3 *via* strong metal-support interaction. Sci. China Chem. **69**(4), 2024–2029 (2026). https://doi.org/10.1007/s11426-025-2963-6
91. Y. Tang, T. Zhao, H. Han, Z. Yang, J. Liu et al., Ir-CoO active centers supported on porous Al_2O_3 nanosheets as efficient and durable photo-thermal catalysts for CO_2 conversion. Adv. Sci. **10**(15), e2300122 (2023). https://doi.org/10.1002/advs.202300122
92. Z. Yang, Z.-Y. Wu, Z. Lin, T. Liu, L. Ding et al., Optically selective catalyst design with minimized thermal emission for facilitating photothermal catalysis. Nat. Commun. **15**, 7599 (2024). https://doi.org/10.1038/s41467-024-51896-4
93. F. Raziq, C. Feng, M. Hu, S. Zuo, M.Z. Rahman et al., Isolated Ni atoms enable near-unity CH_4 selectivity for photothermal CO_2 hydrogenation. J. Am. Chem. Soc. **146**(30), 21008–21016 (2024). https://doi.org/10.1021/jacs.4c05873
94. Y. Gu, J. Ding, X. Tong, H. Yao, R. Yang et al., Photothermal catalyzed hydrogenation of carbon dioxide over porous nanosheet Co_3O_4. J. CO2 Util. **61:** 102003 (2022). https://doi.org/10.1016/j.jcou.2022.102003
95. H. Ge, Y. Kuwahara, K. Kusu, Z. Bian, H. Yamashita, Ru/H x MoO_{3-y} with plasmonic effect for boosting photothermal catalytic CO_2 methanation. Appl. Catal. B Environ. **317**, 121734 (2022). https://doi.org/10.1016/j.apcatb.2022.121734
96. C. Guo, Y. Tang, Z. Yang, T. Zhao, J. Liu et al., Reinforcing the efficiency of photothermal catalytic CO_2 methanation through integration of Ru nanoparticles with photothermal $MnCo_2O_4$ nanosheets. ACS Nano **17**(23), 23761–23771 (2023). https://doi.org/10.1021/acsnano.3c07630
97. J. Zhai, Z. Xia, B. Zhou, H. Wu, T. Xue et al., Photo-thermal coupling to enhance CO_2 hydrogenation toward CH_4 over Ru/MnO/Mn_3O_4. Nat. Commun. **15**(1), 1109 (2024). https://doi.org/10.1038/s41467-024-45389-7
98. Z.-Y. Zhang, T. Li, X.-L. Sun, D.-C. Luo, J.-L. Yao et al., Efficient photo-thermal catalytic CO_2 methanation and dynamic structural evolution over Ru/Mg-CeO_2 single-atom catalyst. J. Catal. **430**, 115303 (2024). https://doi.org/10.1016/j.jcat.2024.115303
99. D. Pan, Y. Wang, H. Li, Y. Zhang, Q. Liang et al., Solar light promoted CO_2 hydrogenation to CH_4 over photo-thermal responsive dispersed Co on defective CeO_2 composite derived from MOFs. Sep. Purif. Technol. **332**, 125756 (2024). https://doi.org/10.1016/j.seppur.2023.125756
100. K. Zhang, C. Xu, X. Zhang, Z. Huang, Q. Pian et al., Structural heredity in catalysis: CO_2 self-selective CeO_2 nanocrystals for efficient photothermal CO_2 hydrogenation to methane. Small **20**(21), 2308823 (2024). https://doi.org/10.1002/smll.202308823
101. Q. Li, C. Wang, H. Wang, J. Chen, J. Chen et al., Disclosing support-size-dependent effect on ambient light-driven photothermal CO_2 hydrogenation over nickel/titanium dioxide. Angew. Chem. Int. Ed. **63**(10), e202318166 (2024). https://doi.org/10.1002/anie.202318166
102. H. Wang, Q. Li, J. Chen, J. Chen, H. Jia, Efficient solar-driven CO_2 methanation and hydrogen storage over nickel catalyst derived from metal–organic frameworks with rich oxygen vacancies. Adv. Sci. **10**(34), 2304406 (2023). https://doi.org/10.1002/advs.202304406
103. X. Yu, X. Ding, Y. Yao, W. Gao, C. Wang et al., Layered high-entropy metallic glasses for photothermal CO_2 methanation. Adv. Mater. **36**(21), e2312942 (2024). https://doi.org/10.1002/adma.202312942
104. Y. Tang, Z. Yang, C. Guo, H. Han, Y. Jiang et al., Encapsulating Ir nanoparticles into UiO-66 for photo-thermal catalytic CO_2 methanation under ambient pressure. J. Mater. Chem. A **10**(22), 12157–12167 (2022). https://doi.org/10.1039/d2ta00933a

105. L. Wang, Y. Qi, Z. Yang, H. Wu, J. Liu et al., Pt nanoparticles supported $LaCoO_3$ as highly efficient catalysts for photo-thermal catalytic CO_2 methanation. Green Energy Resour. **1**(4), 100036 (2023). https://doi.org/10.1016/j.gerr.2023.100036
106. C.F. Shih, T. Zhang, J. Li, C. Bai, Powering the future with liquid sunshine. Joule **2**(10), 1925–1949 (2018). https://doi.org/10.1016/j.joule.2018.08.016
107. A.A. Tountas, X. Peng, A.V. Tavasoli, P.N. Duchesne, T.L. Dingle et al., Towards solar methanol: past, present, and future. Adv. Sci. **6**(8), 1801903 (2019). https://doi.org/10.1002/advs.201801903
108. B. Deng, H. Song, Q. Wang, J. Hong, S. Song et al., Highly efficient and stable photothermal catalytic CO_2 hydrogenation to methanol over Ru/In_2O_3 under atmospheric pressure. Appl. Catal. B Environ. **327**, 122471 (2023). https://doi.org/10.1016/j.apcatb.2023.122471
109. S. Ren, J. Han, Z. Yang, J. Liang, S. Feng et al., Near-unity photothermal CO_2 hydrogenation to methanol based on a molecule/nanocarbon hybrid catalyst. Angew. Chem. Int. Ed. **64**(4), e202416376 (2025). https://doi.org/10.1002/anie.202416376
110. L. Wang, M. Ghoussoub, H. Wang, Y. Shao, W. Sun et al., Photocatalytic hydrogenation of carbon dioxide with high selectivity to methanol at atmospheric pressure. Joule **2**(7), 1369–1381 (2018). https://doi.org/10.1016/j.joule.2018.03.007
111. J. Chen, D. Zhang, B. Liu, K. Zheng, Y. Li et al., Photoinduced precise synthesis of diatomic Ir_1Pd_1-In_2O_3 for CO_2 hydrogenation to methanol *via* angstrom-scale-distance dependent synergistic catalysis. Angew. Chem. Int. Ed. **63**(13), e202401168 (2024). https://doi.org/10.1002/anie.202401168
112. H.-X. Fan, T. Liu, L.-F. Zhen, A. Rajendran, J. Feng et al., Evaluating the role of oxygen vacancies in CO_2 photothermal catalytic reduction to methanol over 2D Bi_2WO_6. Sci. China Mater. **68**(2), 464–471 (2025). https://doi.org/10.1007/s40843-024-3199-9
113. T. Yan, L. Wang, Y. Liang, M. Makaremi, T.E. Wood et al., Polymorph selection towards photocatalytic gaseous CO_2 hydrogenation. Nat. Commun. **10**(1), 2521 (2019). https://doi.org/10.1038/s41467-019-10524-2
114. T. Yan, N. Li, L. Wang, W. Ran, P.N. Duchesne et al., Bismuth atom tailoring of indium oxide surface frustrated Lewis pairs boosts heterogeneous CO_2 photocatalytic hydrogenation. Nat. Commun. **11**(1), 6095 (2020). https://doi.org/10.1038/s41467-020-19997-y
115. Z. Lu, Y. Xu, Z. Zhang, J. Sun, X. Ding et al., Wettability engineering of solar methanol synthesis. J. Am. Chem. Soc. **145**(48), 26052–26060 (2023). https://doi.org/10.1021/jacs.3c07349
116. L. Wang, D. Yao, C. Zhang, Y. Chen, L. Amirav et al., Photothermal catalytic CO_2 hydrogenation to methanol on Au/In_2O_3 nanowires. Chem. Catal. **4**(9), 101095 (2024). https://doi.org/10.1016/j.checat.2024.101095
117. L.-L. Ling, W. Yang, P. Yan, M. Wang, H.-L. Jiang, Light-assisted CO_2 hydrogenation over Pd_3Cu@UiO-66 promoted by active sites in close proximity. Angew. Chem. Int. Ed. **61**(12), e202116396 (2022). https://doi.org/10.1002/anie.202116396
118. Z. Jiang, Z. Yuan, P.N. Duchesne, W. Sun, X. Lyu et al., A living photocatalyst derived from $CaCu_3Ti_4O_{12}$ for CO_2 hydrogenation to methanol at atmospheric pressure. Chem. Catal. **3**(2), 100507 (2023). https://doi.org/10.1016/j.checat.2023.100507
119. Z.-J. Wang, H. Song, H. Pang, Y. Ning, T.D. Dao et al., Photo-assisted methanol synthesis *via* CO_2 reduction under ambient pressure over plasmonic Cu/ZnO catalysts. Appl. Catal. B Environ. **250**, 10–16 (2019). https://doi.org/10.1016/j.apcatb.2019.03.003
120. Z. Zhang, C. Mao, D.M. Meira, P.N. Duchesne, A.A. Tountas et al., New black indium oxide: tandem photothermal CO_2-H_2 methanol selective catalyst. Nat. Commun. **13**, 1512 (2022). https://doi.org/10.1038/s41467-022-29222-7
121. B. Tahir, M. Tahir, N.S. Amin, Performance analysis of monolith photoreactor for CO_2 reduction with H_2. Energy Convers. Manag. **90**, 272–281 (2015). https://doi.org/10.1016/j.enconman.2014.11.018
122. A.V. Puga, A. Corma, Hydrogenation of CO_2 on nickel–iron nanoparticles under sunlight irradiation. Top. Catal. **61**(18–19), 1810–1819 (2018). https://doi.org/10.1007/s11244-018-1030-2
123. Z. Wang, M. Xiao, X. Wang, H. Wang, X. Chen et al., Thermo-driven photocatalytic CO_2 hydrogenation over $NiOx/Nb_2O_5$ *via* regulating the electron transfer behavior of reactant gas adsorption. Appl. Surf. Sci. **592**, 153246 (2022). https://doi.org/10.1016/j.apsusc.2022.153246
124. L. Liu, A.V. Puga, J. Cored, P. Concepción, V. Pérez-Dieste et al., Sunlight-assisted hydrogenation of CO_2 into ethanol and C_{2+} hydrocarbons by sodium-promoted Co@C nanocomposites. Appl. Catal. B-Environ. **235**, 186–196 (2018). https://doi.org/10.1016/j.apcatb.2018.04.060
125. Z.-H. He, Z.-H. Li, Z.-Y. Wang, K. Wang, Y.-C. Sun et al., Photothermal CO_2 hydrogenation to hydrocarbons over trimetallic Co–Cu–Mn catalysts. Green Chem. **23**(16), 5775–5785 (2021). https://doi.org/10.1039/d1gc01152a
126. C. Song, X. Liu, M. Xu, D. Masi, Y. Wang et al., Photothermal conversion of CO_2 with tunable selectivity using Fe-based catalysts: from oxide to carbide. ACS Catal. **10**(18), 10364–10374 (2020). https://doi.org/10.1021/acscatal.0c02244
127. C. Song, Z. Wang, J. Zhao, X. Qin, M. Peng et al., Photothermal conversion of CO_2 into lower olefins at the interface of the K-promoted Ru/Fe_3O_4 catalyst. Chem. Catal. **4**(4), 100960 (2024). https://doi.org/10.1016/j.checat.2024.100960
128. G. Chen, R. Gao, Y. Zhao, Z. Li, G.I.N. Waterhouse et al., Alumina-supported CoFe alloy catalysts derived from layered-double-hydroxide nanosheets for efficient photothermal CO_2 hydrogenation to hydrocarbons. Adv. Mater. **30**(3), 1704663 (2018). https://doi.org/10.1002/adma.201704663

© The authors https://doi.org/10.1007/s40820-026-02351-0

129. Z. Li, J. Liu, R. Shi, G.I.N. Waterhouse, X.-D. Wen et al., Fe-based catalysts for the direct photohydrogenation of CO_2 to value-added hydrocarbons. Adv. Energy Mater. **11**(12), 2002783 (2021). https://doi.org/10.1002/aenm.202002783
130. S. Ning, X. Wu, H. Song, X. Ma, S. Yue et al., Light-field orchestrated tandem photothermal catalysis for highly selective CO_2-to-C_{2+} olefin conversion. J. Am. Chem. Soc. **148**(1), 1728–1740 (2026). https://doi.org/10.1021/jacs.5c18890
131. X. Bai, L. Han, J. Wang, Y. Luo, Y. Li et al., C-C coupling regulation to enhance the stability of ambient pressure photothermal CO_2 hydrogenation to multi-hydrocarbon compounds. Catal. Sci. Technol. **15**(15), 4457–4461 (2025). https://doi.org/10.1039/d5cy00535c
132. J. Zhao, R. Shi, G.I.N. Waterhouse, T. Zhang, Selective photothermal CO_2 reduction to CO, CH_4, alkanes, alkenes over bimetallic alloy catalysts derived from layered double hydroxide nanosheets. Nano Energy **102**, 107650 (2022). https://doi.org/10.1016/j.nanoen.2022.107650
133. R. Song, Z. Li, J. Guo, P.N. Duchesne, C. Qiu et al., Solar hydrocarbons: single-step, atmospheric-pressure synthesis of C_2–C_4 alkanes and alkenes from CO_2. Angew. Chem. Int. Ed. **62**(27), e202304470 (2023). https://doi.org/10.1002/anie.202304470
134. S. Ning, H. Ou, Y. Li, C. Lv, S. Wang et al., Co^0-$co^{\delta+}$ interface double-site-mediated C-C coupling for the photothermal conversion of CO_2 into light olefins. Angew. Chem. Int. Ed. **62**(23), e202302253 (2023). https://doi.org/10.1002/anie.202302253
135. S. Ning, J. Wang, X. Wu, L. Li, S. Zhang et al., Natural sunlight-driven CO_2 hydrogenation into light olefins at ambient pressure over bifunctional Cu-promoted CoFe alloy catalyst. Adv. Funct. Mater. **34**(30), 2400798 (2024). https://doi.org/10.1002/adfm.202400798
136. P. Li, L. Liu, W. An, H. Wang, H. Guo et al., Ultrathin porous g-C_3N_4 nanosheets modified with AuCu alloy nanoparticles and C-C coupling photothermal catalytic reduction of CO to ethanol. Appl. Catal. B Environ. **266**, 118618 (2020). https://doi.org/10.1016/j.apcatb.2020.118618
137. J. Zhu, W. Shao, X. Li, X. Jiao, J. Zhu et al., Asymmetric triple-atom sites confined in ternary oxide enabling selective CO_2 photothermal reduction to acetate. J. Am. Chem. Soc. **143**(43), 18233–18241 (2021). https://doi.org/10.1021/jacs.1c08033
138. W. Ma, S. Xie, T. Liu, Q. Fan, J. Ye et al., Electrocatalytic reduction of CO_2 to ethylene and ethanol through hydrogen-assisted C-C coupling over fluorine-modified copper. Nat. Catal. **3**(6), 478–487 (2020). https://doi.org/10.1038/s41929-020-0450-0
139. C. Ren, Q. Li, C. Ling, J. Wang, Mechanism-guided design of photocatalysts for CO_2 reduction toward multicarbon products. J. Am. Chem. Soc. **145**(51), 28276–28283 (2023). https://doi.org/10.1021/jacs.3c11972
140. X. Li, L. Li, X. Chu, X. Liu, G. Chen et al., Photothermal CO_2 conversion to ethanol through photothermal heterojunction-nanosheet arrays. Nat. Commun. **15**(1), 5639 (2024). https://doi.org/10.1038/s41467-024-49928-0
141. J. Liang, Y. Wang, B. Meng, H. Liu, L. Jiang et al., Efficient product regulation of CO_2 hydrogenation over an intelligent dual-zeolite system. J. Am. Chem. Soc. **147**(49), 45793–45807 (2025). https://doi.org/10.1021/jacs.5c18916
142. K. Cheng, Y. Li, J. Kang, Q. Zhang, Y. Wang, Selectivity control by relay catalysis in CO and CO_2 hydrogenation to multicarbon compounds. Acc. Chem. Res. **57**(5), 714–725 (2024). https://doi.org/10.1021/acs.accounts.3c00734
143. S. Chen, J. Wang, Z. Feng, Y. Jiang, H. Hu et al., Hydrogenation of CO_2 to light olefins over $ZnZrO_x$/SSZ-13. Angew. Chem. Int. Ed. **63**(8), e202316874 (2024). https://doi.org/10.1002/anie.202316874
144. J. Li, Z. Wei, Y. Chen, B. Jing, Y. He et al., A route to form initial hydrocarbon pool species in methanol conversion to olefins over zeolites. J. Catal. **317**, 277–283 (2014). https://doi.org/10.1016/j.jcat.2014.05.015
145. F. Mahnaz, V. Dunlap, R. Helmer, S.S. Borkar, R. Navar et al., Selective valorization of CO_2 towards valuable hydrocarbons through methanol-mediated tandem catalysis. ChemCatChem **15**(17), e202300402 (2023). https://doi.org/10.1002/cctc.202300402
146. H. Tian, P. Gao, X. Yang, C. Jiao, F. Zha et al., Tandem composite of M (Zn, Ga, In)-UIO-66/(HZSM-5)-palygorskite for hydrogenation of carbon dioxide to aromatics. Chem. Eng. J. **466**, 143267 (2023). https://doi.org/10.1016/j.cej.2023.143267
147. H. Tian, P. Gao, X. Yang, C. Jiao, F. Zha et al., Reaction mechanisms and catalytic performance of CO_2 to aromatics over M(ZnO, Ga_2O_3, In_2O_3)-UiO-66 catalysts without zeolite. ACS Sustain. Chem. Eng. **11**(39), 14334–14347 (2023). https://doi.org/10.1021/acssuschemeng.3c00995
148. Z. Sun, Z. Gao, R. Ma, Q. Xu, B. Shao et al., Boosting CO_2 hydrogenation to light olefins with low CO selectivity through promoting HCOO* intermediates on Fe-$ZnGa_2O_4$/SAPO-34. Appl. Catal. B Environ. Energy **358**, 124358 (2024). https://doi.org/10.1016/j.apcatb.2024.124358
149. T. Liu, Z. Liu, S. Jiang, P. Peng, Z. Liu et al., Selectivity control by zeolites during methanol-mediated CO_2 hydrogenation processes. Chem. Soc. Rev. **54**(6), 2726–2761 (2025). https://doi.org/10.1039/d4cs01042f
150. R. Ma, W. Chen, L. Wang, X. Yi, Y. Xiao et al., *N*-Oxyl radicals trapped on zeolite surface accelerate photocatalysis. ACS Catal. **9**(11), 10448–10453 (2019). https://doi.org/10.1021/acscatal.9b03737
151. L. Emdadi, D.T. Tran, J. Zhang, W. Wu, H. Song et al., Synthesis of titanosilicate pillared MFI zeolite as an efficient photocatalyst. RSC Adv. **7**(6), 3249–3256 (2017). https://doi.org/10.1039/c6ra23959e
152. H. He, W. Zhai, P. Liu, J. Wang, Rational design of metal–organic framework based photocatalysts correlated with specific additives for driving gas–liquid-solid CO_2 reduction. Mater. Today **83**, 382–403 (2025). https://doi.org/10.1016/j.mattod.2024.12.019
153. Z. Zhang, M. Li, R. Gao, S. Yang, Q. Ma et al., Selective and scalable CO_2 electrolysis enabled by conductive zinc ion-implanted zeolite-supported cadmium oxide nanoclusters. J.

Am. Chem. Soc. **146**(9), 6397–6407 (2024). https://doi.org/10.1021/jacs.4c01061

154. X. Chi, M. Li, X. Chen, J. Xu, X. Yin et al., Enabling high-performance all-solid-state batteries *via* guest wrench in zeolite strategy. J. Am. Chem. Soc. **145**(44), 24116–24125 (2023). https://doi.org/10.1021/jacs.3c07858
155. J.U. Kim, S. Lee, S.J. Kang, T.I. Kim, Materials and design of nanostructured broadband light absorbers for advanced light-to-heat conversion. Nanoscale **10**(46), 21555–21574 (2018). https://doi.org/10.1039/c8nr06024j
156. Z. Sun, C. Dang, H. Zhang, Y. Feng, M. Jiang et al., Lignin powered versatile bioelastomer: a universal medium for smart photothermal conversion. Adv. Funct. Mater. **34**(45), 2405130 (2024). https://doi.org/10.1002/adfm.202405130
157. F. Wang, J. He, J. Hu, Z. Chen, Y. Shi et al., Photothermal properties of Cu@polycarbonate composites with strong localized surface plasmon resonances. Nano Res. **17**(9), 8513–8520 (2024). https://doi.org/10.1007/s12274-024-6805-0
158. Z. Chen, X. Dong, Z.-X. Sun, X. An, C. Li et al., Hierarchical carbon nanocages as superior supports for photothermal CO_2 catalysis. ACS Nano **18**(30), 19672–19681 (2024). https://doi.org/10.1021/acsnano.4c04691
159. B. Wang, H. Chen, W. Zhang, H. Liu, Z. Zheng et al., Semimetallic bismuthene with edge-rich dangling bonds: broad-spectrum-driven and edge-confined electron enhancement boosting CO_2 hydrogenation reduction. Adv. Mater. **36**(19), e2312676 (2024). https://doi.org/10.1002/adma.202312676
160. Y. Chen, T. Li, H. Guo, X. Wang, W. Cui, Revealing the mechanism of converting CO_2 into methanol by the Cu_2O and oxygen vacancy on MgO: experiments and density functional theory. ACS Appl. Mater. Interfaces **16**(36), 47662–47673 (2024). https://doi.org/10.1021/acsami.4c09920
161. H.-J. Lv, Q. Ul Hassan, S.-C. Fan, Y. Wang, Y. An et al., Ultrafine Pd nanoparticles anchored on hierarchically porous titanium-based MOFs for superior photothermal CO_2 reduction. Sci. China Mater. **66**(6), 2317–2328 (2023). https://doi.org/10.1007/s40843-022-2388-0
162. H. Li, Y. Tang, W. Yan, M. Liu, Z. Wang et al., Vacancy-enhanced photothermal activation for CO_2 methanation on Ni/$SrTiO_3$ catalysts. Appl. Catal. B Environ. Energy **357**, 124346 (2024). https://doi.org/10.1016/j.apcatb.2024.124346
163. J. Lee, D.C. Sorescu, X. Deng, Electron-induced dissociation of CO_2 on TiO_2(110). J. Am. Chem. Soc. **133**(26), 10066–10069 (2011). https://doi.org/10.1021/ja204077e
164. Y. Wu, Q. Hu, Q. Chen, X. Jiao, Y. Xie, Fundamentals and challenges of engineering charge polarized active sites for CO_2 photoreduction toward C_2 products. Acc. Chem. Res. **56**(18), 2500–2513 (2023). https://doi.org/10.1021/acs.accounts.3c00373
165. H. Ma, X. Wang, T. Tan, X. Zhou, F. Dong et al., Stabilize the oxygen vacancies in Bi_2SiO_5 for durable photocatalysis *via* altering local electronic structure with phosphate dopant. Appl. Catal. B Environ. **319**, 121911 (2022). https://doi.org/10.1016/j.apcatb.2022.121911
166. K.K. Ghuman, L.B. Hoch, T.E. Wood, C. Mims, C.V. Singh et al., Surface analogues of molecular frustrated lewis pairs in heterogeneous CO_2 hydrogenation catalysis. ACS Catal. **6**(9), 5764–5770 (2016). https://doi.org/10.1021/acscatal.6b01015
167. K.K. Ghuman, L.B. Hoch, P. Szymanski, J.Y. Loh, N.P. Kherani et al., Photoexcited surface frustrated lewis pairs for heterogeneous photocatalytic CO_2 reduction. J. Am. Chem. Soc. **138**(4), 1206–1214 (2016). https://doi.org/10.1021/jacs.5b10179
168. W. Miao, Y. Li, R. Hao, W. Xu, Z. Wang et al., Dynamic surface reconstruction of plasmonic TiN creates frustrated lewis pairs for boosting photothermal CO_2 hydrogenation performance. Nano Energy **146**, 111548 (2025). https://doi.org/10.1016/j.nanoen.2025.111548
169. M. Wang, G. Gan, Y. He, Y. Li, G. Zhang, Ru-modified Co_3O_4 ultrathin nanosheets with enriched frustrated Lewis pairs for efficient photothermal CO_2 methanation. Chem. Eng. J. **538**, 176634 (2026). https://doi.org/10.1016/j.cej.2026.176634
170. D. Mateo, N. Morlanes, P. Maity, G. Shterk, O.F. Mohammed et al., Efficient visible-light driven photothermal conversion of CO_2 to methane by nickel nanoparticles supported on barium titanate. Adv. Funct. Mater. **31**(8), 2008244 (2021). https://doi.org/10.1002/adfm.202008244
171. I.S. Khan, D. Mateo, G. Shterk, T. Shoinkhorova, D. Poloneeva et al., An efficient metal–organic framework-derived nickel catalyst for the light driven methanation of CO_2. Angew. Chem. Int. Ed. **60**(51), 26476–26482 (2021). https://doi.org/10.1002/anie.202111854
172. B. Gao, Z. Wen, Y. Wang, D. Chen, B. Yang et al., Recent advances in alloy catalysts for CO_2 hydrogenation to methanol. ChemCatChem **16**(19), e202400814 (2024). https://doi.org/10.1002/cctc.202400814
173. S.C. Lin, C.C. Chang, S.Y. Chiu, H.T. Pai, T.Y. Liao et al., Operando time-resolved X-ray absorption spectroscopy reveals the chemical nature enabling highly selective CO2 reduction. Nat. Commun. **11**(1), 3525 (2020). https://doi.org/10.1038/s41467-020-17231-3
174. W.-H. Li, J. Yang, D. Wang, Long-range interactions in diatomic catalysts boosting electrocatalysis. Angew. Chem. Int. Ed. **61**(52), e202213318 (2022). https://doi.org/10.1002/anie.202213318
175. H. Ou, G. Li, W. Ren, B. Pan, G. Luo et al., Atomically dispersed Au-assisted C-C coupling on red phosphorus for CO_2 photoreduction to C_2H_6. J. Am. Chem. Soc. **144**(48), 22075–22082 (2022). https://doi.org/10.1021/jacs.2c09424
176. S. Zhu, X. Li, X. Jiao, W. Shao, L. Li et al., Selective CO_2 photoreduction into C_2 product enabled by charge-polarized metal pair sites. Nano Lett. **21**(5), 2324–2331 (2021). https://doi.org/10.1021/acs.nanolett.1c00383
177. K. Yan, D. Wu, T. Wang, C. Chen, S. Liu et al., Highly selective ethylene production from solar-driven CO_2 reduction on the Bi_2S_3@In_2S_3 catalyst with In–S_V–Bi active sites. ACS Catal. **13**(4), 2302–2312 (2023). https://doi.org/10.1021/acscatal.2c05741

© The authors https://doi.org/10.1007/s40820-026-02351-0

178. Q. Hao, Z. Li, Y. Zhu, Y. Shi, M. Huo et al., BCN-supported CoFe alloy catalysts for enhanced C─C coupling in photothermocatalytic CO hydrogenation. Adv. Funct. Mater. **34**(40), 2403848 (2024). https://doi.org/10.1002/adfm.202403848
179. R.-P. Ye, J. Ding, W. Gong, M.D. Argyle, Q. Zhong et al., CO_2 hydrogenation to high-value products *via* heterogeneous catalysis. Nat. Commun. **10**(1), 5698 (2019). https://doi.org/10.1038/s41467-019-13638-9
180. A. Ramirez, X. Gong, M. Caglayan, S.F. Nastase, E. Abou-Hamad et al., Selectivity descriptors for the direct hydrogenation of CO_2 to hydrocarbons during zeolite-mediated bifunctional catalysis. Nat. Commun. **12**(1), 5914 (2021). https://doi.org/10.1038/s41467-021-26090-5
181. G. Song, M. Li, P. Yan, M.A. Nawaz, D. Liu, High conversion to aromatics *via* CO_2-FT over a CO-reduced Cu-Fe_2O_3 catalyst integrated with HZSM-5. ACS Catal. **10**(19), 11268–11279 (2020). https://doi.org/10.1021/acscatal.0c02722
182. J. Wei, R. Yao, Y. Han, Q. Ge, J. Sun, Towards the development of the emerging process of CO_2 heterogenous hydrogenation into high-value unsaturated heavy hydrocarbons. Chem. Soc. Rev. **50**(19), 10764–10805 (2021). https://doi.org/10.1039/d1cs00260k
183. S. Tada, D. Li, M. Okazaki, H. Kinoshita, M. Nishijima et al., Influence of Si/Al ratio of MOR type zeolites for bifunctional catalysts specific to the one-pass synthesis of lower olefins *via* CO_2 hydrogenation. Catal. Today **411**, 113828 (2023). https://doi.org/10.1016/j.cattod.2022.06.043
184. J. Wei, R. Yao, Q. Ge, D. Xu, C. Fang et al., Precisely regulating Brønsted acid sites to promote the synthesis of light aromatics *via* CO_2 hydrogenation. Appl. Catal. B Environ. **283**, 119648 (2021). https://doi.org/10.1016/j.apcatb.2020.119648
185. P. Gao, S. Li, X. Bu, S. Dang, Z. Liu et al., Direct conversion of CO_2 into liquid fuels with high selectivity over a bifunctional catalyst. Nat. Chem. **9**(10), 1019–1024 (2017). https://doi.org/10.1038/nchem.2794
186. E.A. Elimian, M. Zhang, J. Chen, H. Jia, Y. Sun et al., Construction of Pt-mTiO_2/USY multifunctional catalyst enriched with oxygen vacancies for the enhanced light-driven photothermocatalytic degradation of toluene. Appl. Catal. B Environ. Energy **307**, 121203 (2022). https://doi.org/10.1016/j.apcatb.2022.121203
187. S. Bai, W. Jing, G. He, C. Liao, F. Wang et al., Near-infrared-responsive photocatalytic CO_2 conversion *via In situ* generated Co_3O_4/Cu_2O. ACS Nano **17**(11), 10976–10986 (2023). https://doi.org/10.1021/acsnano.3c03118
188. S. Mo, S. Li, J. Zhou, X. Zhao, H. Zhao et al., Asymmetric interaction between carbon and Ni-cluster in Ni–C–In photothermal catalysts for point-concentrated solar-driven CO_2 reverse water–gas shift reaction. ACS Catal. **15**(4), 2796–2808 (2025). https://doi.org/10.1021/acscatal.4c05916
189. Q. Wei, Y. Yang, J. Hou, H. Liu, F. Cao et al., Direct solar photocatalytic hydrogen generation with CPC photoreactors: system development. Sol. Energy **153**, 215–223 (2017). https://doi.org/10.1016/j.solener.2017.05.064
190. S. Kar, D. Kim, A. Bin Mohamad Annuar, B.B. Sarma, M. Stanton et al., Direct air capture of CO_2 for solar fuel production in flow. Nat. Energy **10**(4), 448–459 (2025). https://doi.org/10.1038/s41560-025-01714-y
191. P. Kant, S. Liang, M. Rubin, G.A. Ozin, R. Dittmeyer, Low-cost photoreactors for highly photon/energy-efficient solar-driven synthesis. Joule **7**(6), 1347–1362 (2023). https://doi.org/10.1016/j.joule.2023.05.006
192. W.T. Xie, Y.J. Dai, R.Z. Wang, K. Sumathy, Concentrated solar energy applications using Fresnel lenses: a review. Renew. Sustain. Energy Rev. **15**(6), 2588–2606 (2011). https://doi.org/10.1016/j.rser.2011.03.031
193. Z. Wu, J. Shen, C. Li, C. Zhang, K. Feng et al., Mo_2TiC_2 MXene-supported Ru clusters for efficient photothermal reverse water–gas shift. ACS Nano **17**(2), 1550–1559 (2023). https://doi.org/10.1021/acsnano.2c10707
194. X. Liu, C. Xing, F. Yang, Z. Liu, Y. Wang et al., Strong interaction over Ru/defects-rich aluminium oxide boosts photothermal CO_2 methanation *via* microchannel flow-type system. Adv. Energy Mater. **12**(31), 2201009 (2022). https://doi.org/10.1002/aenm.202201009
195. T. Dong, X. Liu, Z. Tang, H. Yuan, D. Jiang et al., Ru decorated TiO_x nanoparticles *via* laser bombardment for photothermal co-catalytic CO_2 hydrogenation to methane with high selectivity. Appl. Catal. B Environ. **326**, 122176 (2023). https://doi.org/10.1016/j.apcatb.2022.122176
196. Y. Li, X. Bai, D. Yuan, F. Zhang, B. Li et al., General heterostructure strategy of photothermal materials for scalable solar-heating hydrogen production without the consumption of artificial energy. Nat. Commun. **13**(1), 776 (2022). https://doi.org/10.1038/s41467-022-28364-y
197. Y. Li, F. Meng, Q. Wu, D. Yuan, H. Wang et al., A Ni-O-Ag photothermal catalyst enables 103–m2 artificial photosynthesis with solar-to-chemical energy conversion efficiency. Sci. Adv. **10**(20), 5098 (2024). https://doi.org/10.1126/sciadv.adn5098
198. K. Du, J. Guo, C. Song, X. Liu, M. Chen et al., Persistent photothermal CO_2 methanation without external energy input. Energy Environ. Sci. **18**(3), 1255–1261 (2025). https://doi.org/10.1039/d4ee04849k
199. H. Nishiyama, T. Yamada, M. Nakabayashi, Y. Maehara, M. Yamaguchi et al., Photocatalytic solar hydrogen production from water on a 100–m^2 scale. Nature **598**(7880), 304–307 (2021). https://doi.org/10.1038/s41586-021-03907-3
200. T. Yamada, H. Nishiyama, H. Akatsuka, S. Nishimae, Y. Ishii et al., Production of methane by sunlight-driven photocatalytic water splitting and carbon dioxide methanation as a means of artificial photosynthesis. ACS Eng. Au **3**(5), 352–363 (2023). https://doi.org/10.1021/acsengineeringau.3c00034

201. M. Monai, K. Jenkinson, A.E.M. Melcherts, J.N. Louwen, E.A. Irmak et al., Restructuring of titanium oxide overlayers over nickel nanoparticles during catalysis. Science **380**(6645), 644–651 (2023). https://doi.org/10.1126/science.adf6984
202. S. Huygh, A. Bogaerts, E.C. Neyts, How oxygen vacancies activate CO_2 dissociation on TiO_2 anatase (001). J. Phys. Chem. C **120**(38), 21659–21669 (2016). https://doi.org/10.1021/acs.jpcc.6b07459
203. L. Xie, J. Liang, L. Jiang, W. Huang, Effects of oxygen vacancies on hydrogenation efficiency by spillover in catalysts. Chem. Sci. **16**(8), 3408–3429 (2025). https://doi.org/10.1039/d4sc07375d
204. J. Zhou, J. Zhao, J. Zhang, T. Zhang, M. Ye et al., Regeneration of catalysts deactivated by coke deposition: a review. Chin. J. Catal. **41**(7), 1048–1061 (2020). https://doi.org/10.1016/S1872-2067(20)63552-5
205. X. Ding, W. Liu, J. Zhao, L. Wang, Z. Zou, Photothermal CO_2 catalysis toward the synthesis of solar fuel: from material and reactor engineering to techno-economic analysis. Adv. Mater. (Deerfield Beach Fla) **37**(2), e2312093 (2025). https://doi.org/10.1002/adma.202312093
206. S. Sollai, A. Porcu, V. Tola, F. Ferrara, A. Pettinau, Renewable methanol production from green hydrogen and captured CO_2: a techno-economic assessment. J. CO2 Util. **68**, 102345 (2023). https://doi.org/10.1016/j.jcou.2022.102345
207. G.A. Cuevas-Castillo, S. Michailos, M. Akram, K. Hughes, D. Ingham et al., Techno economic and life cycle assessment of olefin production through CO_2 hydrogenation within the power-to-X concept. J. Clean. Prod. **469**, 143143 (2024). https://doi.org/10.1016/j.jclepro.2024.143143
208. S. Mo, X. Zhao, J. Li, Y. Fan, P. Wu et al., Orbital hybridization-mediated selective photothermal CO_2 hydrogenation over single-atom $Ru1/CeO_2$ catalysts. Appl. Catal. B Environ. Energy **382**, 125949 (2026). https://doi.org/10.1016/j.apcatb.2025.125949

Publisher's Note Springer Nature remains neutral with regard to jurisdictional claims in published maps and institutional affiliations.

© The authors https://doi.org/10.1007/s40820-026-02351-0